Gernot J. Kraberger, BSc

Controlling the electronic structure of graphene by collective electrostatic effects

MASTER THESIS

For obtaining the academic degree
Diplom-Ingenieur

Master Programme of
Technical Physics

Graz University of Technology

Supervisor:

Ao.Univ.-Prof. Dipl.-Ing. Dr.techn. Egbert Zojer

Institute of Solid State Physics

Graz, October 2014

EIDESSTATTLICHE ERKLÄRUNG

AFFIDAVIT

Ich erkläre an Eides statt, dass ich die vorliegende Arbeit selbstständig verfasst, andere als die angegebenen Quellen/Hilfsmittel nicht benutzt, und die den benutzten Quellen wörtlich und inhaltlich entnommenen Stellen als solche kenntlich gemacht habe. Das in TUGRAZonline hochgeladene Textdokument ist mit der vorliegenden Masterarbeit identisch.

I declare that I have authored this thesis independently, that I have not used other than the declared sources/resources, and that I have explicitly indicated all material which has been quoted either literally or by content from the sources used. The text document uploaded to TUGRAZonline is identical to the present master's thesis.

Datum / Date

Unterschrift / Signature

Abstract

The recent isolation of graphene has triggered a steadily growing research interest due to its fascinating structural and electronic properties. For achieving the important goal of finding new applications, it is necessary to control and tune the electonic structure of graphene. In order to reach this aim, several strategies building upon structural and chemical modifications have already been assessed.

In this thesis, the novel idea of using collective electrostatic effects to controllably modify graphene is investigated by means of standard density functional theory. As an initial step, selected neighboring carbon atoms of graphene are substituted with pairs of boron and nitrogen atoms, so that they form lines of dipoles embedded into the two-dimensional layer. The consequences of the dipolar fields acting on the material in its vicinity are examined: modifications of the electrostatic potential, energy shifts of the states and of the density of states and changes in the band structure are observed. Furthermore, the possibility of largely localizing the frontier states in the graphene region between two oppositely oriented dipole lines close to each other is discussed. It is shown that the width of these strips between the dipole lines plays a major role for the size of the energy shift. Also the geometries of the boron-nitrogen-lines (e. g. in parallel orientation, or in zigzag- or armchair-fashion) turn out to be relevant.

As a probably more realistic system, the ordered adsorption of organic molecules with dipolar end groups on the otherwise unmodified graphene sheet is subsequently investigated. Here, qualitatively the same effects can be found. They are, however, less pronounced – a fact that is thoroughly explored and explained. Semiconducting and isolating two-dimensional materials are expected to behave slightly differently than semimetals like graphene, thus the adsorption of the same molecules on single layers of hexagonal boron nitride is finally examined and compared to the other systems.

Kurzfassung

Die Isolierung von Graphen hat ein stetig wachsendes Interesse an diesem Material ausgelöst, was wohl an seinen faszinierenden strukturellen und elektronischen Eigenschaften liegt. Das wichtigste Ziel dieser Forschung ist es, daraus neue Anwendungen zu entwickeln. Bevor das aber möglich ist, muss man erst die elektronische Struktur von Graphen kontrollieren können. Dazu gab es bereits verschiedene Vorschläge, wobei meist chemische oder strukturelle Veränderungen des Materials untersucht wurden.

In dieser Arbeit wird eine neue Idee verfolgt: die Verwendung kollektiver elektrostatischer Effekte, um Graphen gezielt zu modifizieren. Dies wird mittels Standard-Dichtefunktionaltheorieberechnungen untersucht. Zuerst werden Dipollinien direkt in die zweidimensionale Graphenschicht eingebaut, und zwar durch Substitution ausgewählter benachbarter Kohlenstoffatome in Graphen durch Paare von Bor- und Stickstoffatomen. Die so entstehenden Dipolfelder wirken sich auf das Graphen nahe der Dipollinien folgendermaßen aus: Das elektrostatische Potential ändert sich, was die Energie der einzelnen Zustände verschiebt und somit auch die Zustandsdichte sowie die Bandstruktur beeinflusst. Es ist außerdem möglich, die Zustände nahe der Fermienergie mehr oder weniger gut in Bereichen zwischen zwei entgegengesetzt ausgerichteten Dipollinien zu lokalisieren. Eine große Rolle für die Stärke des Effekts spielt vor allem die Breite der Graphenstreifen zwischen den Dipollinien. Außerdem wird noch untersucht, wie groß der Einfluss der Anordnung der Bor-Stickstoff-Linien (also mit parallelen Dipolen oder in Zigzag- oder Armchairgeometrie) ist.

Es ist vermutlich deutlich realistischer, dipolare Linien durch die geordnete Adsorption organischer Moleküle mit polaren Endgruppen auf reinem Graphen zu erzeugen. Das liefert qualitativ die gleichen Effekte. Man stellt jedoch fest, dass deren Stärke deutlich geringer ist, was im Rahmen dieser Arbeit ausführlich dokumentiert und erklärt wird. Man erwartet, dass sich das Verhalten halbleitender und isolierender zweidimensionaler Materialien von Semimetallen wie Graphen unterscheidet. Deshalb wird zum Schluss noch betrachtet, wie sich die Adsorption derselben organischen Moleküle auf zweidimensionalem hexagonalem Bornitrid auswirkt und die Ergebnisse werden mit Graphen verglichen.

Acknowledgements

First of all, I want to thank my supervisor *Egbert Zojer* for giving me the opportunity to work in his group, for teaching me how to do science and for being a constant source of new ideas.

David Egger taught me how to use VASP and GADGET, was always ready to have interesting discussions and motivated me whenever it was necessary.

The members of the "Egberten" group have always been there for advice, discussions and moral support concerning science and everything else – in the office, during lunch and coffee breaks. Thank you, *Lisi Wruß*, *Elsi Verwüster* (especially for helping me when I reached the limits of my chemical knowledge), *Veronika Obersteiner*, *Iris Hehn*, *Bernhard Kretz*, *Thomas Taucher*, *Shashank Harivyasi* and in the last few months *Anu Baby*, *Hermann Edlbauer* and *Georg Huhs*. All the time, *Oliver Hofmann* was a source of good advice. *Karin Zojer* always thought of me when she found interesting papers. I also want to thank the members of her group, *Antón Fernández-Fernández*, *Philipp Breitegger* and *Markus Krammer* and the students who did their Bachelor thesis in our group last summer (*Christian Winkler* – who I had the joy of mentoring, *Andreas Jeindl* and *Stefan Cesnik*) for socializing.

This thesis also marks the end of my Master studies in Technical Physics, which would not have been possible without the scientific discussions, mutual support and the occasional beer with my study mates. In particular, I want to thank *Paul Christian* (my valued lab course partner for many years), *Manuel Zingl*, *Patrick Falk*, *Christian Röthel*, *Georg Urstöger*, *Christian Neubauer*, *Benjamin Lang*, *Martin Kupper* and *Martin Buschmann*.

I am grateful to *Winfried Kernbichler* and *Lilia Boeri* for giving me the opportunity to work as their teaching assistant during my studies. I have learned a lot working as a tutor!

My parents, my brother and my family have always supported me, for which I cannot thank them enough. I want to particularly thank my aunt *Edith Hainzl* for providing me with the flat I have lived in throughout my whole studies.

The *Austrian Science Fund* (FWF) gave me financial support in the form of a Forschungsstipendium (Project I 937-N19). I was able to attend the Spring School 2014 of the *Forschungszentrum Jülich* free of charge due to their financial support for Master students. The *Erasmus* program allowed me to spend a wonderful semester at the Université Joseph Fourier in Grenoble during my Master studies. Finally, I want to thank the ZID TU Graz for providing the computational resources (mainly the *dcluster*, but also the icluster) for the calculations performed for this thesis.

Contents

List of Abbreviations

AC	armchair
BZ	first Brillouin zone
DFT	density functional theory
DOS	density of states
e	Elementary charge, $e = 1.60 \cdot 10^{-19}\,\mathrm{As}$
E_{pot}	Electron potential energy
ε_0	Vacuum permittivity, $\varepsilon_0 = 8.85 \cdot 10^{-12}\,\mathrm{A^2 s^4 kg^{-1} m^{-3}}$
FFT	Fast Fourier Transform
GGA	generalized gradient approximation
GNR	graphene nanoribbon
$\hbar$	Planck constant, $\hbar = 6.63 \cdot 10^{-34}\,\mathrm{J \cdot s} = 4.14 \cdot 10^{-15}\,\mathrm{eV \cdot s}$
hBN	hexagonal boron nitride
KS	Kohn-Sham
LDA	local density approximation
LDOS	Local Density of States
LUMO	lowest unoccupied molecular orbital
m_e	Electron mass, $m_e = 9.11 \cdot 10^{-31}\,\mathrm{kg}$
$\mathbf{p}$	Dipole moment
PAW	projector augmented wave
PBE	Perdew-Burke-Ernzerhof
PDOS	Projected Density of States
SCF	self-consistent field
TW	Tour wire
TW-CN	Dicyano-substituted diphenylacetylene

TW-NC	Di-isocyano-substituted diphenylacetylene
TW-NO_2	Dinitro-substituted diphenylacetylene
TW-Pyr N_{in}	Pyrimidine substituted Tour-wire based molecule in ortho position
TW-Pyr N_{out} CN	(Ortho)-dicyano substituted dipyrimidine acetylene
TW-Pyr N_{out}	Pyrimidine substituted Tour-wire based molecule in meta position
TW alone	Diphenylacetylene
VASP	Vienna Ab initio Simulation Package
vdW-TS	van der Waals Tkatchenko-Scheffler
XPS	X-ray photoelectron spectroscopy
ZZ	zigzag

1. Introduction and Motivation

Graphene and graphene-based materials is arguably the topic that has attracted the biggest research interest in recent years. Exploring the unique properties, selectively modifying them, and finding novel applications in the form of revolutionary devices is the motivation that fuels all this work. A vast number of different ways to tune graphene and its relatives have been suggested and investigated [1], including lateral confinement, doping, the use of different substrates and the application of external fields. In contrast, the use of collective electrostatic effects from dipolar chemical groups presented in this thesis is a different and highly exciting approach.

The heart of *collective electrostatic effects* is that there is a qualitative change in behavior when going from a single dipole to higher-dimensional arrangements of dipoles (this will be thoroughly explained in chapter 2.2). Especially a two-dimensional arrangement of dipoles plays a huge role in surface science, as work function differences of different surfaces of crystals can be explained by surface dipoles. [2] Furthermore, a specific modification of surface-related properties is viable by means of the ordered adsorption of monolayers of polar molecules. [3–5] The prospects of lines of dipoles to locally change the characteristics of the surrounding matter have not been assessed so far.

Using these *linear arrangements* of polar constituents, it is possible to permanently create potential differences between distinct parts of the graphene sheet, which leads to local changes of the energy of the electronic states of the material. This can be useful both in the context of seletively modifying the conduction properties with the long-term goal of graphene-based integrated circuits and for device creation purposes [6][1]. Still the aim of this thesis lies in the investigation and documentation of the impact of one-dimensional collective electrostatic effects on a two-dimensional material from the point of view of fundamental research rather than application-driven innovation.

Quantum mechanical computer simulations using *density functional theory* are the perfect tool to quickly and cost-effectively examine newly proposed systems like these. Apart from the possibility to look at large numbers of different systems without having to invest too much time and effort, one can also state general points using proof of principle models in idealized situations. Furthermore, many different quantities are easily accessible at the end of a numerical calculation without the need to perform diverse measuring procedures

[1] Although the system presented in Ref. [6] looks similar to some of the systems discussed throughout this thesis, collective electrostatic effects do not play a role there. The device presented in this paper mainly relies on different doping concentrations and uses hexagonal boron nitride for its isolating properties to confine graphene states.

one after the other.

This thesis starts out with a very brief overview of the key points of density functional theory, more in the style of a reminder than a thourough introduction (chapter 2.1). Then, the electrostatic properties of dipoles are reviewed and the curious effects that appear when they are arranged in certain orders are discussed (chapter 2.2). When a sea of electrons is perturbed by extra local charges, the effects resulting from these charges will in general be screened by the electrons. As these effects play a role in graphene modified by dipoles, it should be incorporated in the electrostatic modelling of the situation. A very simple theory that takes into account these processes is Thomas-Fermi theory, which will be shortly presented in chapter 2.3. The astonishing structural electronical and structural properties of graphene are then summarized in chapter 2.4.

The methodology used to perform the ab-initio calculations is presented in chapter 3, along with the methods employed for the analysis of the achieved results.

As a first system, graphene with dipoles embedded directly into the plane is investigated (chapter 4). This is done using pairs of boron and nitrogen atoms placed where usually two neighboring carbon atoms would sit, so that the dipoles formed by these heteroatoms are arranged in a line. The resulting effects on the potential and electronic states of the material are then discussed in detail. Another, probably more realistic, approach is the adsorption of self-assembled monolayers of molecules with polar end groups. A toy model for these systems is investigated in chapter 5.

To see how well this approach works also for other two-dimensional materials and to see the different kind of behavior of a semimetal and an isolator, the adsorption of polar molecules on two-dimensional hexagonal boron nitride is finally studied (chapter 6).

2. Theoretical Foundations

2.1. Density Functional Theory

In solid state theory, calculating the electronic properties of a system is equivalent to solving the *Schrödinger equation* [7]

$$H|\psi\rangle = E|\psi\rangle, \tag{2.1}$$

where $|\psi\rangle$ is the many-electron wavefunction of the eigenstate of the system and E is the eigenenergy. H is the electronic part of the Hamiltonian [7], obtained by applying the *Born-Oppenheimer approximation*, (expressed in SI units)

$$H = -\frac{\hbar^2}{2m_e}\sum_i \nabla_i^2 - \frac{1}{4\pi\varepsilon_0}\sum_i\sum_A \frac{Z_A e^2}{|\mathbf{r}_i - \mathbf{R}_A|} + \frac{1}{2}\frac{e^2}{4\pi\varepsilon_0}\sum_i\sum_{j\neq i}\frac{1}{|\mathbf{r}_i - \mathbf{r}_j|}, \tag{2.2}$$

where the sum over A runs over all the ions and sums over i or j run over all the electrons. The quantity Z_A is the atomic number and $\mathbf{R}_A$ the position of the ion with index A, $\mathbf{r}_i$ is the position of the electron with index i. The physical meaning of the three terms in this Hamiltonian is the kinetic energy of the electrons, the interaction of the electrons with the nuclei and the electron-electron interaction. [7] Especially the latter significantly complicates the treatment of this equation.

Two fundamentally different approaches for solving this many-body problem exist: wavefunction based methods (e. g. Hartree-Fock, configuration interaction, coupled cluster theory) and *density functional methods*. [8] In the latter, the key quantity is not the wavefunction, but the electron density $n(\mathbf{r})$. The *Hohenberg-Kohn theorem* [9] shows that the two descriptions are equivalent. Furthermore, the ground state electron density can be found by minimizing the energy functional $E[n]$ with respect to $n(\mathbf{r})$.

In practise, the interacting problem is mapped onto a non-interacting problem with the same electron density. This leads to the *Kohn-Sham equation*, which mathematically looks like the Schrödinger equation of non-interacting particles and can be solved. [10] The electron-electron interactions are accounted for in the local potential which is derived from the energy functional. The functional can be split up into different parts; however for the *exchange-correlation part* the exact functional is not known and one has to use approximations. In solid-state physics, the most commonly used approximatons are the local density approximation (LDA) and the generalized gradient approximation (GGA). [8] A commonly used GGA functional is the PBE functional proposed by John P. Perdew, Kieron

Burke and Matthias Ernzerhof in 1996. [11]

A detailed yet well accessible overview of DFT including practical aspects can be found in Richard Martin's book on electronic structure [7]. There is also a lot of further literature on that topic (e. g. [8, 12–15]). Thus, discussing DFT in more detail in this thesis would be futile.

2.2. Electrostatics

The fundamental relations presented in this chapter on electrostatics can be found in most textbooks on electrostatics or electrodynamics, for example in part three of Nolting's *Grundkurs Theoretische Physik* [16], on which the following considerations are based.

2.2.1. Dipole Potential

The electrostatic potential ϕ of a charged point-like particle is given by

$$\phi(\mathbf{r}) = \frac{1}{4\pi\varepsilon_0}\frac{q}{|\mathbf{r}-\mathbf{r}_0|}, \tag{2.3}$$

where q is the charge and $\mathbf{r}_0$ is the position of the particle.

Two oppositely charged particles form a *dipole*. The dipole potential is the sum of the potentials of the point charges, i. e. for a positively ($+q$) charged particle at $\mathbf{r}_+$ and a negatively ($-q$) charged particle at $\mathbf{r}_-$ it is

$$\phi_{\mathrm{dip}}(\mathbf{r}) = \frac{q}{4\pi\varepsilon_0}\left(\frac{1}{|\mathbf{r}-\mathbf{r}_+|} - \frac{1}{|\mathbf{r}-\mathbf{r}_-|}\right). \tag{2.4}$$

The key quantity for describing a dipole is its *dipole moment* $\mathbf{p} = q(\mathbf{r}_+ - \mathbf{r}_-)$, which for a continuous charge distribution $\rho(\mathbf{r})$ becomes

$$\mathbf{p}(\mathbf{r}) = \int d^3\mathbf{r}'\, \rho(\mathbf{r}')(\mathbf{r}'-\mathbf{r}). \tag{2.5}$$

Note that in chemistry, sometimes the opposite sign convention for dipole moments is used.

Using the multipole expansion, the dipole potential can be approximated as

$$\phi_{\mathrm{dip}}(\mathbf{r}) \approx \frac{1}{4\pi\varepsilon_0}\frac{\mathbf{p}\cdot(\mathbf{r}-\mathbf{r}_0)}{|\mathbf{r}-\mathbf{r}_0|^3}. \tag{2.6}$$

The dipole is now treated as point-like, sitting at $\mathbf{r_0} = \frac{1}{2}(\mathbf{r}_+ - \mathbf{r}_-)$. This approximation holds for large distances from the point dipole, i. e. when $|\mathbf{r}-\mathbf{r}_0| \gg |\mathbf{r}_+ - \mathbf{r}_-|$. Figure 2.1 shows

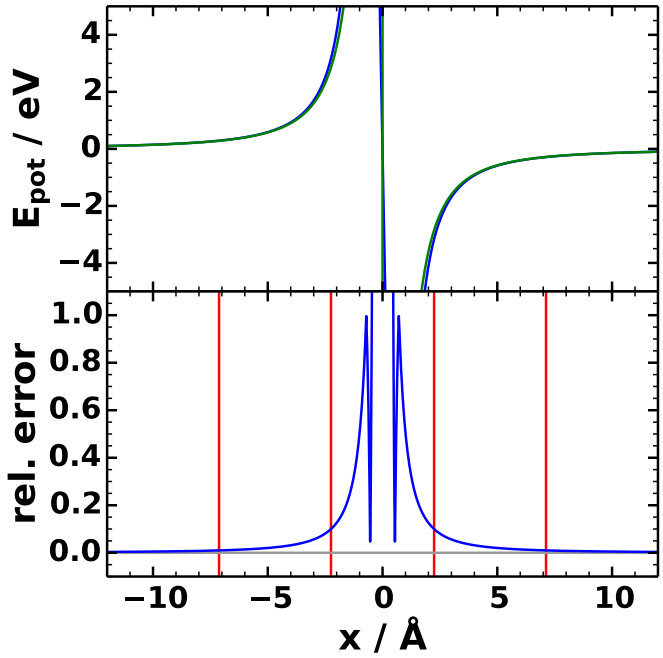

Figure 2.1.: Top: Electron potential energy E_{pot} for a dipole with a dipole moment of $p = 1\,\text{eÅ}$ in x-direction, where $|\mathbf{r}_+ - \mathbf{r}_-| = 1.42\,\text{Å}$. The calculation was once done using the exact equation (2.4) (blue line) and once using the point dipole approximation (2.6) (green line). Bottom: Relative error, i. e. the absolute error divided by the exact result. Especially in the region between the dipoles, the error is huge because the point dipole potential goes to infinity at $x = 0$ while the potential of the two separate point charges goes to zero. The vertical red lines mark the x-positions where the relative error drops below 10^{-1} and 10^{-2}.

how well it is doing in different distances from the dipole.

For a single dipole located at the origin and pointing in the x-direction, the potential along the x-axis goes like

$$\phi_{\text{dip}}(x) \approx \frac{1}{4\pi\varepsilon_0}\frac{p}{x^2}. \tag{2.7}$$

2.2.2. Lines of dipoles

First, the case where an infinite number of point dipoles is arranged in a line, with the dipole moments all pointing in the same direction perpendicular to the line (see figure 2.2), is considered. The distance between two neighboring dipoles is b. This is equivalent to imposing periodic boundary conditions in the direction along the line, with a “lattice constant” b.

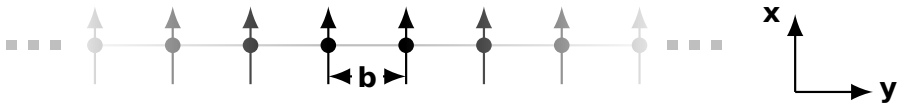

Figure 2.2.: Geometry of an infinitely extended dipole line. The arrows represent the individual dipole moments.

The potential due to this line of dipoles is a superposition of the potentials of the individual dipoles, located at $\mathbf{r}_i$:

$$\phi_{\text{line}}(\mathbf{r}) = \frac{1}{4\pi\varepsilon_0} \sum_i \frac{\mathbf{p}\cdot(\mathbf{r}-\mathbf{r}_i)}{|\mathbf{r}-\mathbf{r}_i|^3}. \tag{2.8}$$

For the dipoles pointing in the x-direction located on the y-axis, this leads to

$$\phi_{\text{line}}(x,y,z) = \frac{1}{4\pi\varepsilon_0} \sum_{i=-\infty}^{\infty} \frac{px}{(x^2+(y-ib)^2+z^2)^{3/2}}. \tag{2.9}$$

Due to the $\phi_{\text{dip}} \sim r^{-2}$ behavior of the dipole potential, the infinite sum only converges slowly with respect to the number of included dipoles. However, in this present one-dimensional case, the calculation is still feasible. A summation up to the limits of the machine precision can be done in reasonable time.

For large distances from the dipole line (i. e. much larger than its lattice constant b), the dipole line appears to be continuous with a dipole density $\mu = p/b$. Then, the infinite sum can be approximated by an integral

$$\phi_{\text{line}}(x,y,z) \approx \frac{1}{4\pi\varepsilon_0} \int_{-\infty}^{\infty} \frac{dy'\,\mu x}{(x^2+(y-y')^2+z^2)^{3/2}} = \frac{1}{4\pi\varepsilon_0}\frac{2\mu x}{x^2+z^2}. \tag{2.10}$$

To examine the resulting electrostatic potential along the x-axis, we set $z \to 0$ and obtain

$$\phi_{\text{line}}(x) \approx \frac{1}{4\pi\varepsilon_0}\frac{2\mu}{x}. \tag{2.11}$$

By comparing this result (2.11) to the result obtained for one single dipole (2.7), it can be seen that the potential of a dipole line drops far more slowly than the potential of a single dipole. This *collective electrostatic effect* not only changes the behavior quantitatively, but also qualitatively. The two different types of behavior can also be seen in figure 2.3.

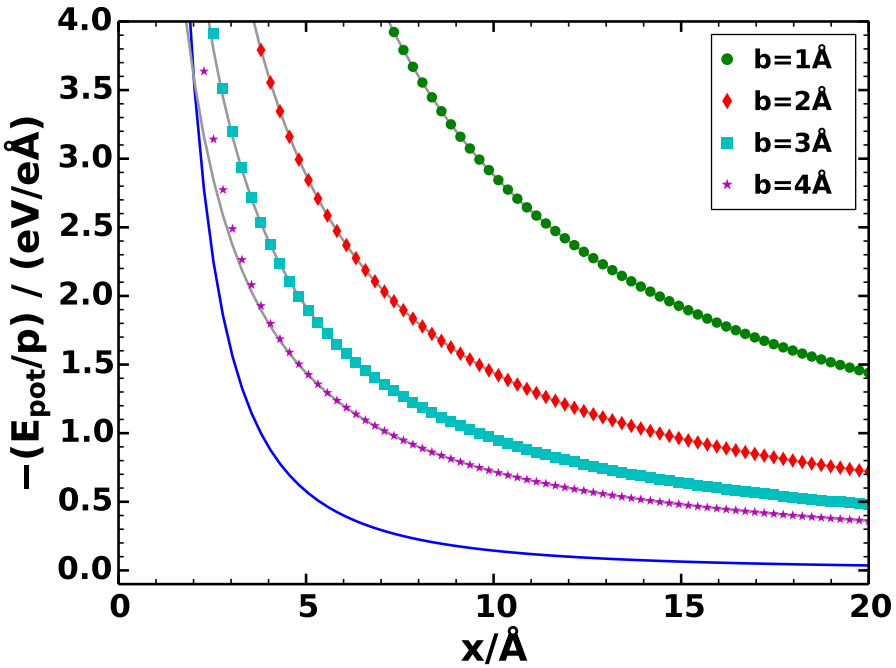

Figure 2.3.: Electron potential energy per unit dipole moment E_{pot}/p of a single point dipole that is pointing in the x-direction and is located at the origin (solid blue line). For different lattice constants b, the value of E_{pot}/p of the infinite sum of dipoles arranged along the y-axis is plotted (data points). The gray solid lines behind the data points are calculated according to (2.11) (with μ chosen to match the different values of b). This shows that for most of the plotted range, the treatment of the point dipoles as a continuous line according to (2.10) is already valid.

2.2.3. Arrays of Dipoles

The next system to look at is a two-dimensional *array of dipoles*, i. e. dipoles arranged on a rectangular grid. For dipoles with a dipole moment p pointing in the x-direction in a grid in the yz-plane (with lattice constants b and c along the y and z-direction), the electrostatic potential is

$$\phi_{\text{array}}(x,y,z) = \frac{1}{4\pi\varepsilon_0} \sum_{i=-\infty}^{\infty} \sum_{j=-\infty}^{\infty} \frac{px}{(x^2+(y-ib)^2+(z-jc)^2)^{3/2}}. \tag{2.12}$$

We can again examine this expression for long distances by taking the continuous limit with a dipole density $\mu = p/bc$

$$\phi_{\text{array}}(x,y,z) \approx \frac{1}{4\pi\varepsilon_0} \int_{-\infty}^{\infty} dz' \int_{-\infty}^{\infty} \frac{dy'\,\mu x}{(x^2+(y-y')^2+(z-z')^2)^{3/2}} = \frac{1}{4\pi\varepsilon_0} 2\pi\mu \operatorname{sgn} x. \tag{2.13}$$

That shows that for large x we get a constant potential (see figure 2.4). Furthermore, there is a different vacuum potential on the left and right side of the dipole array, with a potential difference

$$\Delta E_{\text{vac}} = 2\phi_\infty = \frac{1}{4\pi\varepsilon_0} \frac{4\pi p}{bc}. \tag{2.14}$$

The space is divided into two regions by the dipole plane. Again, a *collective electrostatic effect* changes the behavior qualitatively. This result plays a big role in surface science, because work function modifications due to surface dipoles (or bond dipoles due to adsorption) can be explained by the different vacuum potentials. [5]

For the infinite sums in (2.12), a direct summation is not feasible anymore. However, the form of the potential outside the dipole layer can be expressed as a Fourier series [3]

$$\phi_{\text{array}}(x,y,z) = \pm\phi_\infty + \frac{1}{4\pi\varepsilon_0} \sum_{m=-\infty}^{\infty} \sum_{n=-\infty}^{\infty} \frac{2\pi p}{bc} e^{i2\pi\left(\frac{my}{b}+\frac{nz}{c}\right)} e^{-2\pi\sqrt{\left(\frac{m}{b}\right)^2+\left(\frac{n}{c}\right)^2}|x|}. \tag{2.15}$$

This series converges much more quickly than the real space summation.

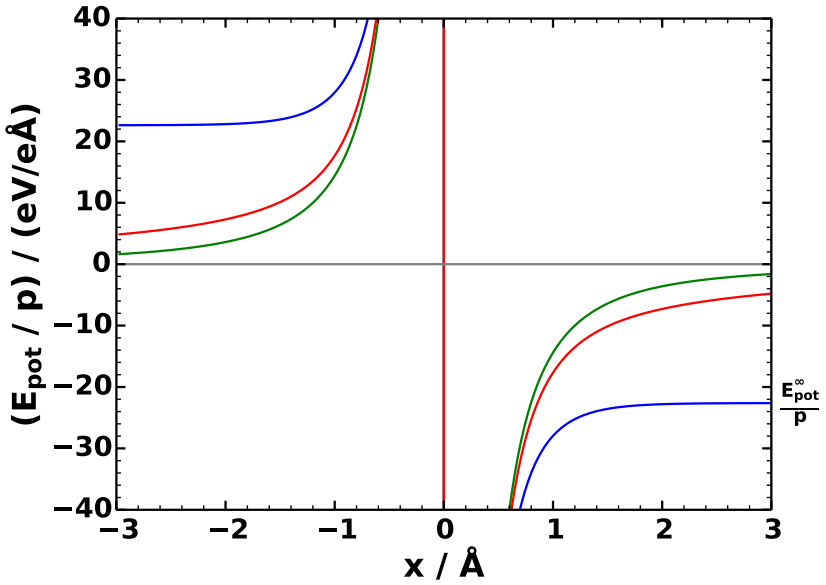

Figure 2.4.: Comparison of the electron potential energy per unit dipole moment E_{pot}/p of a single dipole at $x = 0$ (green line), a dipole line at $x = 0$ with a lattice constant $b = 2\,\text{Å}$ (red line) and a dipole array at $x = 0$ with lattice constants $b = c = 2\,\text{Å}$ (blue line). The constant value for large x, i. e. the shift of the vacuum potential, is marked as E^{∞}_{pot}.

2.2.4. Lattices of Dipoles

The next logical step is a three-dimensional *lattice of dipoles*[1]. Of course, this does not have a direct relevance to surface science and the systems treated in this thesis and is merely included for completeness.[2] Now, there are three lattice constants: a, b and c (in the directions x, y, z). The potential can be written as

$$\phi_{\text{lattice}}(\mathbf{r}') = \frac{1}{4\pi\varepsilon_0} \sum_j \sum_i \frac{\mathbf{p}_j(\mathbf{r}' - \mathbf{r}_j - \mathbf{R}_i)}{|\mathbf{r}' - \mathbf{r}_j - \mathbf{R}_i|^3}, \tag{2.16}$$

where the sum over i runs over all the unit cells (with lattice vectors $\mathbf{R}_i$) and the sum over j runs over the individual point dipoles in the unit cell (with positions $\mathbf{r}_j$ and dipole moments $\mathbf{p}_j$).

For one particular dipole in the unit cell (i. e. one special value for j), which we will choose

[1] In this case, the unit cell should not have a net dipole moment because otherwise the total energy would diverge. This problem only occurs due to the infinite extent of the crystal with periodic boundary conditions. For finite crystals, and thus for every real system, a unit cell with a net dipole moment leads to a macroscopic polarization of the sample (e. g. ferroelectricity).

[2] It also provides a way to assess the validity of the slab approach, which consists of performing 3D-periodic calculations for 2D-periodic systems by introducing a large vacuum gap (see chapter 3.1). In this thesis, this was checked using a more practical method, see figure 3.3.

as located in the origin and pointing in the x-direction, we get

$$\phi_{\text{lattice}}(x,y,z) = p \sum_i \frac{x - R_i^x}{((x-R_i^x)^2 + (y-R_i^y)^2 + (z-R_i^z)^2)^{3/2}}. \tag{2.17}$$

Now we rewrite $R_i^x = la$, $R_i^y = mb$ and $R_i^z = nc$ (where l, m and n are integers) and introduce relative coordinates $x = \xi a$, $y = \eta b$ and $z = \zeta c$ (where ξ, η and ζ are reals) to obtain

$$\phi_{\text{lattice}}(x,y,z) = p \sum_{l,m,n=-\infty}^{\infty} \frac{a(\xi - l)}{(a^2(\xi-l)^2 + b^2(\eta-m)^2 + c^2(\zeta-n)^2)^{3/2}}. \tag{2.18}$$

Now we pull all the factors of a out and substitute l, m, n by $-l$, $-m$ and $-n$ (which does not change anything because of the symmetric infinite sum) to get

$$\phi_{\text{lattice}}(x,y,z) = \frac{p}{a^2} \underbrace{\sum_{l,m,n=-\infty}^{\infty} \frac{\xi + l}{((\xi+l)^2 + \left(\frac{b}{a}\right)^2 (\eta+m)^2 + \left(\frac{c}{a}\right)^2 (\zeta+n)^2)^{3/2}}}_{=:X}. \tag{2.19}$$

The part of this summation that is named X is the same as the quantity X in equation (4) in Ref. [17], which is shown to be equal to (equation (6) in [17])

$$X = 8\pi \sum_{l=1}^{\infty} l \sin(2\pi l \xi) \sum_{m,n=-\infty}^{\infty} K_0(2\pi l \tilde{r}_{mn}(\eta,\zeta)), \tag{2.20}$$

with

$$\tilde{r}_{mn}(\eta,\zeta) = \left(\frac{b}{a}\right)^2 (\eta+m)^2 + \left(\frac{c}{a}\right)^2 (\zeta+n)^2. \tag{2.21}$$

K_0 is the modified Bessel function of second kind. This method of doing lattice sums is referred to as *Lekner summation*, which is rapidly converging. One problem with the application of that method is that K_0 diverges when its argument goes to zero, thus leading to problems if y and z both become zero. In principle, one can choose very small values for both variables; the limitation is the numerical stability of the calculation of the sum of the Bessel functions.

2.2.5. Polar Groups and Depolarization

In molecules and solids, certain arrangements of atoms can lead to *permanent dipole moments*. They can exist when the center of charge of the nuclei and the electrons do not coincide. For molecules or unit cells to have a global net dipole moment, there can be no mirror symmetry in the system. Of course, neither the charges involved nor the resulting dipoles are point like, but with increasing distance this approximation becomes better and better.

In contrast to fixed point charges, matter that forms dipoles is in general *polarizable*. That means that the dipole moment changes as a function of the local electric field acting at the location of the dipole. The local electric field can be of different origin, most importantly either by an external electric field or by the field of other dipoles in the vicinity. The latter effect plays a role for collective electrostatics, as each dipole feels the potential of all the other dipoles, which then leads to *depolarization*.

In the case of an infinitely extended dipole line, all the other dipoles create a field pointing in the direction opposite to that dipole. In figure 2.5, the electron potential energy due to the other dipoles is plotted together with the field. The negative end of the dipole would be on the left side, the positive end on the right side; the resulting dipole moment would thus point from left to right. Due to the presence of the other dipoles, the electron potential energy on the right, positive side is lowered which leads to an attraction of the electrons to the right side. This lowers the dipole strength.

Using the molecular polarizability α of the matter constituting the dipoles, the effective dipole moment can be written (up to first order) as [18, 19]

$$p = p_0 + \alpha E_{\parallel}, \tag{2.22}$$

where p_0 is the dipole moment in gas phase and $E_{\parallel}$ is the depolarizing local electric field parallel to the dipole orientation. The depolarization factor is given by p/p_0.

For a two-dimensional array of dipoles, the dipole jump is, as shown in (2.14)

$$\Delta E_{\text{vac}} = \frac{p}{\varepsilon_0 bc} = \frac{p_0}{\varepsilon \varepsilon_0 bc}, \tag{2.23}$$

where a relative permittivity ε was introduced. It describes the depolarization and is thus given by [18]

$$\varepsilon = \frac{p_0}{p}. \tag{2.24}$$

This effective dielectric constant is not equal to the bulk dielectric constant of the material.

Whenever the gas phase value of the dipole moment is not of relevance, working just with the effective dipole moment p is suitable.

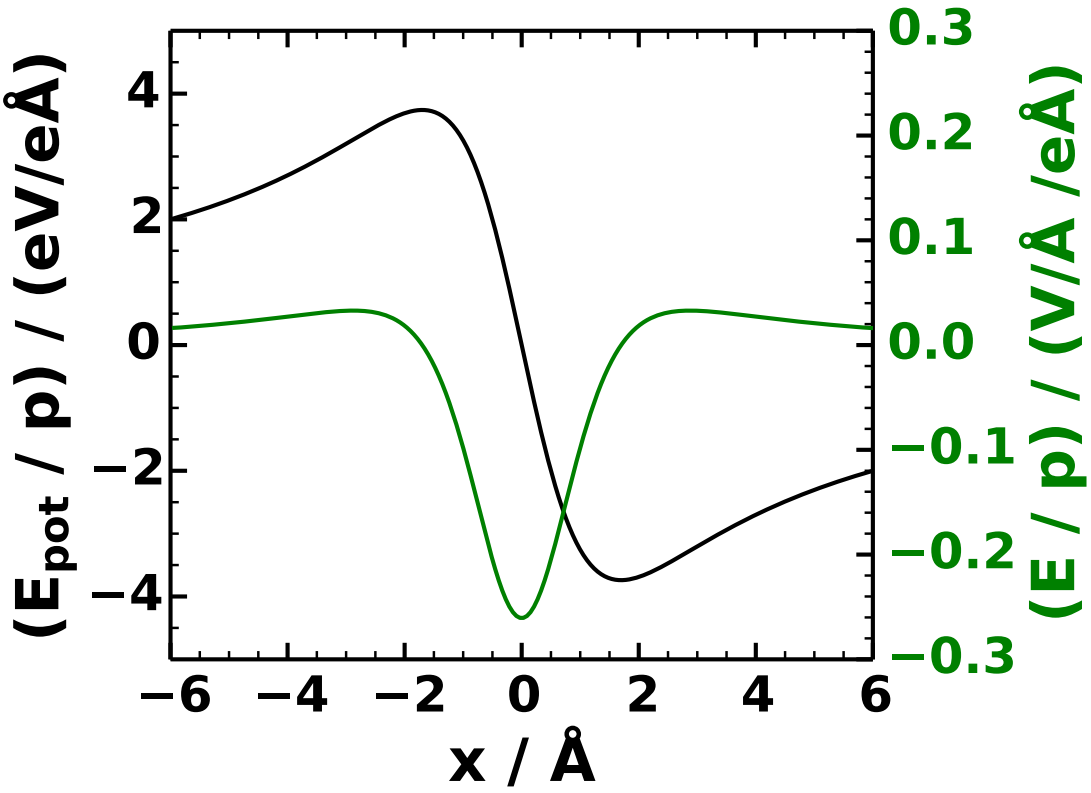

Figure 2.5.: Electron potential energy per unit dipole moment E_{pot}/p (black line, left axis) and the corresponding electric field E/p (green line, right axis) that dipoles arranged in a line at $y = \pm b, \pm 2b, \pm 3b, \ldots$ create at $y = 0$. The lattice constant $b = 2\,\text{Å}$ was used. For the full dipole line, a dipole would be sitting at $x = 0$, $y = 0$. The validity of the point dipole approximation in this case is not obvious, however the qualitative behavior should be correct.

2.3. Screening

This section follows chapter 17 of the book by Ashcroft and Mermin [20] and chapter 11.7 of the book by Gross and Marx [21].

2.3.1. Introduction

The electrostatic potential caused by charged impurities (and as a special case also dipoles) in a metal is *screened* by its electrons, a process that is mediated by the electron-electron interactions.

The total potential ϕ includes the "external" potential ϕ_{ext} and an induced potential ϕ_{ind} stemming from the rearrangement of the electrons. Then the "external" potential ϕ_{ext} acting on the electrons in a system is linearly related to the total potential ϕ according to

$$\phi_{\text{ext}}(\mathbf{r}) = \int d\mathbf{r}'\, \varepsilon(\mathbf{r}-\mathbf{r}')\phi(\mathbf{r}'). \tag{2.25}$$

Here, the *dielectric function* $\varepsilon(\mathbf{r}-\mathbf{r}')$ was introduced. The electrons are treated as a free electron gas. By means of the Fourier transform, this relation can be rewritten as

$$\phi(\mathbf{k}) = \frac{1}{\varepsilon(\mathbf{k})}\phi_{\text{ext}}(\mathbf{k}), \tag{2.26}$$

where the $\mathbf{k}$-dependent functions are the Fourier transforms of the $\mathbf{r}$-dependent functions. Now the key quantity is the "dielectric constant" $\varepsilon(\mathbf{k})$, which is $\mathbf{k}$-dependent due to inhomogeneities of the fields involved.

2.3.2. Thomas-Fermi Screening Theory

The basic assumption of Thomas-Fermi theory is that the dispersion relation of electrons in solids reads

$$E(\mathbf{k}) = \frac{\hbar^2}{2m}k^2 - e\phi(\mathbf{r}). \tag{2.27}$$

Due to the very nature of quantum mechanics (namely the Heisenberg uncertainty principle), this equation can only be understood as describing electrons in forms of *wave packets*. The width of these wave packets in real space will be on the length scale of k_F^{-1}, the inverse Fermi wave vector. The total potential $\phi(\mathbf{r})$ should thus not vary too much on this length scale. A *slowly varying* total potential is a central requirement for the applicability of Thomas-Fermi screening.

In general, the electron density $n(\mathbf{r})$ is given by the expression

$$n(\mathbf{r}) = \int \frac{d^3k}{4\pi^3} f(E(\mathbf{k})), \tag{2.28}$$

with the Fermi function

$$f(E) = \frac{1}{\exp\left(\frac{E-\mu}{k_B T}\right)+1}. \tag{2.29}$$

The role of the Fermi energy at finite temperature T is taken by the chemical potential μ. For zero potential, $\phi \to 0$, the electron density $n(\mathbf{r})$ is compensated by a positive background density n_0, given by

$$n_0(\mu) = \int \frac{d^3k}{4\pi^3} \frac{1}{\exp\left[\frac{1}{k_B T}\left(\frac{\hbar^2 k^2}{2m} - \mu\right)\right]+1}. \tag{2.30}$$

In presence of a potential ϕ, the dispersion relation $E(\mathbf{k})$ that appears in (2.28) is given by (2.27), which is technically equivalent to setting the chemical potential to $\mu \to \mu + e\phi(\mathbf{r})$ in (2.30). Now the induced charge density due to the potential ϕ is given by

$$\rho_{\text{ind}}(\mathbf{r}) = -e\left[n_0(\mu + e\phi(\mathbf{r})) - n_0(\mu)\right]. \tag{2.31}$$

The first of these two terms is the electron density, the second the background density.

This result, (2.31), is the foundation of *nonlinear Thomas-Fermi theory*. However, by linearizing it one obtains

$$\rho_{\text{ind}}(\mathbf{r}) = -e^2 \frac{\partial n_0}{\partial \mu} \phi(\mathbf{r}) =: \chi\, \phi(\mathbf{r}). \tag{2.32}$$

The dielectric constant $\varepsilon(\mathbf{k})$ is given by

$$\varepsilon(\mathbf{k}) = 1 - \frac{1}{\varepsilon_0 k^2}\chi = 1 + \frac{e^2}{\varepsilon_0}\frac{\partial n_0}{\partial \mu}\frac{1}{k^2} =: 1 + \frac{k_0^2}{k^2}, \tag{2.33}$$

where the Thomas-Fermi wave vector k_0 was defined.

2.3.3. Thomas-Fermi Screening of a Dipole

For the potential of a point charge and its Fourier transform,

$$\phi_{\text{ext}}(\mathbf{r}) = \frac{1}{4\pi\varepsilon_0}\frac{q}{r}, \qquad \phi_{\text{ext}}(\mathbf{k}) = \frac{q}{\varepsilon_0 k^2} \tag{2.34}$$

using (2.26) and (2.33) the total potential becomes

$$\phi(\mathbf{k}) = \frac{q}{\varepsilon_0(k^2 + k_0^2)}. \tag{2.35}$$

By applying the inverse Fourier transform, the potential of a screened charge comes out as

$$\phi(\mathbf{r}) = \frac{1}{4\pi\varepsilon_0}\frac{q}{r}\exp(-k_0 r). \tag{2.36}$$

Due to Thomas-Fermi screening, the potential of the point charge now has an additional exponentially decaying factor.

For a dipole, the potential is given as[3] (in analogy to (2.4)) [22]

$$\phi_{\text{dip}} = \frac{q}{4\pi\varepsilon_0}\left(\frac{e^{-k_0|\mathbf{r}-\mathbf{r}_+|}}{|\mathbf{r}-\mathbf{r}_+|} - \frac{e^{-k_0|\mathbf{r}-\mathbf{r}_-|}}{|\mathbf{r}-\mathbf{r}_-|}\right). \tag{2.37}$$

Again, the point dipole limit can be taken, which leads to [22]

$$\phi_{\text{dip}} \approx \frac{1}{4\pi\varepsilon_0}\frac{\mathbf{p}(\mathbf{r}-\mathbf{r}_0)}{|\mathbf{r}-\mathbf{r}_0|^3}e^{-k_0|\mathbf{r}-\mathbf{r}_0|}(1 + k_0|\mathbf{r}-\mathbf{r}_0|). \tag{2.38}$$

2.4. Graphene

Systems of graphite with very few layers are referred to as *graphene*. In this thesis, only single-layer graphene will be used and the term graphene always stands for single-layer graphene. Starting from 10 layers, the properties of the material are very similar to the bulk properties of graphite, and consequently systems of 10 or more layers are not called graphene anymore. [23]

While the first theoretical description of graphene dates back to the 1950s [24], then still in the context of explaining the electronic properties of graphite, the first isolation of graphene has not been achieved until 2004 [25]. For this ground-breaking work, performed using mechanical exfoliation from graphite, the Nobel prize 2010 in Physics was awarded to *Andre Geim* and *Konstantin Novoselov*. The predicted and observed structural and electronic properties are very unique and interesting, a fact that has led to a huge research interest in this novel material.

This chapter gives a fundamental overview of the structure and key electronic properties of graphene and graphene nanoribbons (sections 2.4.1, 2.4.2 and 2.4.3), following a review article [26] but including also some demonstrational calculations performed by myself. Then, from a more methodological point of view, the concept of supercells and Brillouin

[3] The assumption that the screening response to a dipole can be described as a superposition of the screening response to two charges is not obvious, but can be found in literature [22].

zone folding (section 2.4.4) and consequences of symmetries in graphene and their breaking (section 2.4.5) are explained. Finally, an overview over different approaches to modify the properties of graphene is given (section 2.4.6).

2.4.1. Structure

Graphene is a two-dimensional material with a hexagonal unit cell. The two lattice vectors are[4]

$$\mathbf{a}_1 = \frac{a}{2}\begin{pmatrix} 3 \\ \sqrt{3} \end{pmatrix} \qquad \text{and} \qquad \mathbf{a}_2 = \frac{a}{2}\begin{pmatrix} 3 \\ -\sqrt{3} \end{pmatrix}. \tag{2.39}$$

The carbon-carbon distance is $a = 1.42\,\text{Å}$. There are two carbon atoms in the unit cell (see figure 2.6), at

$$\begin{pmatrix} 0 \\ 0 \end{pmatrix} \quad \text{and} \quad \begin{pmatrix} a \\ 0 \end{pmatrix}. \tag{2.40}$$

This structure leads to a honeycomb lattice. Upon periodic replication, the two atoms in the unit cell give rise to two different sublattices. In unmodified graphene, the two atoms are equivalent, which is referred to as sublattice symmetry.

The C-C bond distance, 1.42 Å, is the experimental value. It is also possible to get the lattice constant from DFT calculations, either by using geometry optimization algorithms or by simply looking for the minimum of the total energy. An example of a calculation employing the latter method is found in figure 2.7 (this calculation was performed in the course of this thesis with VASP using the PBE functional as described in chapter 3.1). The bond distance thus obtained is within 10^{-2} Å of the experimental value, which can be considered a good agreement.

[4] In VASP, the order of the two lattice vectors has to be reversed to ensure a positive direct product.

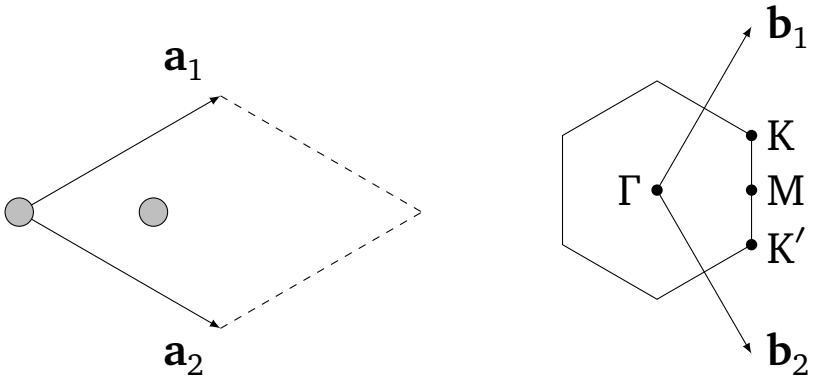

Figure 2.6.: Graphene unit cell (left) and first Brillouin zone (right).

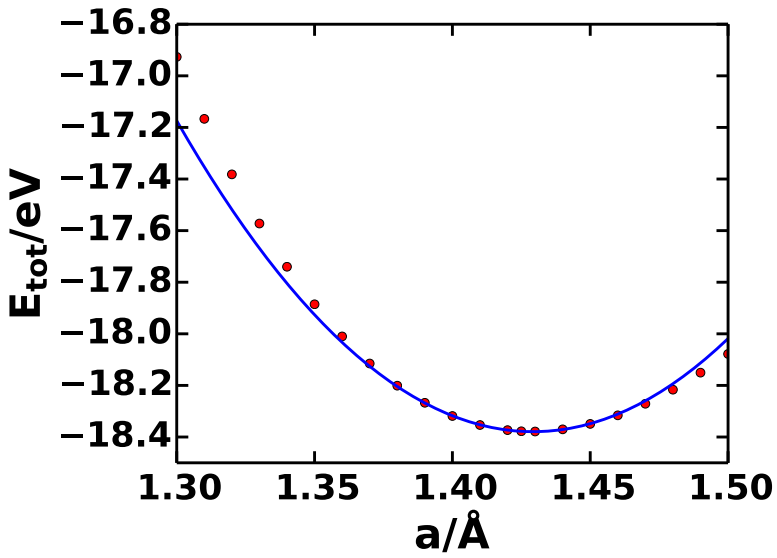

Figure 2.7.: Optimization of the graphene structure *by hand*: energy for different values of the lattice constant a. The solid line is a parabola fit around the minimum (taking into account the values between $a = 1.39\,\text{Å}$ and $a = 1.45\,\text{Å}$), leading to a fit function $E_{\text{tot}}(a) = 72.138(a - 1.429)^2 - 18.379$ (for E_{tot} in eV, a in Å). (The calculation was performed in the course of this thesis as described in chapter 3.1, but with a plane wave energy cutoff of 273.911 eV and Gaussian smearing *SIGMA* = 0.3 eV.)

In reciprocal space, the lattice vectors are given by

$$\mathbf{b}_1 = \frac{b}{3}\begin{pmatrix} 1 \\ \sqrt{3} \end{pmatrix} \qquad \mathbf{b}_2 = \frac{b}{3}\begin{pmatrix} 1 \\ -\sqrt{3} \end{pmatrix},$$

with $b = 2\pi/a$. The first Brillouin zone is hexagonal as well, the high symmetry points are the Γ, K and K′ and the M point (see figure 2.6):

$$\Gamma = \begin{pmatrix} 0 \\ 0 \end{pmatrix}, \quad \mathrm{K} = \frac{2\pi}{3a}\begin{pmatrix} 1 \\ 1/\sqrt{3} \end{pmatrix}, \quad \mathrm{K}' = \frac{2\pi}{3a}\begin{pmatrix} 1 \\ -1/\sqrt{3} \end{pmatrix}, \quad \mathrm{M} = \frac{1}{2}(\mathrm{K}+\mathrm{K}') = \frac{2\pi}{3a}\begin{pmatrix} 1 \\ 0 \end{pmatrix}. \tag{2.41}$$

This geometry is the root of several fascinating structural properties of graphene: Measurements of the breaking strength [27] have revealed that it is the strongest material known to mankind. Before the isolation of graphene, the existence of a flat two-dimensional infinitely extended crystal at finite temperature was believed to be impossible. [28, 29] However, the existence of isolated graphene sheets seems to disprove this statement. In an attempt to reconcile these two points, height fluctuations in graphene were proposed to play a crucial role in the thermodynamic stability of the material. [30, 31] Alternatively, graphene could be the manifestation of a metastable structure that is obtained from a three-dimensional (and thus stable) geometry. [32]

2.4.2. Electronic Structure

The most interesting feature in the band structure (see figure 2.8) is the *Dirac cone* at the K point. That means that the π bands at this point disperse linearly around the Fermi level, forming a cone in the three-dimensional energy landscape in k-space. The only point where the occupied and unoccupied bands touch is the K (and by time-reversal symmetry[5] also the K′) point. In other words, the Fermi surface consists of only six points in the first Brillouin zone. Graphene is thus neither a metal (the density of states is zero at the Fermi level) nor a semiconductor (there is no band gap): it is called a *semimetal* (or a gapless semiconductor).

The linear dispersion can be described using *massless Dirac fermions* (using the relativistic massless Dirac equation). The role of the spin in the Dirac equation is played by a pseudospin that describes the sublattice structure of the π wavefunction (i. e. bonding or antibonding π orbital; whether or not the p_z orbitals at the different sublattice sites are in phase of out of phase). The projection of the momentum operator along the pseudospin direction is called the helicity of the eigenfunctions and basically identical to their chirality (this is true only for massless particles). [34] One interesting consequence of the relativistic nature of graphene electrons is the *Klein paradox* (see also Ref. [35]): Under certain conditions, there is total transmission (i. e. no backscattering) through a potential barrier (Klein tunneling).

[5] Time-reversal symmetry implies that the states at $\mathbf{k}$ and $-\mathbf{k}$ have the same energy. [33]

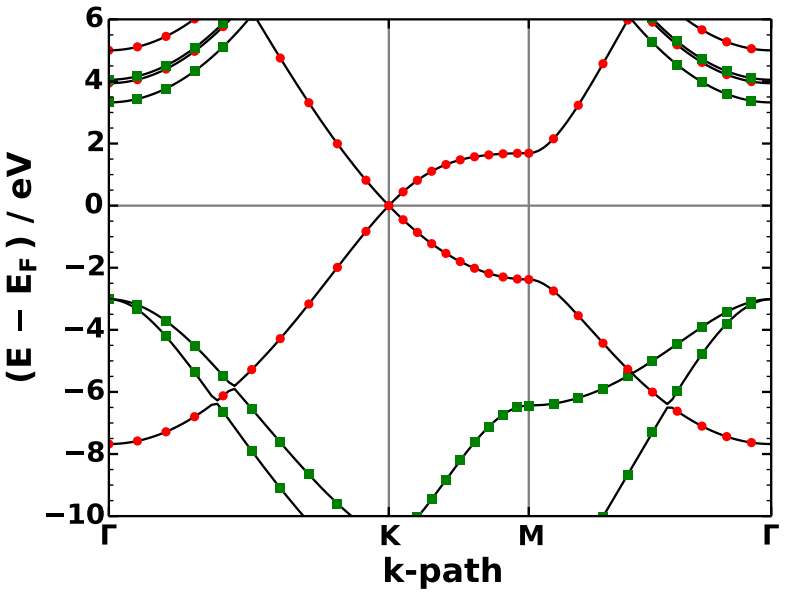

Figure 2.8.: Kohn-Sham band structure of pure graphene along the high symmetry directions (see Brillouin zone in figure 2.6). Red circles mark bands with mainly π character, green squares mark bands with mainly σ character. (Own calculation, for methodology see chapter 3, plane wave energy cutoff: 273.911 eV.)

The lack of backscattering is due to the conservation of pseudospin (because pseudospin flip processes are rare).

Another interesting effect happens when one tries to confine electrons in graphene: then the electron-hole symmetry is broken and the so-called *Zitterbewegung* occurs. This is a trembling motion of the charge carriers due to the interaction of the positive and negative energy branches. [36]

Graphene has an extraordinarily high *mobility* and ballistic transport can be observed up to very high length scales. An effective mass of the electrons in graphene (not to be confused with the Dirac quasiparticles which are massless) can be given: while the definition typically used in semiconductor physics (involving the second derivative of energy with respect to k) does not hold because the dispersion around the Fermi energy is not parabolic, the cyclotron mass is still a meaningful quantity. It is given by [37]

$$m^* = \hbar^2 k \left(\frac{\partial E}{\partial k} \right)^{-1}. \tag{2.42}$$

Let's now turn to another key property of all solids, the *density of states* (DOS), see figure 2.9. As mentioned above, the DOS goes to zero at the Fermi level. Close to the Dirac point, it depends linearly on the energy. At about 2 eV above and below the Fermi level, van Hove singularities appear.

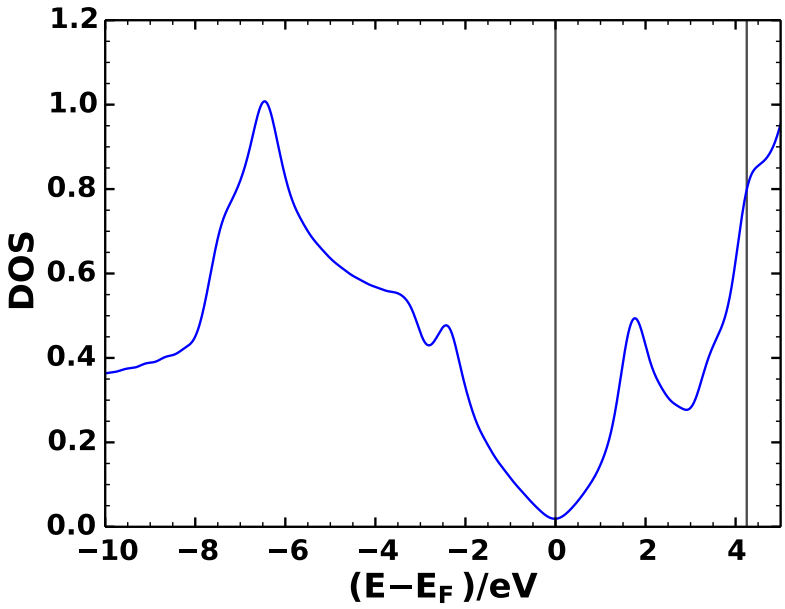

Figure 2.9.: Density of states per unit cell of pure graphene. The Fermi and the vacuum level are marked by vertial lines. The values above the vacuum energy are not reliable. (Own calculation, for methodology see chapter 3, plane wave energy cutoff: 273.911 eV.)

2.4.3. Graphene Nanoribbons

Graphene strips of finite width are known as *graphene nanoribbons* (GNR). When cutting the strip out of a graphene layer, in principle every direction is possible. However, often two important directions are considered, namely the zigzag (ZZ) and the armchair (AC) direction, see figure 2.10. Finite size effects lead to finite band gaps, which are bigger for narrower strips.

For AC-GNR, the dependence of the band gap on the width of the ribbon is more complex: The width is usually given by the number of dimer lines N ($N = 9$ in the AC-GNR in figure 2.10). The behavior of the decrease of the band gap with increasing strip width is qualitatively different for the three cases where $N = 3p$ (i. e. it is a multiple of three), $N = 3p + 1$ and $N = 3p + 2$, see figure 2.11. [38] Furthermore, typically in ZZ-GNR, spin-polarization occurs, which leads to magnetic edge states near the Fermi level.

In simple tight binding calculations, the different GNR geometries have a far greater impact on the electronic structure (to the point where metallic behavior is found). However, by using more accurate calculations, it can be shown that this is not the case. [39, 40] Also in experiment, finite band gaps are measured for all orientations. [41, 42]

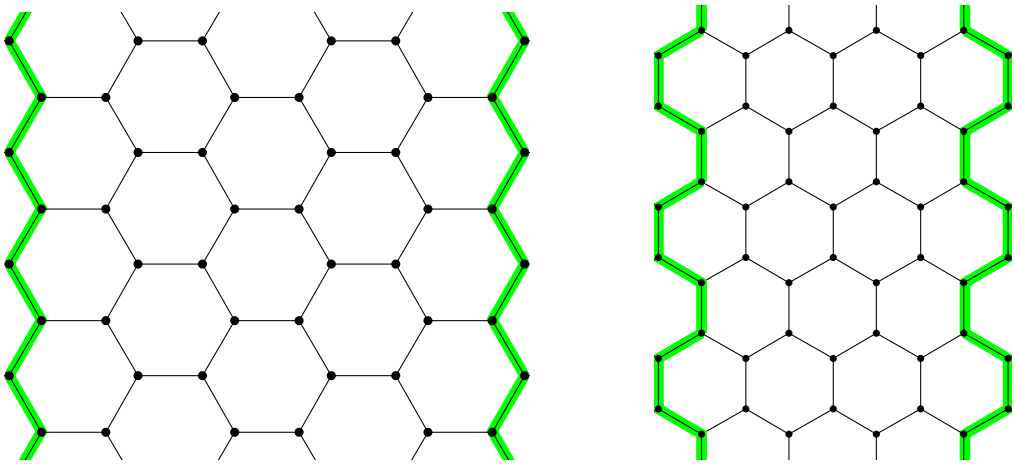

Figure 2.10.: Graphene nanoribbons with zigzag (left) and armchair (right) edges.

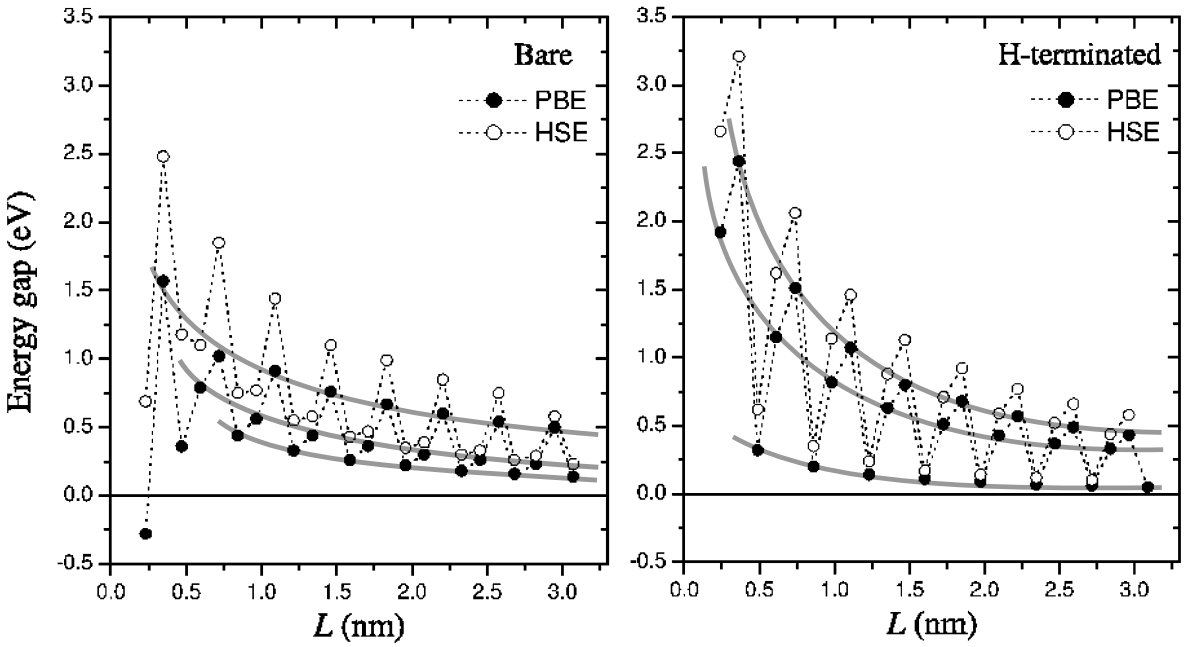

Figure 2.11.: "Dependence of the band gap on the ribbon width for bare (left panel) and hydrogen-terminated (right panel) armchair CNRs [=AC-GNR]." [38] The gray lines to visually accentuate the three different kinds of qualitative behavior were added by me. Adapted with permission from V. Barone, O. Hod, and G. E. Scuseria. "Electronic Structure and Stability of Semiconducting Graphene Nanoribbons". *Nano Letters* **6,** 2748 (2006) (figure 2). Copyright 2006 American Chemical Society.

2.4.4. Supercells and Brillouin Zone Folding

When taking multiple unit cells along the direction of a unit cell vector, a supercell consisting of several primitive unit cells is formed. The real space unit cell vector increases by an integer factor f, the reciprocal unit cell vector now shrinks by a factor $1/f$. Naturally, the size of the first Brillouin zone (BZ) reduces accordingly. The bands are *back-folded* from the original BZ to the new BZ, thus increasing the number of bands there. Obviously this also leads to more band crossings than before.

For example, if one multiplies the unit cell by two in each direction (i.e. one constructs a 2×2 supercell), the BZ shrinks by a factor of two in each direction. The area of the new BZ is one quarter of the area of the original BZ. However, the bands of the larger BZ are folded back into the smaller BZ, multiplying the number of occupied bands by four. The resulting band structure is a superposition of the original and the back-folded bands (see figure 2.12).

Apart from going from one hexagonal unit cell to another, bigger hexagonal unit cell, it is also possible to build a *rectangular supercell* (see figure 2.13). It contains four atoms and its area is twice the area of the hexagonal primitive unit cell. For simplicity, the $\mathbf{a}_1$-direction is called x-direction and the $\mathbf{a}_2$-direction is called y-direction. Now also the first Brillouin zone is rectangular, with the high symmetry points X and Y. Due to Brillouin zone folding, the K point of the hexagonal system is at $2/3$ of the way from Γ to Y in the rectangular system (see figure 2.14).

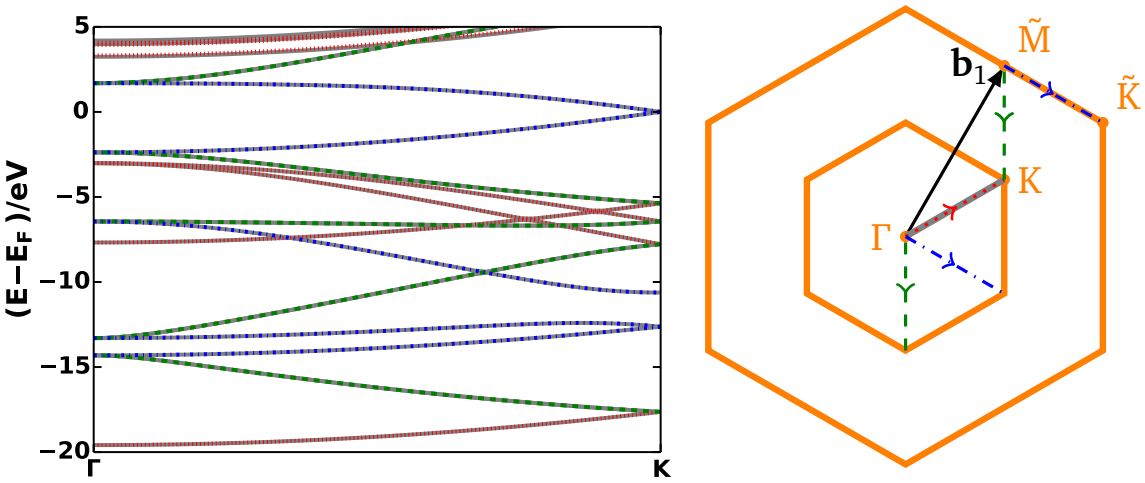

Figure 2.12.: Left: Kohn-Sham band structure (line from Γ to K) of a 2×2 graphene unit cell (gray lines), on top the corresponding lines of a 1×1 unit cell (Γ to K, $\tilde{\text{M}}$ to K and $\tilde{\text{M}}$ to $\tilde{\text{K}}$). (Own calculation, for methodology see chapter 3, plane wave energy cutoff: 273.911 eV.) Right: 1×1 and 2×2 Brillouin zones. The three lines (red, green, blue) in the smaller Brillouin zone are all equivalent to the Γ-K line (by symmetry). If shifted by the reciprocal lattice vector $\mathbf{b}_1$, (this is a reciprocal lattice vector of the 2×2 unit cell, i. e. it corresponds to the smaller BZ), the green line becomes equivalent to $\tilde{\text{M}}$-K and the blue line becomes equivalent to $\tilde{\text{M}}$-$\tilde{\text{K}}$. This means that the lines $\tilde{\text{M}}$-K and $\tilde{\text{M}}$-$\tilde{\text{K}}$ get back-folded onto Γ-K in the bigger unit cell (smaller BZ).

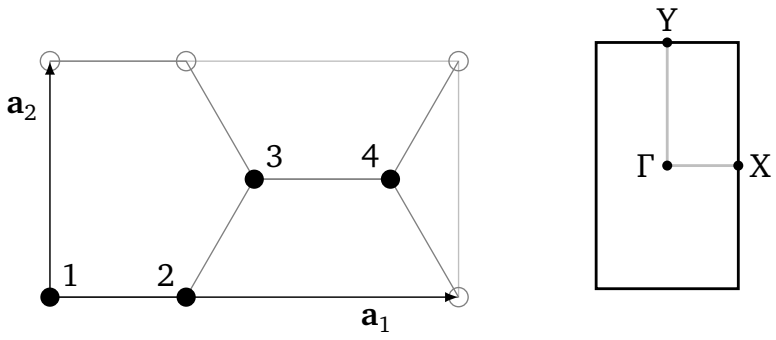

Figure 2.13.: Rectangular unit cell of graphene (left), containing four atoms. The corresponding first Brillouin zone (right).

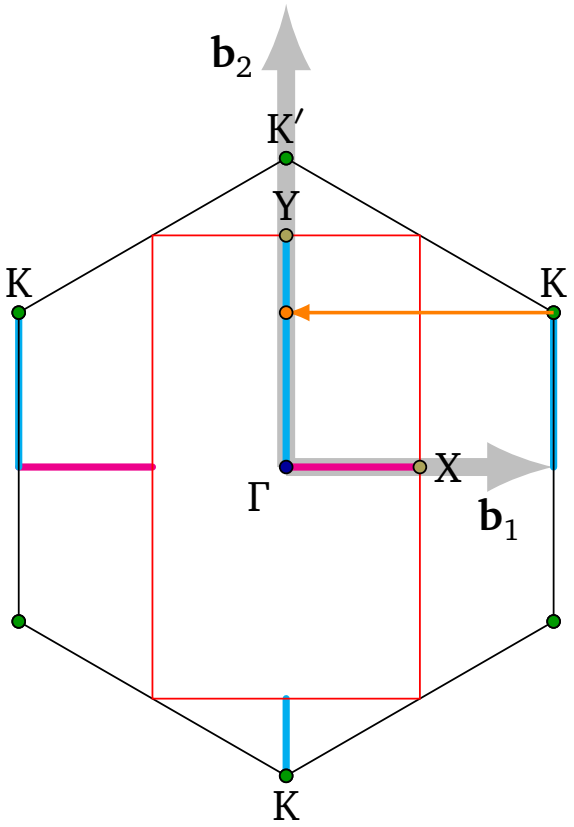

Figure 2.14.: First Brillouin zone of the primitive hexagonal graphene system (black line) and of the rectangular system (red line). Inside the red rectangle, there are two lines: a cyan line going from Γ to Y and a magenta line from Γ to X. We now want to investigate which lines of the big hexagonal BZ are back-folded onto these two lines. Two points (or lines) in k-space that are connected with a reciprocal lattice vector (i. e. $h\mathbf{b}_1 + k\mathbf{b}_2$ with integers h, k) are equivalent. We thus shift the cyan and magenta line from the rectangular BZ along different reciprocal lattice vectors to get all the equivalent lines in the BZ of the hexagonal system. These are the cyan and magenta lines outside the red rectangle. They mark the paths through k-space that get back-folded onto the original cyan and magenta line in the rectangular BZ. For instance, going from Γ to Y is equivalent to going 3/4 of the way from Γ to K′ and 1/4 of the way from K to Γ and from M to K. The orange arrow (the vector $-\mathbf{b}_1$) shows that the K point gets backfolded onto 2/3 of the way from Γ to Y.

2.4.5. Symmetries

This section explains the symmetries of graphene following a paper by Malterre *et al.* [43] (first paragraph) and then describes own calculations that demonstrate the consequences of symmetry breaking on the band structure.

Graphene belongs to the plane symmetry group p6mm (see figure 2.15). This means that around the K point there is a 3-fold rotational axis with a mirror plane associated to it (symmetry C_{3v}). This symmetry leads to a degeneracy of the bands at the K point, i. e. there is no band gap possible. A breaking of this symmetry, e. g. by asserting a difference between the two lattice sites as it is found in hexagonal boron nitride (hBN), lowers the symmetry at the K point to C_3. Thus, the bands are not degenerate any more, a band gap can form.

An easy way of examining how a certain change of symmetry affects the band structure is by a simple tight binding calculation (taking into account only nearest-neighbor hopping). The asymmetry is then created by assigning different on-site energies to the different orbitals (atomic sites). This was done using the freely available tight binding code `PythTB`[6] [45]. A rectangular graphene unit cell was used, see figure 2.13. The hopping parameter t describes nearest-neighbor hopping (equal irrespective of the sites involved in the hopping process). The different sites can have different on-site energies ε_i. For the present study, the magnitude of all the ε_i was given by $\delta = 0.1t$. In figure 2.16 you can see the result for three different symmetries regarding the ε_i: At first (figure 2.16a), all sites are equivalent, the bands are degenerate at the K point and at X and Y. By introducing an asymmetry between the A and B sublattices (figure 2.16b), a gap opens at the K point (as described above). An asymmetry regarding the atoms at $y = 0$ in the rectangular unit cell and the atoms at $y = a_2/2$ leads to a splitting of the energies at X and Y (figure 2.16c).

[6] This code, written by the David Vanderbilt group at Rutgers University, is a Python program that allows the calculation of band structures and Berry phases based on the tight binding approach. It can be downloaded from the website `http://www.physics.rutgers.edu/pythtb/index.html`. Here, version 1.6.2 was used.

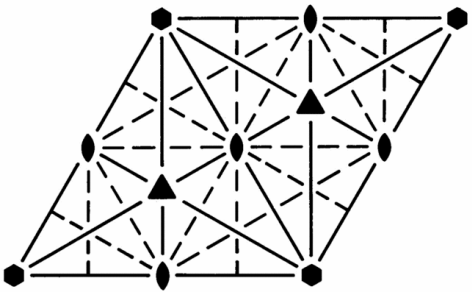

Figure 2.15.: Symmetry elements of the planar space group p6mm. Source: [44]

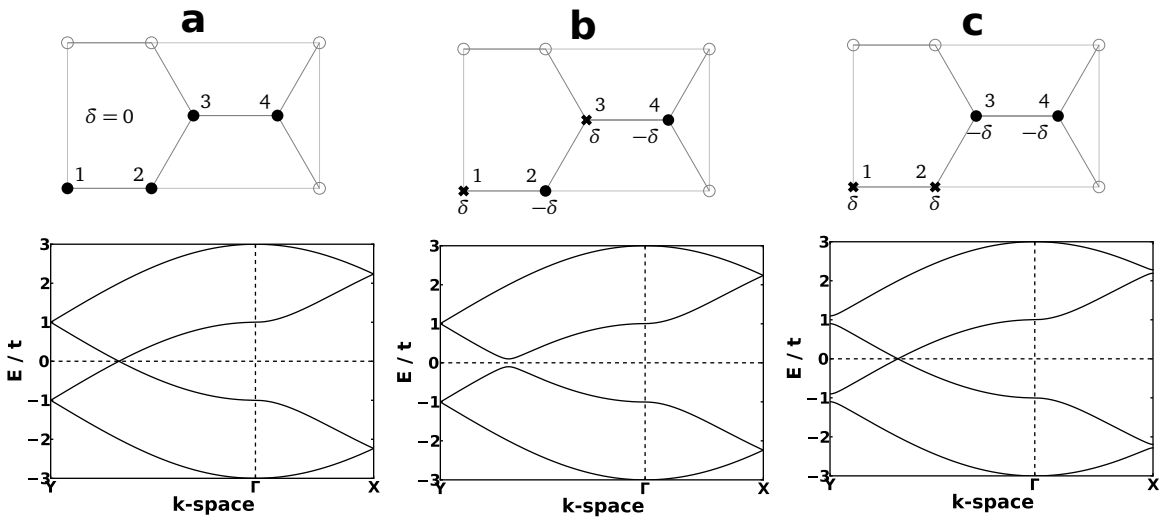

Figure 2.16.: Tight binding calculation of graphene taking into account only the nearest neighbors and an on-site energy $\delta = 0.1t$. For the left band structure (a), all the $\varepsilon_i = 0$. For the band structure in the middle (b), we have $\varepsilon_1 = \delta$, $\varepsilon_2 = -\delta$, $\varepsilon_3 = \delta$, $\varepsilon_4 = -\delta$ (see unit cell above the band structure), i.e. the A sublattice has a positive on-site energy, the B sublattice has a negative on-site energy. The right band structure (c) has $\varepsilon_1 = \varepsilon_2 = \delta$ and $\varepsilon_3 = \varepsilon_4 = -\delta$. The K point of the hexagonal Brillouin zone of graphene can be found by going 2/3 of the way from Γ to Y.

2.4.6. Modified Graphene

Since its discovery, many attempts have been made to influence and tune the properties of graphene. Most of the literature found today consists of proposed ways of graphene modifications backed by ab-initio calculations, although also some experimental investigations exist.

One of the main goals is building integrated circuits out of graphene. This, however, is difficult due to the lack of a band gap. [46] Therefore, many of the proposed modifications of graphene discussed below aim at opening a band gap in graphene.

A means already discussed above is confinement of the electrons by construction of graphene nanoribbons. This gives rise to magnetic edge states [47, 48] and can open a band gap [42, 49]. It has been proposed to functionalize the edges of GNRs using different chemical groups [50–52], leading for example to increased half-metallicity [53], other magnetic phenomena or tunable band gaps [52].

Applying stress to graphene leads to a distortion of the lattice, which changes electronic properties like the band gap. [54, 55]

Chemical doping is widely used, for instance in semiconductors, to influence key electronic properties of materials. Naturally, it can also be successfully applied to graphene. For example, substitutional doping with Al, Si, P and S is expected to open a gap [56].

The adsorption of different molecules can also have doping effects (e. g. CrO_3 [57] should lead to a doping induced band gap opening and F4TCNQ [58] leads to *p*-type doping). Also single atoms can adsorb on graphene: To name just a few examples, Bi, Sb and Au were experimentally shown to lead to *p*-type doping [59] and 3d transition metal atoms are expected to change the magnetic properties of graphene [60]. A substantial change of the electronic structure of graphene can also be achieved by covalent functionalization of graphene using aryl groups. [61]

Using different substrates supporting the graphene layer is another promising way to open a band gap due to defect formation [62] or the formation of so-called moiré superlattices. [63]

Sheets of graphene mixed with hexagonal boron nitride (hBN), forming a material with graphene and hBN domains, also appears interesting from a band-gap engineering point of view. [64, 65] Also applications of this approach for devices have been proposed. [6] A different way of combining graphene and other two-dimensional materials is van der Waals heterostructure stacking [66], where layers of different materials are put onto each other. [67] Due to the vast number of possible combinations, materials with many different properties seem possible.

The application of an external electric field allows field-effect tuning especially in multilayer graphene. [68, 69] Also field-effect doping is proposed to lead to potential applications of graphene. [25, 70]

Of course, this short overview cannot summarize all the findings of the more than 30000

published papers[7] on graphene in the last ten years but should rather give an impression about the diversity of approaches for evolving the development of graphene-based materials.

[7] according to Thomson Reuters Web of Science, September 16, 2014

3. Methodology

This chapter explains how the calculations were done and analyzed.

Nearly all of the data analysis was performed using the Python packages SciPy [71] and NumPy [72]. Nearly all of the plots were produced with the Matplotlib package [73].

3.1. Single Point Calculations

The quantum mechanical simulations were performed using density functional theory (DFT, see chapter 2.1) with the Vienna Ab initio Simulation Package (VASP) [74–77] code in the 5.3.3 version with extensions by Tomáš Bučko[1]. The Perdew-Burke-Ernzerhof (PBE) functional [11, 78] was employed. The atomic potentials were treated using the projector augmented wave (PAW) method [79], as implemented in VASP [80], using the "soft" pseudopotentials unless noted otherwise (for details see table 3.1). If no different value is indicated, a plane wave cutoff energy, which determines the size of the basis set, of 279.692 eV (= 20.557 Ry) was chosen in accordance with the value recommended by VASP.

For self-consistent calculations, a Γ-centered Monkhorst-Pack [81] *k*-point grid was used. For a simple graphene unit cell, the convergence of the total energy with respect to the

[1] For some members of our group, these extensions are necessary to get correct results. To stay consistent within our group, also here this modified version of VASP was used, although the modifications should have no impact on the results presented here.

Table 3.1.: Titles (as found in the `POTCAR` files) of the used pseudopotentials for the different atoms. The maximum recommended plane wave energy cutoff *ENMAX* is given as well.

Element	Title of used potential	*ENMAX*/eV
H	PAW_PBE H_s 15May2010	200.000
Be	PAW_PBE Be 06Sep2000	247.543
B	PAW_PBE B_s 22Jan2003	269.245
C	PAW_PBE C_s 06Sep2000	273.911
N	PAW_PBE N_s 07Sep2000	279.692
O	PAW_PBE O_s 07Sep2000	282.853

number of k-points was tested (see chapter 3.4); a $21 \times 21 \times 1$ grid was found to be sufficient. For larger supercells, the number of k-points was scaled down accordingly.

For the occupation scheme, a smearing method (`INCAR`-tag *ISMEAR*) has to be chosen. While the VASP manual [82] recommends the tetrahedron method with Blöchl corrections, for supercells this leads to noise in the density of states due to the large number of band crossings. Consequently, the Gaussian smearing method with a width of $SIGMA = 0.01\,\text{eV}$ (for most of the calculations) was applied. This has the advantage that the resulting density of states can easily be "resmeared" for visualization purposes by convolving it with another, broader Gaussian function (with a width $SIGMA_{\text{resmearing}}$). If a width of $SIGMA_{\text{desired}}$ is wanted, the following $SIGMA_{\text{resmearing}}$ has to be used (where *SIGMA* is the value used in the `INCAR` file):

$$SIGMA_{\text{resmearing}} = \sqrt{SIGMA^2_{\text{desired}} - SIGMA^2}. \tag{3.1}$$

The standard deviation σ used in the usual definition of the Gaussian normal distribution $\mathcal{N}$

$$\mathcal{N}(x; x_0, \sigma) = \frac{1}{\sqrt{2\pi\sigma^2}} \exp\left(-\frac{(x-x_0)^2}{2\sigma^2}\right) \tag{3.2}$$

is related to the VASP-*SIGMA* by

$$SIGMA = \sqrt{2}\sigma. \tag{3.3}$$

In most DOS-plots shown in this thesis, the density of states was calculated with $SIGMA = 0.01\,\text{eV}$ and then plotted after "resmearing" it with $SIGMA_{\text{desired}} = 0.3\,\text{eV}$.

As VASP is a three-dimensionally periodic code, stricty two-dimensionally periodic systems cannot be simulated. However, this can be circumvented by introducing a large vacuum region in the z-direction, with a sufficiently large lattice vector length in that direction so that the periodic replicas do not interact any more[2]. In the present case, 20 Å turned out to be adequate (see figure 3.3). This procedure is called the *slab approach*.

If there is a dipole moment pointing towards the z-direction in such a slab, this leads to a shift of the vacuum level (see chapter 2.2.3). This is not compatible with periodic boundary conditions, so by default such a shift is compensated by a homogeneous electric field across the whole unit cell. Obviously, this can cause artefacts. Thus, a better strategy is to introduce a compensating dipole jump in the vacuum region. This has to be done self-consistently until the dipole strength of the compensation dipole layer is converged[3].

A set of typically used input files is shown in appendix A.

[2] While chemical interactions are only acting on a short range, the electrostatic fields of polar elements in the layers still have effects on a longer range. Therefore the convergence of the considered quantities with respect to the vacuum gap used has to be investigated. This will be done in chapter 3.4.

[3] Reaching convergence with dipole correction is always a bit tricky. In the present calculations (where dipole corrections were required, which was only the case for molecules adsorbed on graphene), it turned out to be necessary to use a vacuum gap of 40 Å instead of 20 Å to achieve convergence.

3.2. Geometry Optimizations

Due to the use of the Born-Oppenheimer approximation, single point DFT calculations work with fixed ion positions. However, it is possible to move the atoms around (according to a geometry optimization algorithm) and perform single point calculations for each configuration until a convergence criterion is met. Typically, this criterion will be that the maximum force acting on the ions falls below a certain threshold; alternatively, the total energy can be minimized.

While VASP comes with several ionic relaxation algorithms, the usage of Cartesian coordinates is not always ideal: sometimes, large movements of parts of the geometry are required, which can be more accurately described by internal coordinates (such as bond lengths and angles). There is a tool called GADGET [83] built around VASP that allows geometry optimizations in internal coordinates. Furthermore, certain constrictions (like constant bond lengths, angles, lattice vectors, etc.) can be enforced. Usually, the geometry was optimized with GADGET until the maximum gradient was below 0.01 eV/Å. A template for a GADGET input file can be found in appendix A.3.

For molecules adsorbed on graphene, the positions of the carbon atoms in the graphene sheet were held fixed while the atoms belonging to the molecule were allowed to move.[4] Unfortunately, structure relaxations where the substrate molecules are allowed to move are computationally not feasible with our present resources. As *van der Waals interactions* typically play a significant role when it comes to adsorption, they have to be somehow included in the calculation. The van der Waals method by Tkatchenko and Scheffler (vdW-TS) [84] successfully and computationally inexpensively corrects the total energy after the SCF cycle. It was, therefore, used (in the implementation included in VASP [85]) for the ionic relaxations of molecules on graphene.[5]

To obtain reasonable starting guesses for the molecule geometries, they were pre-optimized using the Gaussian code [86] with the PBEPBE functional and the 6-311G(d,p) basis set. Again, a sample input file can be found in appendix A.4.

3.3. BN-substituted graphene

The system that a large portion of this thesis focuses on is a graphene sheet where selected neigboring carbon atoms are replaced by pairs of boron and nitrogen atoms. Starting from the rectangular unit cell of graphene (figure 2.13), a rectangular $N \times 1$ supercell is constructed. Then two neighboring carbon atoms are replaced by a pair of a boron and a nitrogen atom. Each of the BN pairs forms a *dipole*, where the boron atom is the negative and the nitrogen atom is the positive end[6]. By replacing another pair of carbon atoms by an

[4] This is done using *Selective Dynamics* in the `POSCAR` file.
[5] This is achieved using the *IVDW*=2 tag in the `INCAR` file.
[6] This is not true for BN bonds in general, but for BN in a graphene-like conjugated structure.

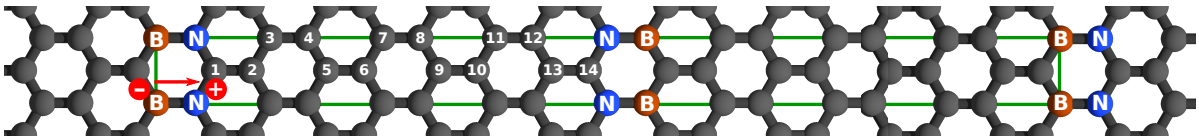

Figure 3.1.: BN pair-substituted graphene: the green rectangle marks the the unit cell (i. e. due to the periodic boundary conditions the BN pairs form an infinitely extended line along the y-direction). The BN pairs form dipoles as indicated by the red arrow. The size of the unit cell in x-direction is determined by the number of C atoms between the two N atoms (14 in this particular system, numbered atoms) and the number of C atoms between the two B atoms (counted analogously, also 14 here).

oppositely oriented BN pair, a strip of graphene in-between these dipole lines is formed[7].

An example for one of these systems can be found in figure 3.1. This system has two oppositely oriented BN pairs per unit cell and a certain number of C atoms in between. The number n of C atoms between the N atoms does not necessarily have to be the same as the number b of C atoms between the B atoms. When describing a system, the short notation "BN-nC-NB-bC" is used. The symmetric system arranged in figure 3.1 would then be called BN-14C-NB-14C.

The unit cell of a BN-nC-NB-bC system is based on is a $(\frac{n+b}{4}+1)\times 1$ rectangular graphene supercell.

For large system sizes, a full geometry optimization is not feasible. Therefore, a full relaxation in the xy-plane was performed (with GADGET) for a BN-22C-NB-22C system. Then, carbon atoms were added (or removed) in the middle between the BN pairs with a C-C distance of 1.42 Å until the desired number of C atoms was reached.[8]

All the dipoles of the individual BN pairs in the infinitely (due to the periodic boundary conditions) extended line give rise to a collective electrostatic effect as described in chapter 2.2.2. Of course, the dipoles are depolarizing each other, as discussed in chapter 2.2.5. Therefore only the effective dipole moment will be considered here.

3.4. k-Point and Vacuum Gap Convergence

Choosing a sufficiently large number of k-points is crucial for the validity of band structure results. For a two-dimensional material like graphene using the slab approach, the unit cell is very large in z-direction with only vacuum. Any interaction in the z-direction is

[7] This has the advantage that the unit cell has no net dipole moment, which might lead to problems due to the three-dimensionally periodic boundary conditions.

[8] The reason why even for smaller systems no separate relaxation was performed is that if you have a BN-nC-BN-bC strip where $n < 22$ and $b > 22$, one cannot be consistent otherwise.

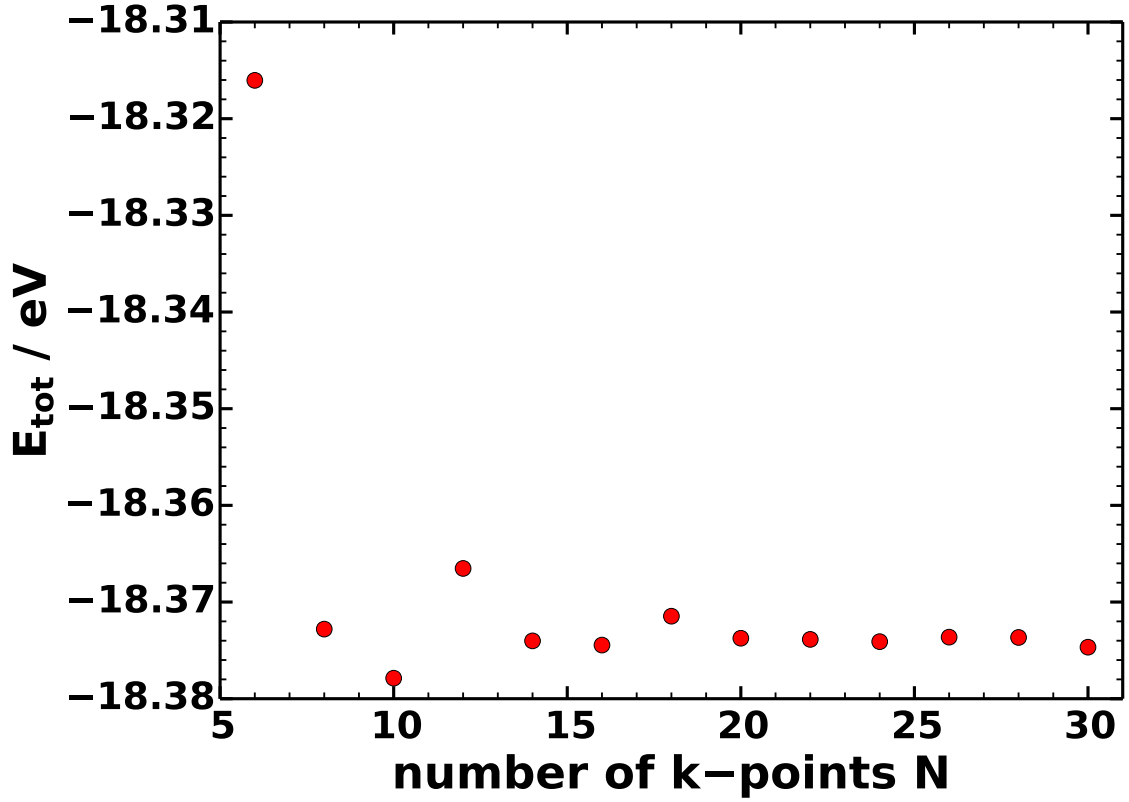

Figure 3.2.: Total energy of graphene as a function of the number of k-points in $\mathbf{b}_1$ and $\mathbf{b}_2$-direction (i. e. for a $N \times N \times 1$ k-point grid). (Plane wave energy cutoff: 273.911 eV.)

not wanted and therefore only one k-point should be used in the $\mathbf{b}_3$-direction. However, in the $\mathbf{b}_1$ and $\mathbf{b}_2$-directions, tests have to be performed to ensure the convergence of the calculation with respect to the k-point grid. This is done by calculating the total energy for $N \times N \times 1$ k-point grids with different numbers of N and comparing these energies (see figure 3.2).

It can be seen that the total energy is well converged at 20 k-points per direction already. In order to include the K point in the calculation (which obviously is advisable because most of the interesting physics of graphene happens there), the number of k-points per direction has to be a multiple of three. Thus $21 \times 21 \times 1$ k-points is a good choice.

For a nice sampling of the DOS, more k-points can be necessary. In principle, there are three possibilities: doing the whole self-consistent calculation with more k-points (which usually is computationally expensive), doing a self-consistent calculation first with the minimal converged number of k-points and then a non self-consisting calculation with more k-points or resmearing the DOS with a rather high σ (which is the least accurate method). For pure graphene, as a compromise, the self-consistent calculation was performed with $42 \times 42 \times 1$

k-points (owing to the small system size this could be done reasonably fast) followed by resmearing the DOS.

When using the slab approach, the size c of the unit cell in z-direction is a freely choosable parameter. However, too small values of c lead to an interaction of the slab with its periodic replicas, while too high values of c lead to unnecessarily long calculations. Figure 3.3 shows the electron potential energy at the core of the C atoms[9] in a BN-pair substituted graphene system. The x-dependence of E_{pot} shows the typical shape stemming from the dipole lines (which will be thoroughly discussed in chapter 4.2). However, what matters here is that the data points for a vacuum gap of 20 Å, 40 Å and 80 Å lie on top of each other, which means that 20 Å of vacuum are sufficient.

[9] This average E_{pot} at the core of the ions is evaluated in VASP by integrating the local potential in a sphere around the ion position. In chapter 3.5, this will be explained and examined further.

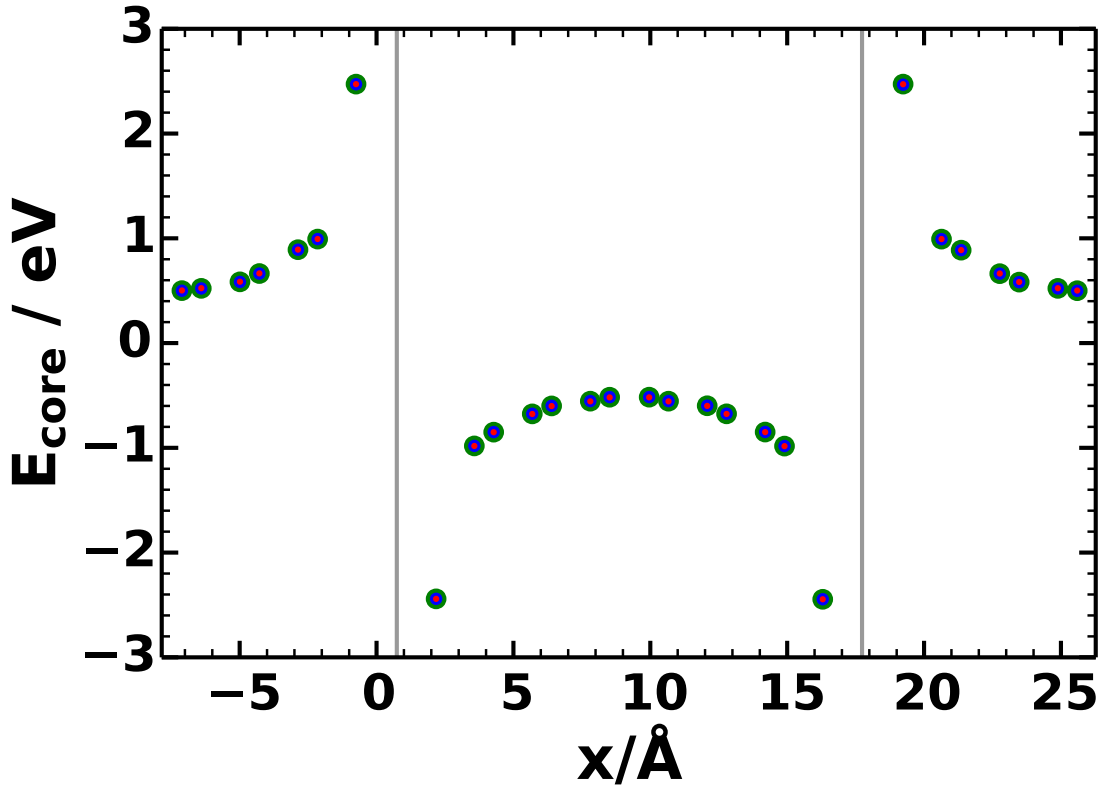

Figure 3.3.: Electron potential energy at the core of the carbon atoms in a BN-14C-NB-14C system relative to its mean value (for a discussion of this system and the shape of the potential see chapter 4). The green points are the values for a vacuum gap of 80 Å, the blue points for 40 Å and the red points for 20 Å. The position of the dipoles is marked with gray lines. The maximum difference of a core potential is 5 meV between the 20 Å and 80 Å case.

3.5. Avoiding Artefacts in the Local Potential

The electron potential energy E_{pot} plays a crucial role in the DFT self-consistent loop and is thus calculated in every simulation. VASP can then write out the local electron potential energy on a real space grid in the file `LOCPOT`. The *LVHAR*-tag should be set to true in the `INCAR` file to just write the ionic and Hartree contributions, but not the exchange-correlation contributions[10], of E_{pot}.

During the calculation, fast Fourier transforms (FFT) are performed on grids. Obviously, the grid spacing (i. e. the number of grid points per unit cell) has to be carefully chosen to avoid errors. VASP offers the *PREC* tag to easily switch between different levels of accuracy. While for most calculations the "normal" precision should be sufficient, the "accurate" value should be chosen if one is interested in the local potential. Otherwise, wrap-around (i. e. aliasing) errors are expected (see figure 3.4).

However, sometimes this is not sufficient and by looking at E_{pot} one can see that there are artefacts. While it is in principle possible to increase the number of FFT grid points to absurdly high values, this is not economical. Moreover, the default maximum number of grid points per dimension is 4096 – this value can be changed in the VASP source code, but this is not recommended.

In the case of a supercell where there is a periodicity (at least as a good approximation) with a smaller lattice constant a_{small} than the nominal lattice constant a, the number of FFT grid points should be chosen to be an integer multiple of a/a_{small} to get a nicely looking E_{pot} (as shown in figure 3.4). Especially for optimized geometries, this sub-periodicity does often not exist.

When one is not interested in the heavily oscillating E_{pot}, but it is sufficient to get the value of E_{pot} (up to an arbitrary constant) at the position of each atom, there are two additional possibilites that give nice results not suffering from aliasing problems. Firstly, VASP offers values for the average electrostatic potential at each ion, i. e. E_{pot} integrated over a sphere around the ion and reports it in the `OUTCAR` file. Secondly, the initial state approximation [87] can be used to calculate the 1s core levels of the individual atoms (this corresponds to X-ray photoelectron spectroscopy (XPS) measurements) using the *ICORELEVEL* tag in VASP. Then, for atoms of the same element the relative shift of the core level can be attributed to chemical and electrostatic effects. A comparison of the different methods is found in figure 3.5.

[10] These contributions cause the potential to look noisy and should thus not be plotted along with the other contributions of the potential.

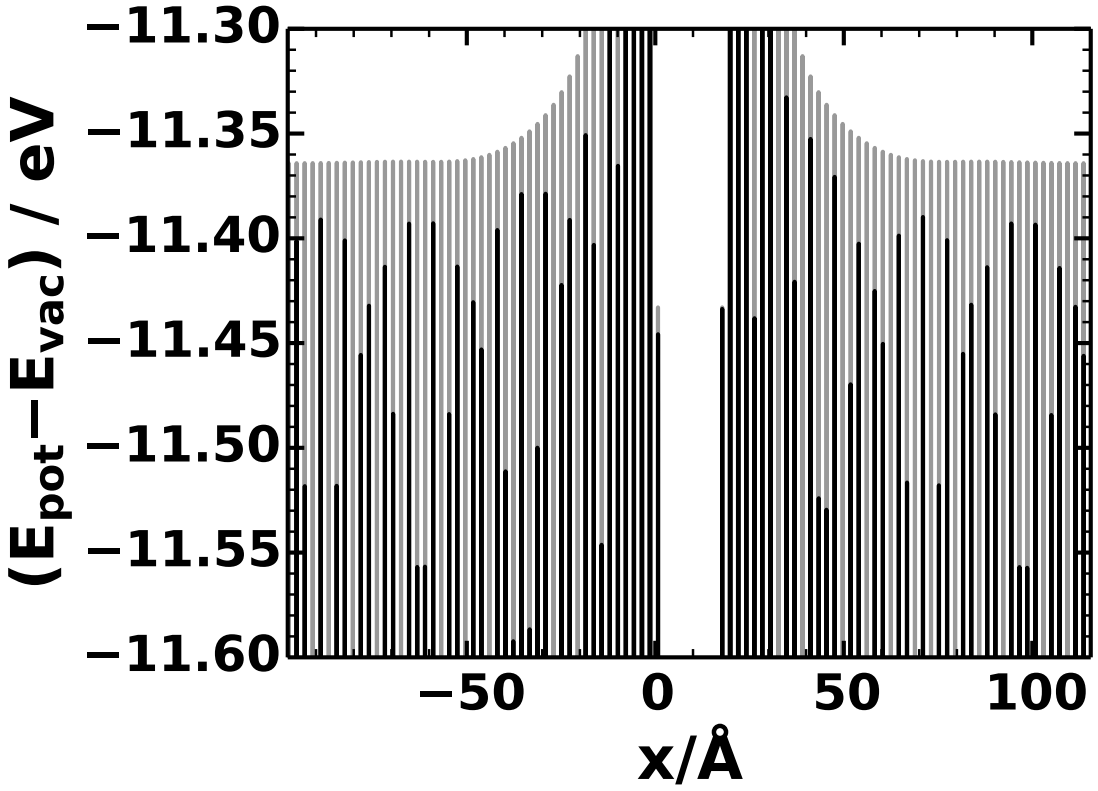

Figure 3.4.: Electron potential energy of a BN-14C-NB-182C system (geometry not optimized, all bond lengths set to 1.42 Å) in the graphene plane, averaged along the y-direction. The gray curve is E_{pot} calculated by making use of the sublattice periodicity (this is only possible for non-relaxed systems). The black curve is E_{pot} for the same system, but with *PREC*=Normal, showing strong aliasing effects. Both curves are aligned at the vacuum level.

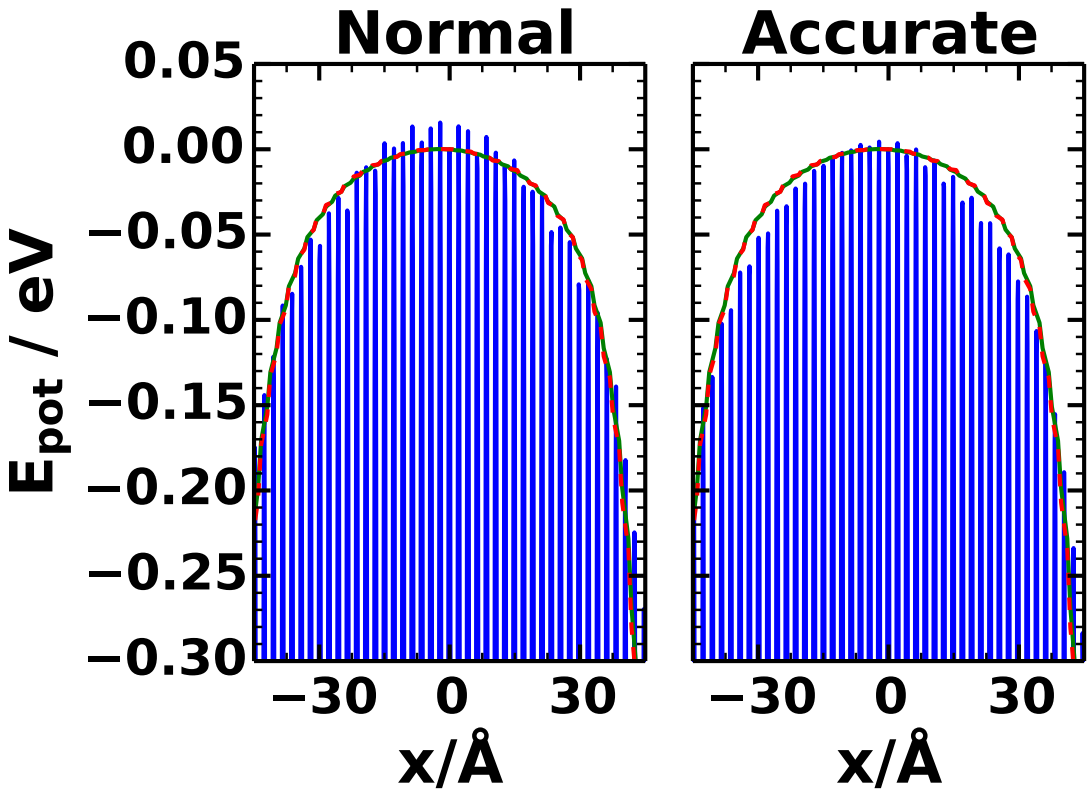

Figure 3.5.: Electron potential energy for a BN-98C-NB-98C system (see chapter 4 for a detailed description of these kinds of systems) calculated with normal (left) and accurate (right) precision. The data found in the `LOCPOT` file was plane-averaged in the yz-direction (blue line). The green line is the smooth average electrostatic potential at each ion and the red dashed line is the C 1s core level (in both plots). The tree different lines were aligned so that the value at $x = 0\,\text{Å}$ is identical and at 0 eV.

3.6. Fitting the Local Potential

The local electron potential energy E_{pot} of a BN-pair substituted graphene sheet, averaged along the yz-plane to be only x-dependent, should have the form of the E_{pot} of an infinite line of dipoles. Consider a system that has a dipole line at $x = 0$ and one at $x = x_0$, where x_0 is much lower than the lattice constant a (in x-direction). Then the system of two dipole lines is reasonably well decoupled from the next periodic replica in x-direction. The non-periodic model system for describing this situation consists, thus, of four dipole lines, one at $x = 0$, one at $x = x_0$, one at $x = a$ and one at $x = a + x_0$. The latter two are necessary because the right end of the unit cell does feel hardly anything from the first two dipole lines, but is mainly influenced by their periodic replica. Had the unit cell boundary been chosen so that the influence of the dipole lines on the unit cell boundary is negligible, two dipole lines would have sufficed.

Now the smooth, yz-plane-averaged, E_{pot} obtained from the quantum mechanical calculation (typically obtained by the XPS method explained in section 3.5) in the whole unit cell can be fitted to an electrostatic model of four dipole lines. The position of each of the four dipole lines was chosen to be the mean of the x-coordinates of the B and N atoms constituting the dipole (from the quantum mechanical calculation). The model E_{pot} is thus given by (using the result from (2.9))

$$E_{\text{pot}}^{\text{model}}(x) = \frac{1}{4\pi\varepsilon_0} \sum_d \sum_{i=-\infty}^{\infty} \frac{p_d(x - x_d)}{(x - x_d)^2 + (-ib)^2)^{3/2}} + V_0. \tag{3.4}$$

The sum over d is the sum of the four dipole lines, positioned at x_d with a dipole moment p_d. In order to fit to the quantum mechanical values, a physically irrelevant constant background V_0 has to be added. The absolut values of the dipole moments should be equal, so $p_d = f_d p$, where $f_d = \pm 1$ is the correct sign for the dth dipole line. Then one obtains

$$E_{\text{pot}}^{\text{model}}(x) = p\frac{1}{4\pi\varepsilon_0} \sum_d \sum_{i=-\infty}^{\infty} \frac{f_d(x - x_d)}{(x - x_d)^2 + (-ib)^2)^{3/2}} + V_0. \tag{3.5}$$

This model definition includes the two fitting parameters p and V_0 that can be determined using a least-squares fit of the data from the quantum mechanical calculation.

It turns out that an exponential ansatz is better suited for describing the potential. This was chosen in accordance to the result obtained for Thomas-Fermi screening (see section 2.3) although the central requirements[11] are not fulfilled. While the Thomas-Fermi model for screening is therefore a very crude approximation, the exponential ansatz it motivates is successful for fitting the quantum-mechanical results. To include this additional screening,

[11] These are a parabolic density of states, a slowly varying total potential and a three-dimensional system.

the model has to be changed, according to (2.38). One then obtains

$$E_{\text{pot}}^{\text{model,TF}}(x) = p\frac{1}{4\pi\varepsilon_0}\sum_d \sum_{i=-\infty}^{\infty} \frac{f_d(x-x_d)}{(x-x_d)^2+(-ib)^2)^{3/2}} e^{-k_0|x-x_d|}(1+k_0|x-x_d|)+V_0. \quad (3.6)$$

Now the fitting parameters are p, V_0 and the "Thomas-Fermi screening constant" k_0.

A program to calculate the potential of a dipole line is found in appendix B.

3.7. Calculating the Shift of a PDOS

One of the main effects to be investigated in this thesis is the energy shift of the projected density of states (PDOS) $d(E)$ with respect to the DOS of pure graphene $d_G(E)$. Now, we want to find a value for the energy shift ΔE so that

$$d(E+\Delta E) = d_G(E). \quad (3.7)$$

This equation will never hold perfectly because $d(E)$ is not only a shifted graphene DOS, but the result of an entirely different calculation (involving a chemically different system). We take the values of the pure graphene DOS between $-10\,\text{eV}$ and $5\,\text{eV}$ (there are 2143 points in that interval with the parameters chosen as in appendix A) as data to fit to. Then we linearly interpolate between the values of $d(E)$ to be able to evaluate $d(E+\Delta E)$ for any ΔE. Using a least squares fit, the quantity

$$\chi^2 = \sum_i (d_G(E_i) - d(E_i+\Delta E))^2 \quad (3.8)$$

is minimized[12].

Figure 3.6 shows an example of how well the shifted PDOS then agrees with the DOS of pure graphene.

[12] The least squares fit was performed using the function `scipy.optimize.curve_fit`, taken from the Scipy Python library [71]. The energy shift ΔE was taken as the fit parameter.

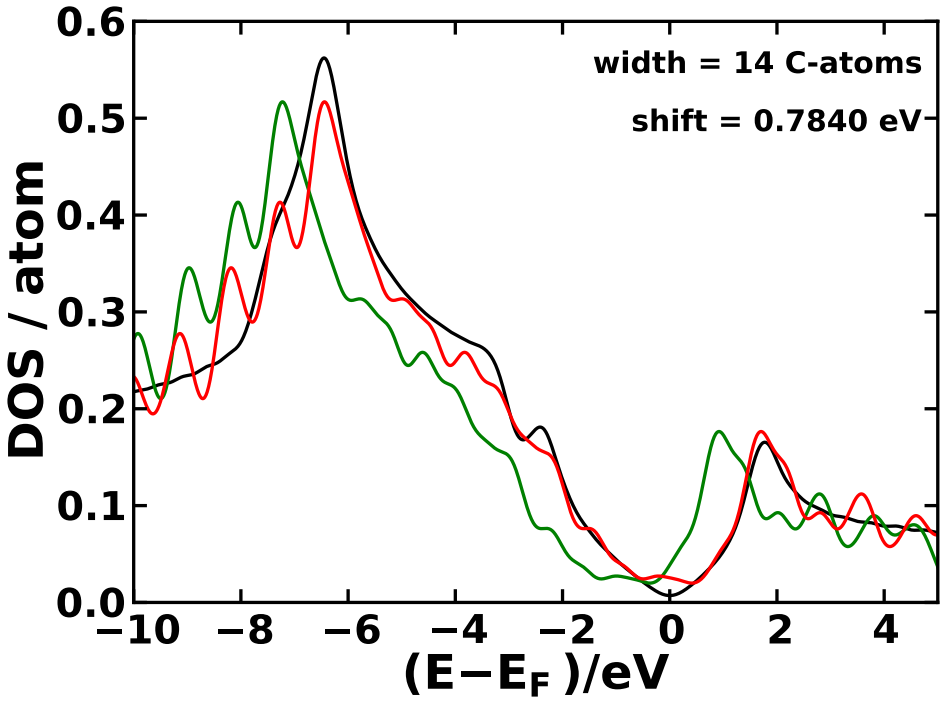

Figure 3.6.: Average PDOS of the C atoms between the BN and NB pairs in a BN-14C-NB-182C system (green line, for a detailed description of this system see chapter 4) compared to the DOS per atom of graphene (black line). The red line shows the same data as the green line, but shifted in energy by $\Delta E = 0.78\,\text{eV}$ towards higher energy, so that it lies on top of the pure graphene DOS. The value of the shift has been determined by a least squares fit. It is thus possible to conclude that the PDOS of the C atoms in the BN-substituted system is shifted by 0.78 eV towards lower energies.

3.8. Bandstructure and Localization

Using the resulting charge density of a self-consistent DFT calculation, the Kohn-Sham (KS) energies at certain, additional k-points typically in the first Brillouin zone are calculated non-selfconsistenly[13]. When these KS energies are plotted along k-paths (often in high symmetry directions), the typical band structure plots are obtained. While, strictly speaking, this is not correct, because the KS energies are fundamentally different from what is usually known as band structure, it is common to use them as an approximation (in zeroth order of the electron-electron interaction [88]) to the real band structure.

Furthermore, VASP has no way of detecting which KS energies at which k-points belong to the same band. According to the VASP definition, at every k-point the KS energies are sorted and then the lowest is called band number one, the next band number two, etc.

It is possible to calculate the electron density (as a function of the position in the unit cell) separately for each k-point and band[14]. This can also be interpreted as the local density of states (LDOS) for this k-point and band. When this k-point resolved band-projected LDOS is then integrated over different spatial regions, the localization of the state represented by this point in the band structure can be examined.

3.9. Charge Rearrangements

It is important to calculate how the distribution of the electrons changes when a bond[15] forms between the substrate (graphene sheet) and an adsorbed molecule. These charge rearrangements give rise to a bond dipole in z-direction which, due to the periodicity of the system, leads to a change of the vacuum energy (as for every two-dimensional array of dipoles, see chapter 2.2.3).

The following discussion follows Ref. [89]. In order to calculate the charge rearrangements, three calculations have to be performed: the whole system (substrate and molecule), the substrate alone and the molecule alone (but in the same geometry and position that it would have in the whole system). Then the charge rearrangements are

$$\Delta\rho(z) = \rho(z) - (\rho_{\text{graphene}}(z) + \rho_{\text{molecule}}(z)), \tag{3.9}$$

[13] This is done by adding ten to the value of the *ICHARG* tag in the `INCAR` file – typically *ICHARG*=11 will be used. The resulting `CHGCAR` file of a self-consistent run is needed as input.

[14] With the `WAVECAR` of a non-selfconsistent calculation of the band structure, calculate the partial charge density `PARCHG` using *LPARD=.TRUE.*, specify the numbers of the bands of interest with *IBAND= <band-numbers>*, turn on separate evaluation for these bands using *LSEPB=.TRUE.*, turn on separate evaluation of k-points with *LSEPK=.TRUE.* and specify certain k-points with *KPUSE= <k-point numbers>* (or combine just certain tags, as needed) in the `INCAR` file.

[15] Here, bond is to be understood in the general sense of binding behavior and adsorption. The presence of a chemical bond is not implied.

where the z-dependent xy-plane-integrated values for the charge densities of the whole system (graphene and adsorbed molecule) ρ, of the graphene layer alone ρ_{graphene} and the molecule alone ρ_{molecule} are used. For each value of z, the quantity $Q(z)$ gives the amount of charge transferred from the region below z to the region above z. It can be obtained by the integral

$$Q(z) = \int_{-\infty}^{z} d\zeta \, \Delta\rho(\zeta). \tag{3.10}$$

Negative values of $Q(z)$ mean that electrons flow upwards while positive values mean that electrons flow downwards. The corresponding electron potential energy E_{bond} due to the bond dipole can be calculated by solving the Poisson equation

$$\frac{d^2}{dz^2} E_{\text{bond}}(z) = \frac{e}{\varepsilon_0} \Delta\rho. \tag{3.11}$$

In practise and in the present (VASP) units we get

$$E_{\text{bond}}(z[\text{Å}])[\text{eV}] = -\frac{4\pi \cdot 27.11652}{A[\text{Å}^2]} 0.5291772108 \int_{-\infty}^{z} d\zeta \, Q(\zeta)[-\text{e}]. \tag{3.12}$$

Furthermore, this bond dipole potential can be calculated using the electron potential energy Φ for the different parts of the system:

$$E_{\text{bond}}(z) = \Phi(z) - (\Phi_{\text{graphene}}(z) + \Phi_{\text{molecule}}(z)) + C. \tag{3.13}$$

A physically irrelevant constant shift C is included to ensure the equality of the two values of E_{pot} obtained by (3.12) and (3.13), because the electron potential energies of the three systems are ususally not aligned to a common level.

The three-dimensional charge rearrangements are calculated in analogy to (3.9) as

$$\Delta\rho(x,y,z) = \rho(x,y,z) - (\rho_{\text{graphene}}(x,y,z) + \rho_{\text{molecule}}(x,y,z)). \tag{3.14}$$

4. Graphene with BN Pairs

As a proof of principle for modifying graphene with collective electrostatic effects stemming from dipole lines, graphene with substitutional pairs of boron and nitrogen atoms (BN pairs) is examined. The geometry of these systems is introduced in chapter 3.3. The results of a geometry optimization are presented in section 4.1. Then the consequences of the introduction of dipole lines in the form of BN pairs are investigated. These comprise:

- change of the electron potential energy (section 4.2)
- shift of the energy of electronic states in graphene and its manifestation in the atom-projected and local DOS as well as the localization of the occupied and unoccupied states in different spatial regions (section 4.3)
- changes in the band structure and k-point- and band-resolved localization of the states (section 4.4).

Finally, different ways of incorporating BN pairs in graphene are tested and the influence on the properties are explained (section 4.5).

4.1. Geometry Optimization

The geometry used for BN-substituted graphene is explained in chapter 3.3.

When performing a structure relaxation (where the atoms can move in the xy-plane and the lengths of the unit cell vectors in x- and y-direction are allowed to change), it turns out that there is a slight distortion of the lattice due to the BN pairs. The bond between the boron and the nitrogen atom is longer than the C-C bond in graphene, measuring about 1.48 Å (see figure 4.1). The surrounding C-C bond lengths have values different from pure graphene, however far from the BN pairs they tend to a stable value (the pure graphene value). This also justifies the approach to construct larger systems from smaller, relaxed structures by adding extra carbon atoms with the pure graphene bond distance (as explained in chapter 3.3).

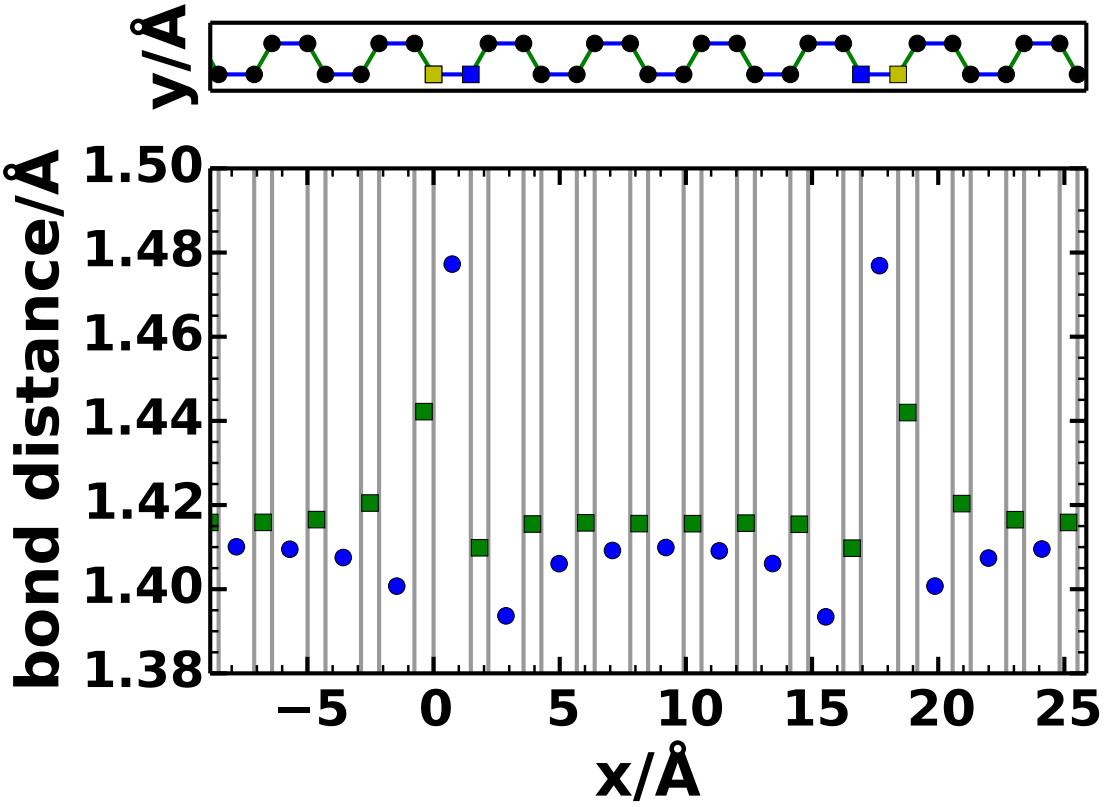

Figure 4.1.: Bond lengths (lower plot) of the different bonds in a BN-14C-NB-14C system (upper plot). In the lower plot, bonds that are pointing in the x-direction are indicated using blue circles, bonds pointing at a 60 degree angle using green squares. The atom positions are marked as vertical gray lines. In the upper plot, C atoms are shown as black circles, B atoms as yellow squares and N atoms as blue squares. Geometry as optimized by GADGET.

4.2. Potential

The dipole lines formed by the BN pairs change the electrostatic potential in their vicinity. This potential acts on the electrons, changing their local potential energy E_{pot} as a function of the location with respect to the dipole line. The central quantity is the shift of E_{pot} due to the presence of the dipole lines.

We will now consider the electron potential energy, averaged across the yz-plane, as a function of x, which can be found in figure 4.2. It is strongly oscillating because very near the ions, the electron potential energy is significantly lowered. However, the effects of the dipole lines can clearly be seen. The potential distribution in the y-direction can be seen from the two-dimensional plot in figure 4.2.

For a more quantitative and detailed analysis, the heavy oscillations are counterproductive. Thus, the potential at the position of the individual atoms is probed by calculating the energy of the C 1s state (as described in section 3.5). The resulting data can be seen in figure 4.3. An atom not affected by the potential modification of the dipoles would be at an energy zero in that plot. The system consists of two oppositely oriented dipole lines per unit cell, with a narrow strip of graphene in-between. Now the electron potential energy for the atoms in this strip is consistently shifted from zero, by e. g. at least 0.5 eV for a strip width of 14 C atoms.

The data can be fitted by a *model function* for the electrostatic potential of a dipole line, as explained in section 3.6. Without a Thomas-Fermi-like exponential ansatz to take into account screening, the fit parameters are $p = 0.26\,\text{eÅ}$ and $V_0 = 0.01\,\text{eV}$. With screening, they are $p = 0.31\,\text{eÅ}$, $k_0 = 0.15\,\text{Å}^{-1}$ and $V_0 = 0.01\,\text{eV}$. Note that the dipole strength p is the resulting dipole moment of a BN pair embedded in graphene feeling the field of all the other BN pairs. It is, thus, an effective dipole moment. The curves resulting from the fits are presented in figure 4.3.

The model without considering screening fails to represent the data, especially in-between the two oppositely oriented dipole lines. As there are many data points far away from the dipoles where the modification of E_{pot} is nearly zero, this zero-level is well described by both fits. However, the strip region is far better represented by the model that accounts for Thomas-Fermi screening. In conclusion, a screening mechanism in addition to a linear screening (which is already accounted for by the effective dipole moment) plays an important role in graphene and can be well described using a model inspired by Thomas-Fermi theory.

The fitted value of the *Thomas-Fermi screening constant* k_0 allows an estimate for the characteristic length scale on which the potential drops when going away from a dipole line. This screening length is $1/k_0 = 6.75\,\text{Å}$. Therefore, for systems with a large strip width, the effect will eventually vanish. The investigated systems, thus, have to have very narrow strip widths, because the decrease of the potential modification does not follow a $1/r$, but rather an exponential behavior.

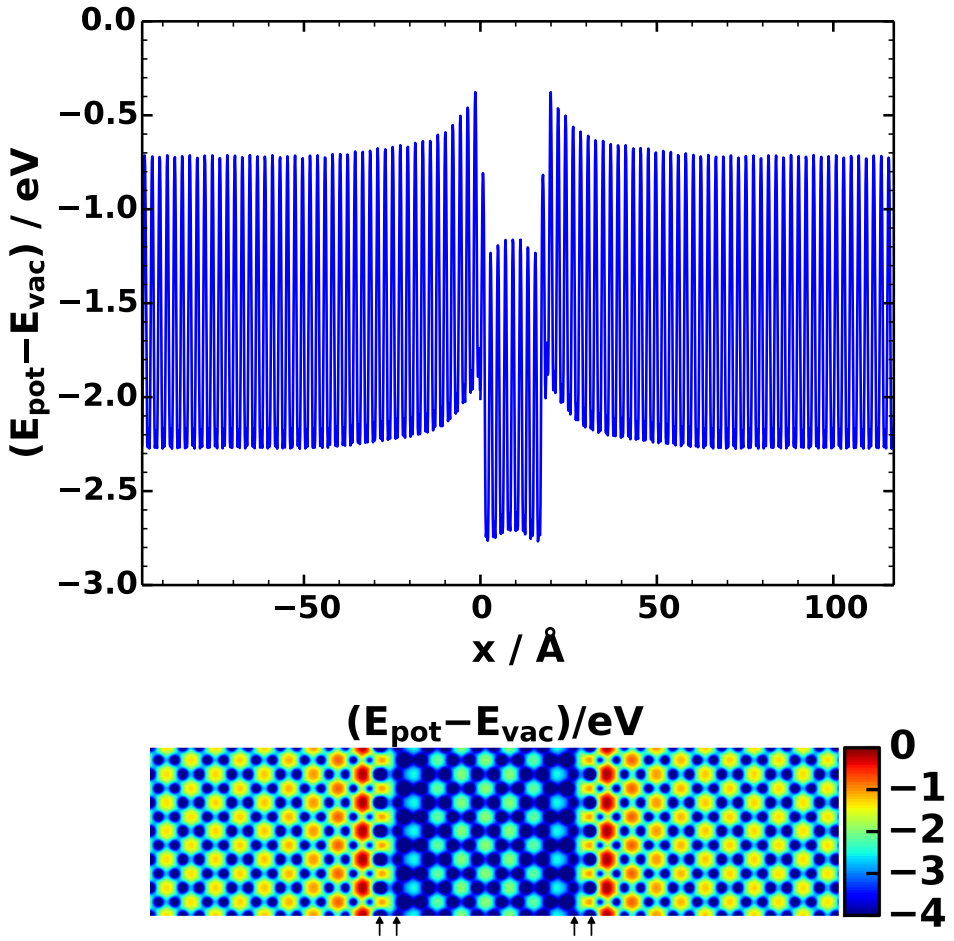

Figure 4.2.: Top: Electron potential energy averaged across the yz-plane of a BN-14C-NB-182C system. Bottom: Electron potential energy in the xy-plane at 1.07 Å (because E_{pot} is calculated on a finite grid by VASP, no "round" value could be used here without manually modifying the grid) above the graphene plane (in z-direction). The arrows mark the x-positions of the B, N, N and B atoms (from left to right).

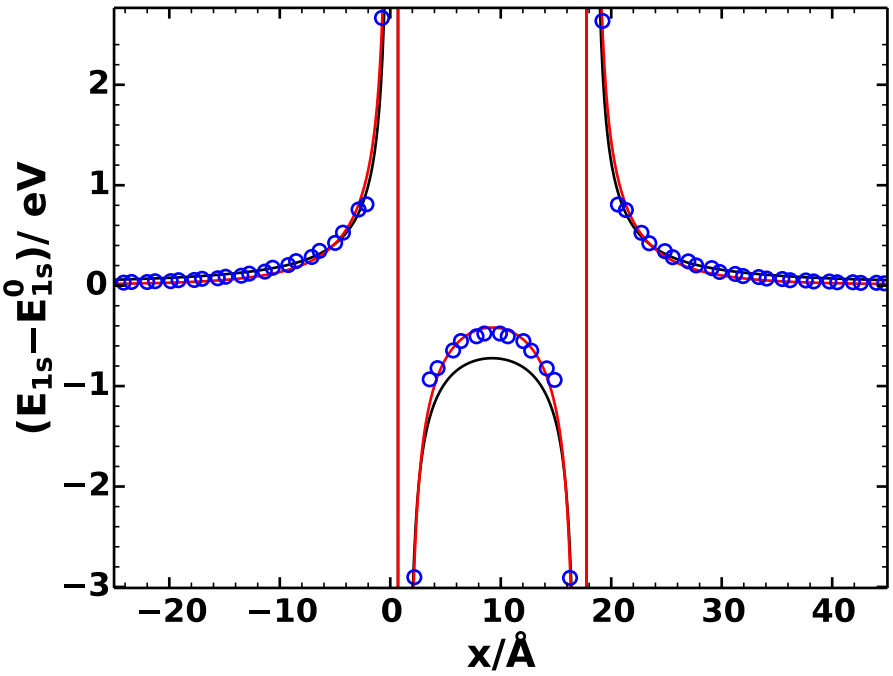

Figure 4.3.: Energy E_{1s} of the C 1s core level states (i. e. a probe for the electron potential energy) with respect to the C 1s core level electron potential energy E^0_{1s} of a C atom far from the dipole lines in a BN-14C-NB-182C system (blue circles). The energies are plotted as a function of the x-coordinate of the atom they belong to. The black line is the fit without Thomas-Fermi screening according to the model function (3.5), the red line is the fit with Thomas-Fermi screening according to (3.6). The position of the dipole lines in the unit cell are at $x = 0.74\,\text{Å}$ and at $x = 17.70\,\text{Å}$.

When comparing the electron potential energy of the valence electrons, as shown in figure 4.2, with the C 1s core level shifts (figure 4.3), it is obvious that both the valence and the core states are equally affected by the modifications. This, together with the fact that the electrostatic model (3.6) works so well, is already a strong hint that the observed effect does indeed stem from the dipole potential and is not a chemical effect caused by change of bonding due to the presence of heteroatoms in graphene. A further test also strongly supports this fact: The shift of the electron potential energy is expected to depend linearly on the dipole density (see the electrostatic model in chapter 2.2.2). The dipole density can easily be decreased by enlarging the unit cell in y-direction, but still having only one BN pair per unit cell. Then, when going along the dipole line, there is one BN pair and then one or more carbon pairs, before after one lattice constant in y-direction the next BN pair comes up. In figure 4.4, the dependence of the electron potential energy shift on the dipole density is plotted. For a dipole density of one third of the full dipole density and more, a nearly linear dependence is observed. This agreement with the electrostatic model strongly supports the claim that the observed effect is of electrostatic nature. However, for smaller dipole densities, the shift of E_{pot} is nearly constant, because the distance from the investigated C atoms to the next-nearest dipole is already so big that the local potential of the nearest dipole dominates.

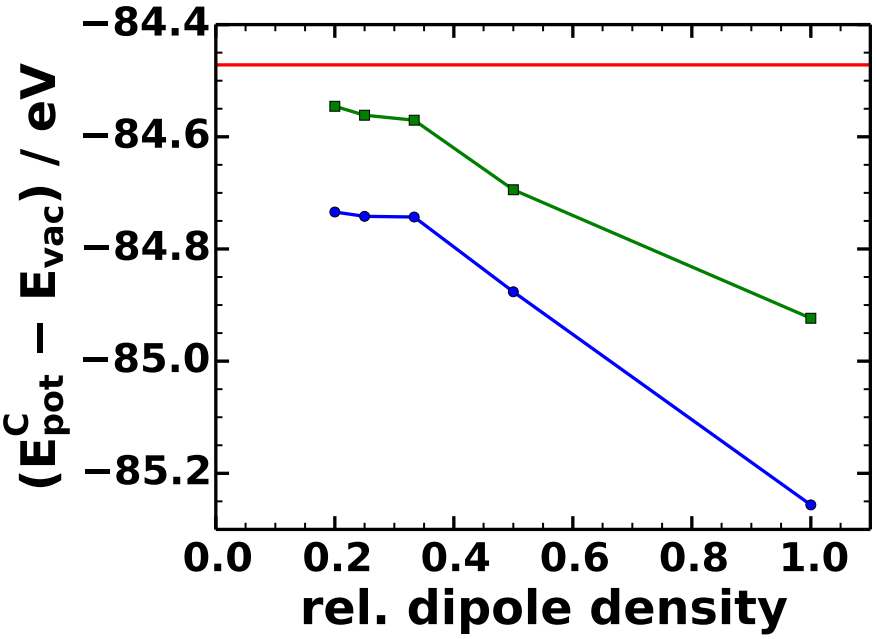

Figure 4.4.: Electron potential energy at the positions of the third (blue) and seventh (green) C atom in a BN-14C-NB-14C system (atom numbers as in figure 4.1). By enlarging the unit cell in y-direction, lower dipole densities are possible. This dipole density, in units of the full dipole density, is plotted along the abscissa. The electron potential energy of a C atom in pure graphene is indicated by the red line.

4.3. Energetic Shift of the DOS

In the previous section, the effect of lines of BN pairs on the electron potential energy in graphene was investigated. A change in E_{pot} changes the energy of all the electronic states as a function of position. This can also be seen in the density of states as a shift of the energy.

4.3.1. Shift of the Different Atom Types

The investigated systems have no net dipole moment in the unit cell (as discussed), so the total DOS, at least for a symmetric system, will not show this energy shift[1]. However it is possible to project the DOS onto certain atoms. By averaging over the projected DOS (PDOS) of several atoms, for examples all C atoms in the strip between the dipoles, the shift of the states in that spatial region can be described.

Figure 4.5 shows this averaged PDOS. In between the BN and NB pairs, the carbon states are shifted towards lower energies with respect to unmodified graphene. The carbon atoms in between the NB and BN pairs, on the other hand, have a shift to higher energies. Due to the averaging process, the features are broadened. Furthermore, the PDOS does not go to zero at the Fermi level (in contrast to pure graphene). The modifiers (i. e. the B and N atoms) also contribute states around the Fermi level: For the N atoms, the PDOS around the Fermi level is comparable to that of the adjacent C atoms. In comparison, the B atoms contribute far more importantly to the DOS right below the Fermi level. There is no gap in these systems, so a separation of electrons and holes in two different spatial regions is not possible.

[1] Nevertheless, the total DOS will be distorted compared to the DOS of pure graphene.

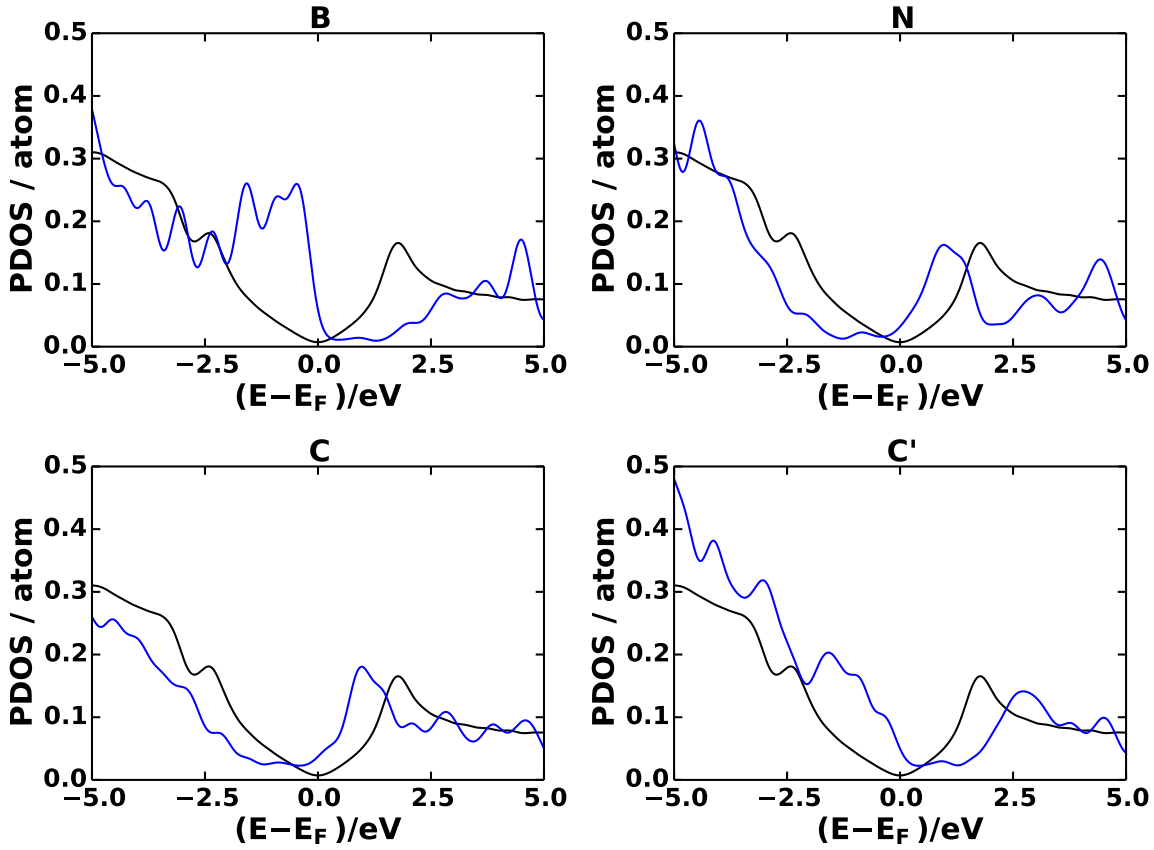

Figure 4.5.: Averaged PDOS per atom for a BN-14C-NB-14C system for the different atom types (blue line). The carbon atoms in the strip between the BN and NB lines are marked with C, the carbon atoms between the NB and BN lines as C'. To compare, the DOS per atom of pure graphene is plotted as well (black line).

4.3.2. Width Dependence

Since the screened dipole potential in graphene drops on a length scale of 6.75 Å, the atoms further away from the lines of BN pairs feel less change of E_{pot}. Thus, the shift of the averaged PDOS decreases with the strip width.

This behavior is illustrated by figure 4.6, which shows that even for a 38 atom strip the shift is still $> 0.2\,\text{eV}$.

Naturally, due to the averaging process information is lost. Still, the PDOS of the individual atoms can be investigated by itself. While the averaged PDOS is well suited to get a general impression of the effects due to the dipole lines (on a larger length scale), additional insight can be gained by separately examining the individual atoms.

In figure 4.7, the PDOS of the six carbon atoms closest to the line of BN pairs is plotted. The first atom shows a PDOS very different from the pure graphene DOS because its chemical environment is totally different – one of its bonds is with a nitrogen atom instead of a carbon atom. From the second atom on the PDOS can be explained as a shifted DOS of pure graphene. One thing that can be noticed is that the PDOS just below and at the Fermi level is higher for odd-numbered atoms than for even-numbered atoms (where it even goes to zero). While the partitioning scheme used for assigning a state to a certain atom is not perfect and could thus give rise to this behavior as an artefact, a more physical explanation is possible as well: The electron density per atom oscillates from higher values to lower values, because the two lattice sites in graphene are not equivalent anymore (the electron potential energy is different). Furthermore, disturbances in graphene have been shown to have a rather long range impact on the charge density [90, 91].

Secondly, the dependence of the PDOS of an atom on the overall strip width (the number of C atoms between BN and NB) has a very characteristic behavior: For the first six atoms from the BN pairs, the PDOS curves for large strip widths coincide. However, for low strip widths, there is an additional shift to lower energies. This stems from the influence of the oppositely oriented, i. e. NB, dipole line: if it is near, the potential is lowered even more because now two dipole lines shift the electron potential energy. If, however, it is far enough to play no role in the local electrostatic potential, this additonal shift does not happen.

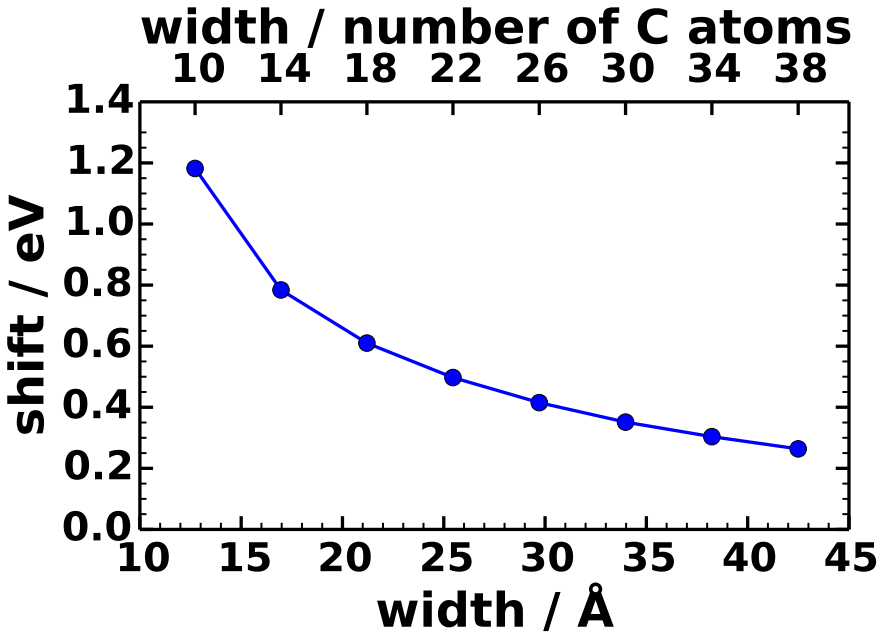

Figure 4.6.: Width dependence of the energy shift of the averaged PDOS over the atoms between the lines of BN and NB pairs in a BN-*n*C-NB-182C system. The strip width is given as the number *n* of C atoms and in Å (measured from the middle of the bond between the B and N atom). Only the absolute value of the shift, calculated as explained in section 3.7, is plotted. Here it means a shift towards lower energies.

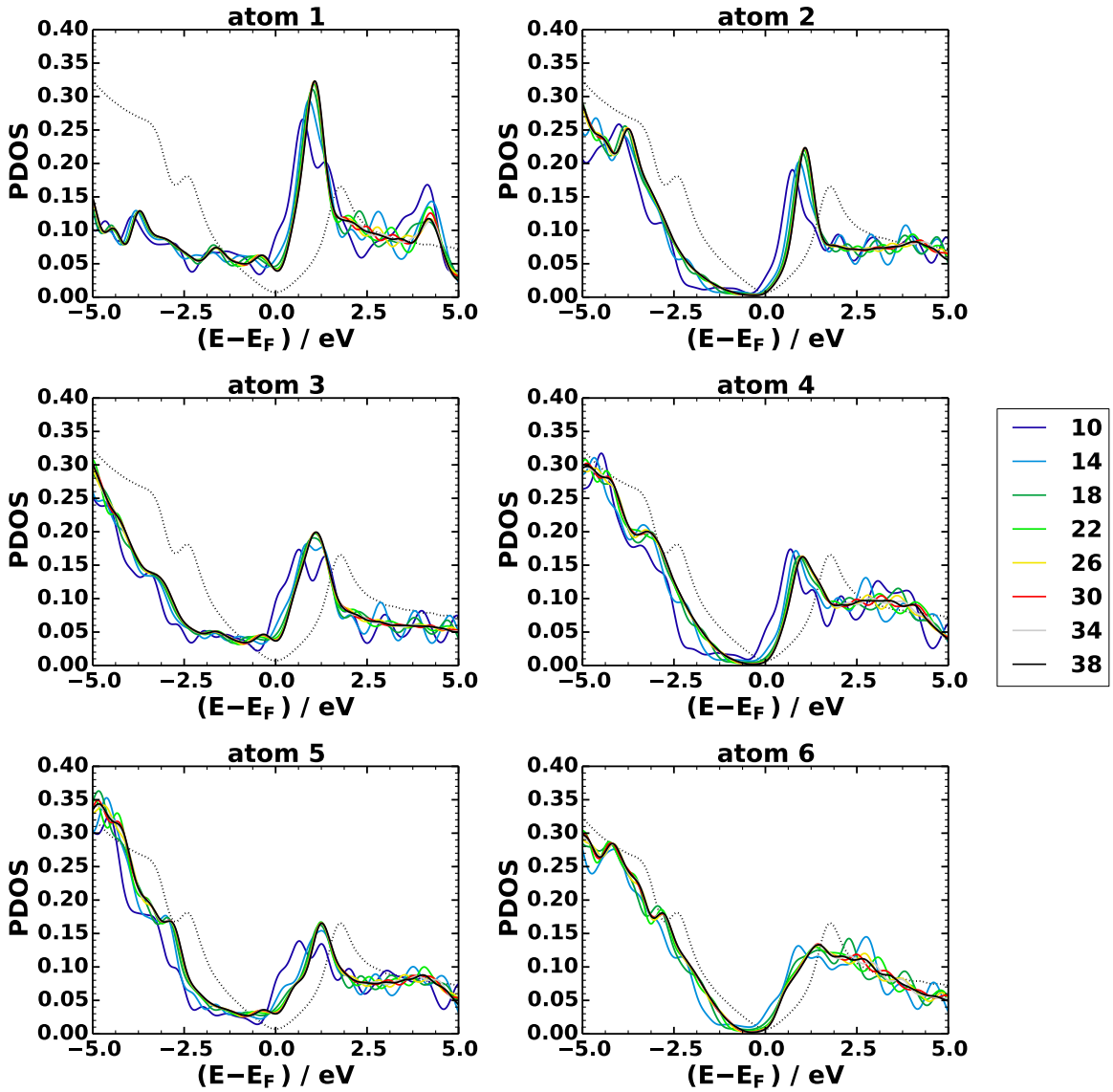

Figure 4.7.: PDOS of the individual atoms in a BN-*n*C-NB-182C system. Different strip widths *n* are used (see legend). The DOS/atom of pure graphene is plotted as a black dashed line. The numbering of the atoms is according to figure 3.1.

4.3.3. Localization of States

The spatially resolved density of states is called local DOS (LDOS). It allows to look at the distribution of the states as a function of both spatial position and energy.

The color-coded LDOS of one of the investigated systems can be found in figure 4.8a. In the shown energy window around the Fermi level, the unoccupied states are found mostly in the region between the BN and NB lines (where the electron potential energy is lowered due to the dipoles). The occupied states are located on the other side of the dipoles, i. e. between the NB and BN lines (increased E_{pot}). The relative shift (in energy) of the LDOSes in the two different strips is clearly visible. If one takes into account the BN pairs, it turns out that occupied states nearest to the Fermi level are largely localized on the BN pairs (in accordance to figure 4.5).

In figure 4.8c and d, the x-dependent LDOS is shown integrated over different energy ranges around the Fermi level. From these plots, the relative height of the charge density in the different spatial regions can be assessed. A certain degree of localization can be observed, although for this system the charge density does not go to zero even in the regions with low DOS. Therefore, the localization of charges in-between the dipole lines is not totally successful.

Around the Fermi level, the border of the regions with high LDOS and regions with low LDOS in the color-coded plot in figure 4.8 is shaped like the $E_{\text{pot}}(x)$ curves. Yet once more this demonstrates the electrostatic nature of the energy shift of the carbon states.

When one integrates the LDOS over all spatial directions, the total DOS of the system is obtained (figure 4.8b).

If one assumes that exciting electrons across the Fermi level does not change the electronic structure, electron conduction would mainly be localized in the region with lowered E_{pot}. While calculating the electronic excitations of the system or doing transport calculations is beyond the scope of this thesis, a feeling for what happens to electrons above E_F can be developed by other means: In the simplest picture, where shifting the Fermi level does not change the electronic structure, the localization behavior described here would imply that additional electrons inserted into the system would be nicely localized in the strip between the BN and NB pairs. The following considerations will investigate what happens when the calculation is done with an extra number of electrons.

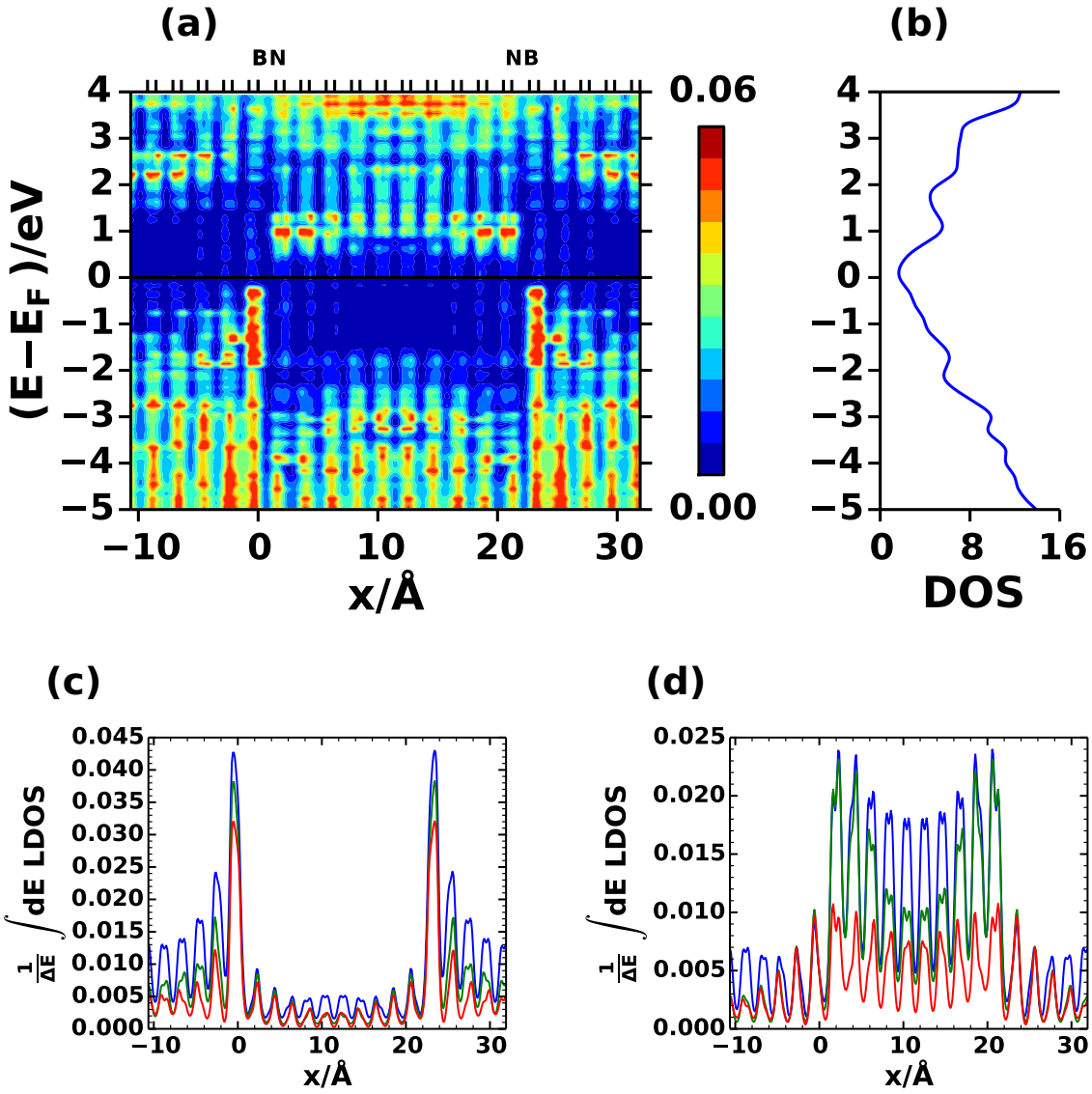

Figure 4.8.: (a) Local DOS, yz-plane integrated, depending on the x-position and the energy (color-coded), of a BN-18C-NB-18C system (geometry individually optimized with GADGET). (b) DOS of the total system as resulting from the left plot when integrating along the x-axis. (c, d) LDOS averaged over different energy ranges: (c) in the interval $(-2, 0)$ eV (blue), $(-1, 0)$ eV (green) and $(-0.5, 0)$ eV (red), (d) in the interval $(0, 2)$ eV (blue), $(0, 1)$ eV (green) and $(0, 0.5)$ eV (red).

4.3.4. Excess Number of Electrons

It is possible to do VASP calculations with more or fewer electrons per unit cell than in the neutral case[2]. Then, the program adds a homogeneous positively charged background in the whole volume of the unit cell to compensate the charge imbalance. In the context of this work it is then interesting to see where the excess charge goes. This can be calculated by substracting the neutral charge density from the charge density of the system with an elevated or reduced number of electrons.

Figure 4.9 shows that there is no nice localization of excess electrons in a certain spatial region, but that they can rather be found everywhere in the graphene sheet throughout the unit cell. In the region far from the dipoles, the excess charge density is located at the carbon-carbon bonds parallel to the x-direction. In each of the pairs of atoms forming these C-C bonds, the atom nearer to the dipole lines seems to get more of the extra electrons than the atom further away (this can be best seen in the averaged excess electron density in the lower plot in figure 4.9). This could be related to the observation that the PDOS of the oddly numbered atoms in figure 4.7 is higher around the Fermi level than the PDOS of the evenly numbered atoms. Closer to the dipole lines and especially in the graphene strip in between the BN and NB pairs, the extra electron density forms lines along the zigzag bonds of graphene. In conclusion, we see two different shapes of charge distribution, once around parallel pairs of C-atoms and once in zigzag lines. It is worth noting that these two characteristic shapes can also be found in isodensity plots of the charge density of graphene states, as will be shown in figure 4.18.

The oscillations seen in the yz-plane averaged excess charge density in figure 4.9 are a direct consequence of the localization of the surplus electrons on individual bonds. One very interesting thing that can be seen from this averaged plot is that at some points, the charge density of the system with more electrons is lower than the neutral system (the excess charge density is negative). This could not happen if extra electrons would just fill up some previously empty states without otherwise changing the system.

Note that the range of possible values of the number of excess electrons per unit cells is limited for getting sensible results: Very large values (like one electron per unit cell) are not realistic and change the Fermi level significantly. Furthermore, the compensating positive charge is quite substantial in that case, creating additional artefacts. On the other hand, too low values lead to numerical errors.

Overall, the spatial average is still 0.2 electrons per unit cell everywhere, so all in all the localization is not successful. The following theoretical model tries to explain why.

[2] This can be done by manually setting *NELECT* in the `INCAR` file to a value higher or lower than the default value, which is chosen so that there is charge neutrality. Non-integer values are possible.

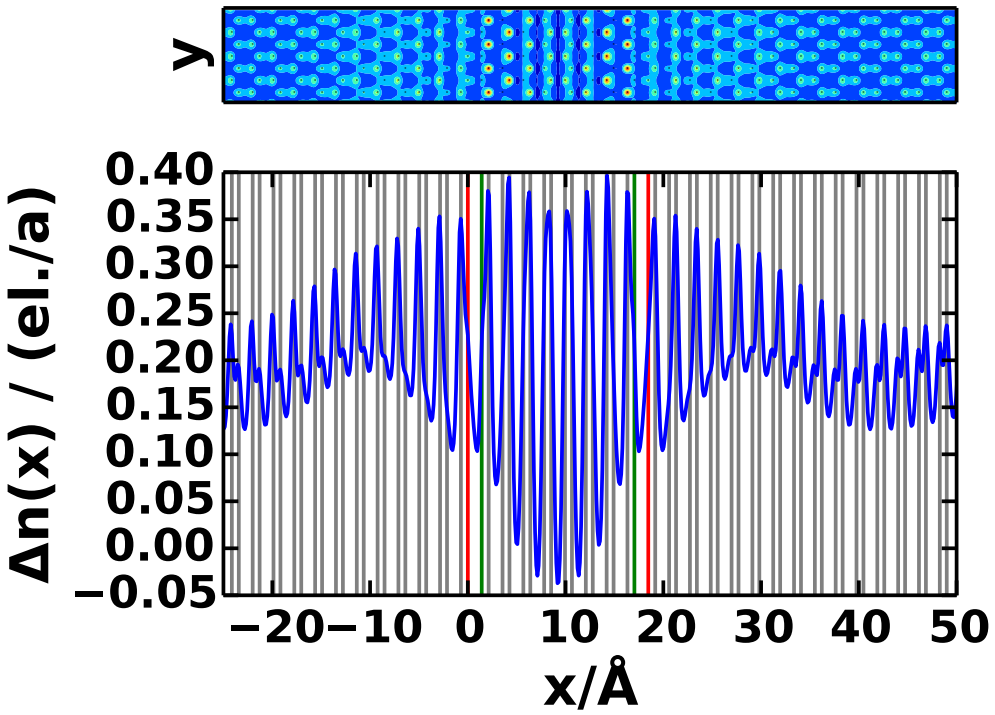

Figure 4.9.: Spatial distribution of the excess electron density for a BN-14C-NB-182C system (in contrast to the other calculations, here a non-optimized pure graphene-like geometry was used). In total, 0.2 electrons per unit cell have been added to the number of electrons per unit cell of a neutral system. The upper plot shows the two-dimensional graphene sheet, colored according to the value of the excess electron density Δn. Blue means low values, red high values. The lower plot shows (in blue) the yz-plane-averaged value of the excess charge density as a function of x, in units of electrons per unit cell. The gray lines mark the position of the carbon atoms, the red lines the position of the boron atoms and the green lines the position of the nitrogen atoms.

4.3.5. Shifted PDOS Model

When dealing with the question how and whether localization of (excess) electrons and holes is possible, there is a fundamental difference between semimetals and semiconductors. To investigate this further, a very simple model is chosen. A linear chain of $N = 20$ atoms is taken as a test system. Each of the atoms gets assigned a value for the electron potential energy E_{pot} (see figure 4.10). As demonstrated above, a shift in the electron potential energy leads to a shift of the DOS projected onto this atom. Therefore, in this toy model, the shape of the PDOS at each atom is chosen to be identical, but the PDOS curves of the individual atoms are shifted in energy according to their value of E_{pot}.

For the DOS shapes, two different models are investigated (see figure 4.11).

1. **Graphene-like model**:
   The PDOS of each atom is[3]
   $$\text{PDOS}(E) = |E|. \tag{4.1}$$

2. **Semiconductor model**:
   The PDOS of each atom consists of a step function:
   $$\text{PDOS}(E) = \begin{cases} 0 & |E| < 2.5 \\ 1 & |E| > 2.5 \end{cases}. \tag{4.2}$$

In figure 4.12, the resulting PDOSes after applying the E_{pot} shift are shown for the unshifted atoms, the maximally down-shifted atom and the maximally up-shifted atom. By summing over the PDOSes of all the atoms, the total DOS is obtained, see figure 4.13. In the graphene-like model, the DOS does not go to zero at the Fermi level because one of the shifted atoms always provides states at E_F. In the semiconductor model, there remains a gap, although it becomes far narrower. The steps in the DOS come from the discrete values for the shifts.

Now a certain number of excess electrons N_{extra} is brought into the system. This causes the Fermi level to shift (to higher energies for positive N_{extra}, to lower energies for negative N_{extra}). The new Fermi level is the energy $\tilde{E}$ that fulfills the equation

$$\int_{E_F}^{\tilde{E}} dE\ \text{DOS}(E) = N_{\text{extra}}. \tag{4.3}$$

Here, the old Fermi level is E_F and by DOS(E), the total DOS is meant.

Next the PDOSes of the individual atoms are filled up to that new Fermi level. Then, for each atom the resulting added electron density is plotted (see figure 4.14). In other words, in this plot it can be seen where the additional charge density goes.

[3] For this simple model, we do not worry about the units. For real graphene, the slope of the DOS would be $D_0 = 0.09\,(\text{eV}^2 \text{ unit cell})^{-1}$, i.e. $D(E) = D_0|E|$, see Ref. [92].

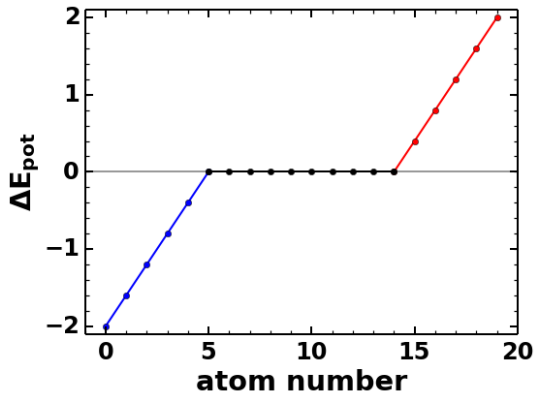

Figure 4.10.: Shift of the electron potential energy E_{pot} and thus the PDOS with respect to E_F for atoms at different positions along the chain. The region with a negative shift is plotted in blue, the region with a positive shift in red. In this simple model, no units are used.

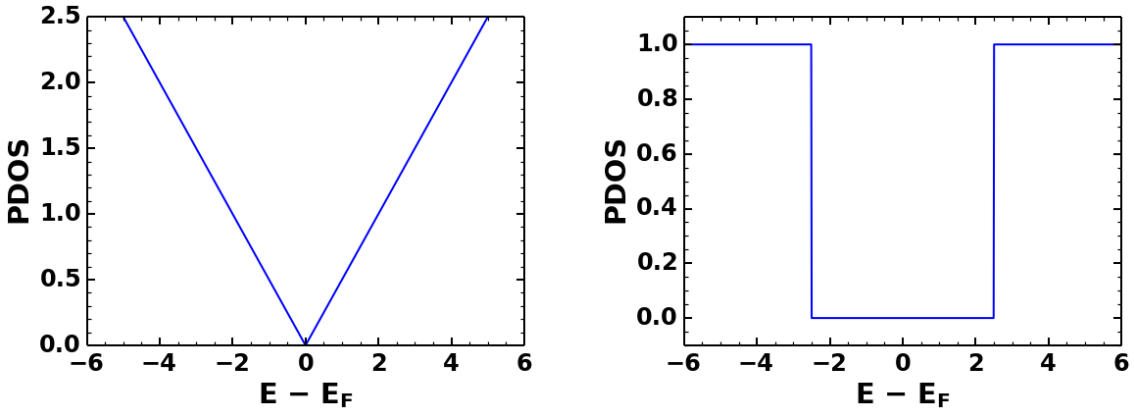

Figure 4.11.: Left: PDOS for the graphene-like model. Right: PDOS for the semiconductor model.

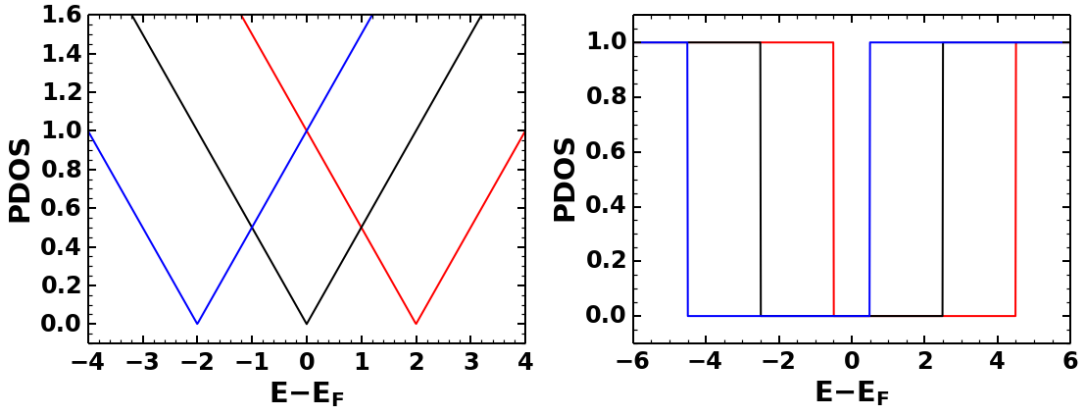

Figure 4.12.: PDOS of the unshifted atoms (black) and the atoms with the maximum shift towards lower (blue) and higher (red) energies. This is shown for the graphene-like model (left) and the semiconductor-like model (right).

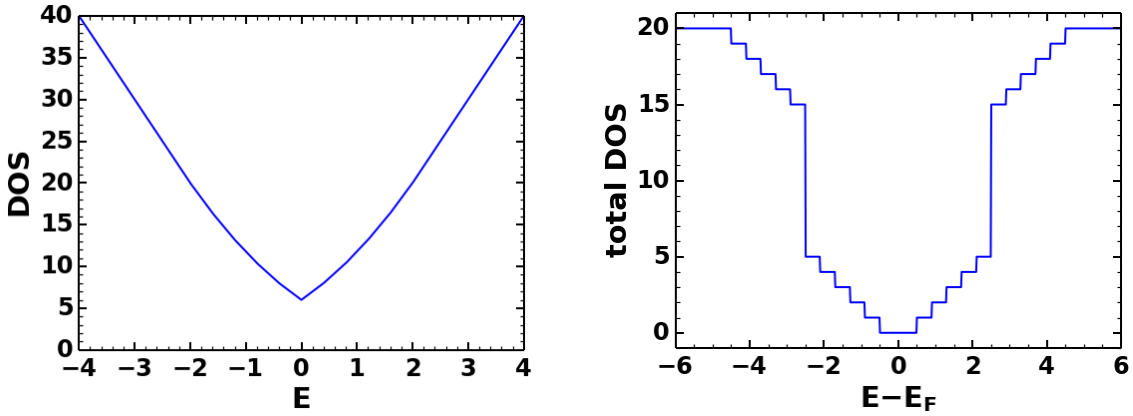

Figure 4.13.: Total DOS for the graphene-like model (left) and the semiconductor model (right).

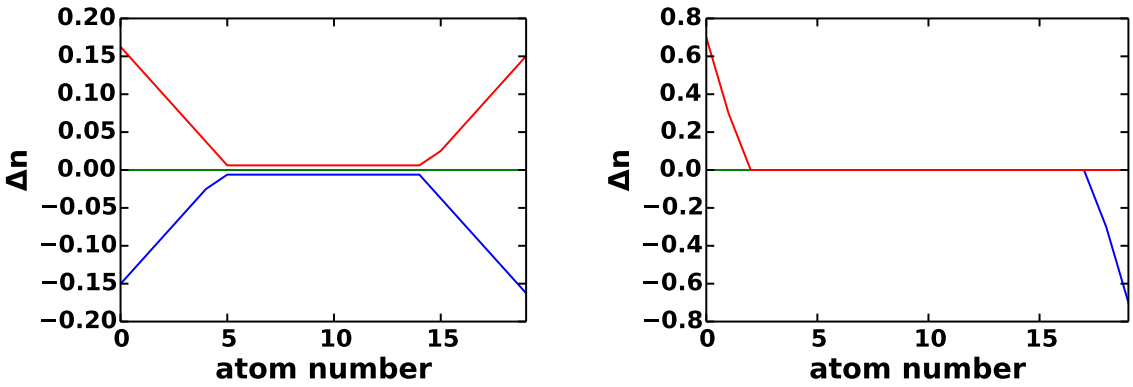

Figure 4.14.: Excess electron density Δn per atom when the total excess electron density is $N_{\text{extra}} = +1$ (red) and -1 (blue). The left plot is for the graphene-like model, the right plot for the semiconductor-like model.

For a *semimetal*, both electrons (positive N_{extra}) and holes (negative N_{extra}) can be found in spatial regions with elevated or reduced electron potential energy (irrespective of the sign of the shift of E_{pot}). This is because the upward-shifted and the downward-shifted PDOSes both have high values at the old Fermi level (see figure 4.12). More mathematically speaking, the integral from the old Fermi level to slightly higher or lower values does not differ much between these two cases. So it is not possible to localize electrons and holes in different spatial regions with this approach (this is in accordance with the quantum-mechanical results in figure 4.9). However, hardly any excess charge goes to the unshifted atoms, because here the PDOS around the old Fermi level is very low. So a localization of excess charge in regions that have a shift (either positive or negative) seems possible (although it does not seem to be that way in figure 4.9, probably because of changes of the DOS beyond a simple electrostatic shift). In stark contrast, for *semiconductors*, electrons only go to regions with lower potential energy and holes are only found in regions with increased E_{pot}. This is because the new valence band comes from down-shifted states and the new conduction band

So, there a localization of electrons and holes in different spatial regions, and thus their spatial separation, is achieveable.

The Python programs used to calculate the results in this section can be found in appendix C.

4.4. Energetic Shift of the Band Structure

The energetic shift of the states on different sides of the dipole lines also leads to changes in the band structure.

Figure 4.15 shows the band structure in the high symmetry directions of the rectangular

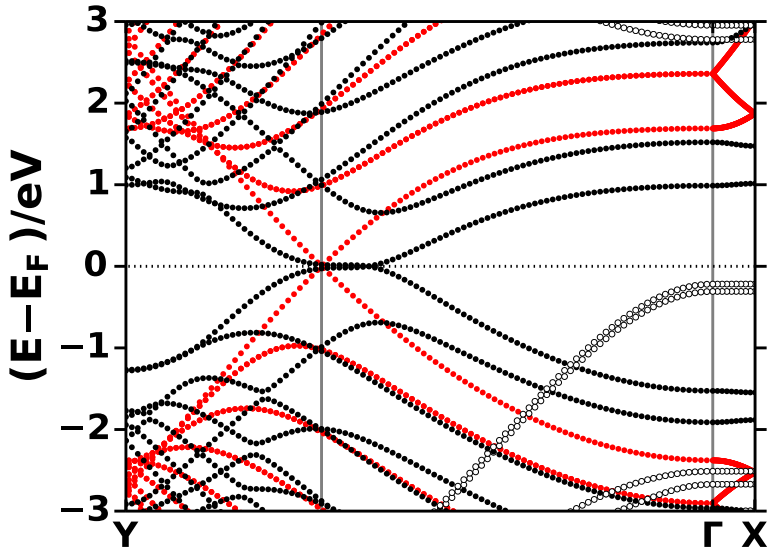

Figure 4.15.: Kohn-Sham band structure of a BN-14C-NB-14C system (black symbols) and of pure graphene in an equivalent (8×1 rectangular) unit cell (red symbols). Open symbols mark bands with predominantly σ character, filled symbols bands with π character. Due to Brillouin zone folding, the K point of the hexagonal system is found at 2/3 of the way from Γ to Y (this is shown by the gray vertical line).

unit cell of a BN-14C-NB-14C system. In the Y-direction, this is the direction along the dipole lines, states are found around the Fermi level. However, the linear dispersion that is characteristic for the Dirac cone is not present around the Fermi level anymore. The bands are flattened and show a rather parabolic dispersion (like e. g. bilayer graphene [93]). At around ±1 eV above the Fermi level, there is a band crossing with linear dispersion at the K point, which is due to the intersection of two back-folded π bands. In the X-direction, there is hardly any dispersion.

This band structure cannot be compared with the band structure of graphene in a hexagonal unit cell, but rather with a pure graphene system in the same rectangular supercell (red symbols in figure 4.15). Therefore, the graphene band structure used for comparison was calculated using a 8×1 rectangular supercell (this is equivalent to the BN-14C-NB-14C system). While some of the bands in the BN-substituted system can clearly be identified with one of the graphene bands, there are other bands whose origin is not so obvious.

From figure 4.15 it can also be seen that most of the bands of the BN-substituted system have π character (filled symbols). This indicates that they originate from the bands involved in the Dirac cone (in the energy range around the Fermi level). There is only one set of σ bands (open symbols) close to the Fermi level.

For very wide strips, the band structure is expected to be very graphene like. Therefore, the

band structure calculation was performed using different strip widths from BN-14C-NB-14C to BN-30C-NB-30C (see figure 4.16). Indeed, for very broad strips, the bands around the Fermi level lie closer to the Dirac cone than for narrow strips. That happens because there are now many undisturbed carbon atoms in the system. When the strip width changes, the shift of the individual bands with respect to the Fermi level changes, but whether the energy shift grows or diminishes is different from band to band. The σ band close to the Fermi level hardly shifts at all.

The next thing to investigate is where the individual states in the band structure are localized. Chapter 3.8 explains how this can be done. The resulting band structures are displayed in figure 4.17. There is a general trend that occupied states near the Fermi level sit between the NB and BN pairs (this is the region with increased E_{pot}) while the unoccupied states are located between the BN and NB lines (lowered E_{pot}). The σ band closest to the Fermi level sits at the BN lines. This is why it also does not change much in energy when the strip width is changed because the dipole itself shows the least sensibility to how much carbon lies on the way to the next dipole line. Whether increasing the strip width shifts the band to lower or higher energies is also not linked to localization.

The bands directly at the Fermi level change their localization when they go from occupied to unoccupied. In many bands, the localization behavior in the region between Γ and K[4] differs from the localization behavior between K and Y. This is because these are two different regions in the original hexagonal unit cell (see figure 2.14).

In figure 4.18, isodensity plots of the LDOS for selected k-points and bands are shown. The points labeled 1 and 2, very close to the Fermi level, show the localization of the occupied and unoccupied states in different spatial regions. Another difference can be seen: at point 1, the isodensity surface forms “tubes” along the zigzag lines of graphene. In contrast, at point 2 one can identify individual isosurfaces sitting on the parallel bonds. At point 3, where the two bands cross, the bands mix and localization is lost. At point 4, a “tube” pattern similar to that at point 1 is observed (which probably means that they originate from the same pure graphene state). However, the state at point 4 is located on the opposite side of the dipole line, as expected for an occupied state. For points 2 and 5, the analogous argument is valid: they have a similar orbital shape, but are located in different regions. The next highest band in energy contains points 6 and 7. Again, when crossing the K point, the localization character of the band changes significantly. This band crosses another band very close to the K point. On that band, there are the points 8 and 9. At point 8, a nice localization of the state is observed, while this breaks down when going to smaller values of k, as can be seen at point 9. Similar observations can be made for the occupied bands that cross at 1 eV below the Fermi level (points 10 and 11). The σ-Band that point 12 belongs to is mainly localized at the boron atom, in accordance with the results from the calculations in figure 4.17.

[4]The K point of the hexagonal graphene system is found at 2/3 of the way from Γ to Y in the rectangular system, as discussed in chapter 2.4.4.

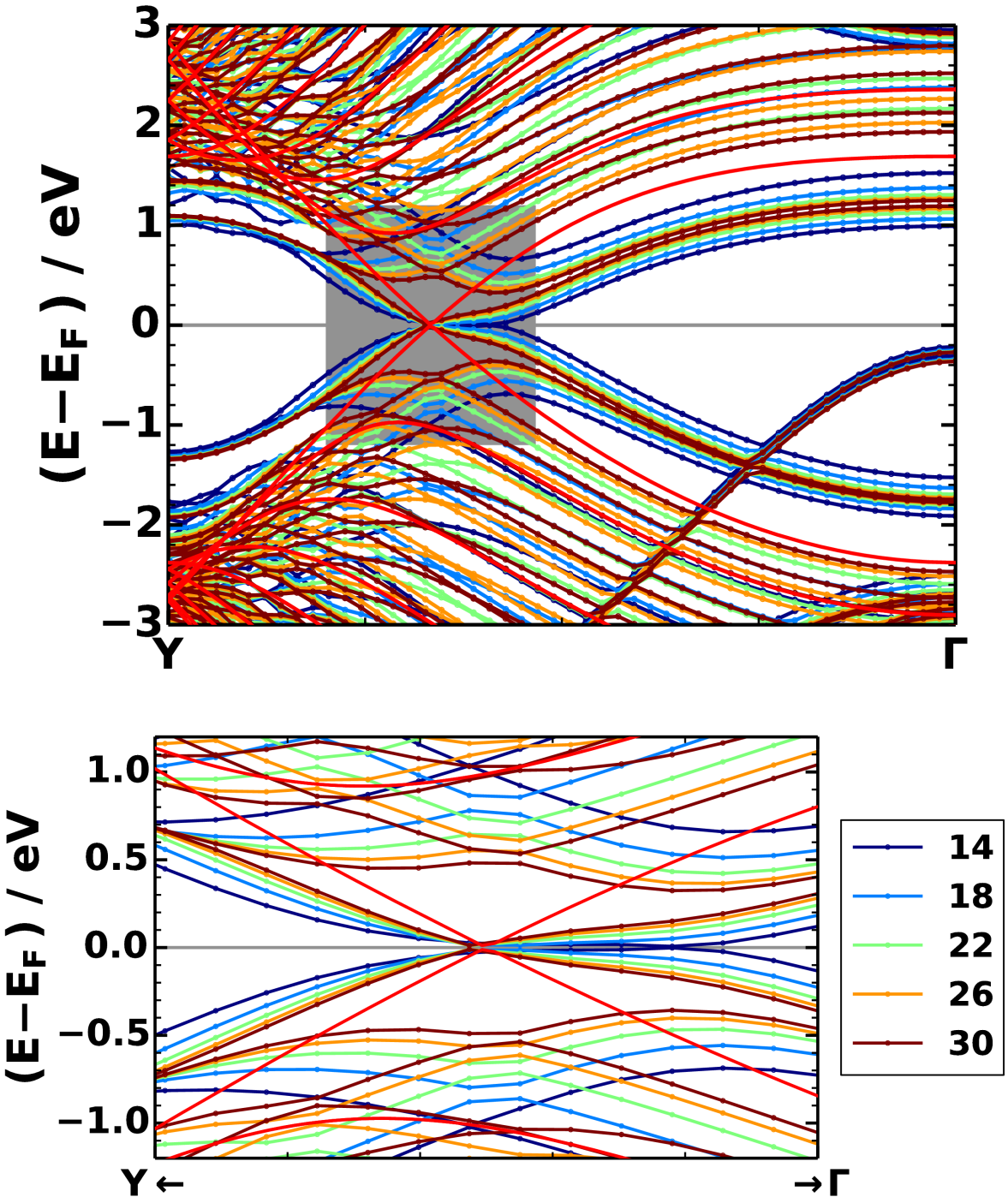

Figure 4.16.: Top: Kohn-Sham band structure from Γ to Y of BN-*n*C-NB-*n*C systems for different values of n (see legend). In comparison, the band structure of pure graphene in a 8×1 rectangular unit cell (equivalent to the unit cell for $n = 14$) is shown (red line). The Dirac cone in pure graphene is found at 2/3 of the way from Γ to Y. With decreasing strip width, the bands around the Fermi level become more and more flattened. Bottom: Zoomed in on the region that is marked by a gray rectangle in the top plot.

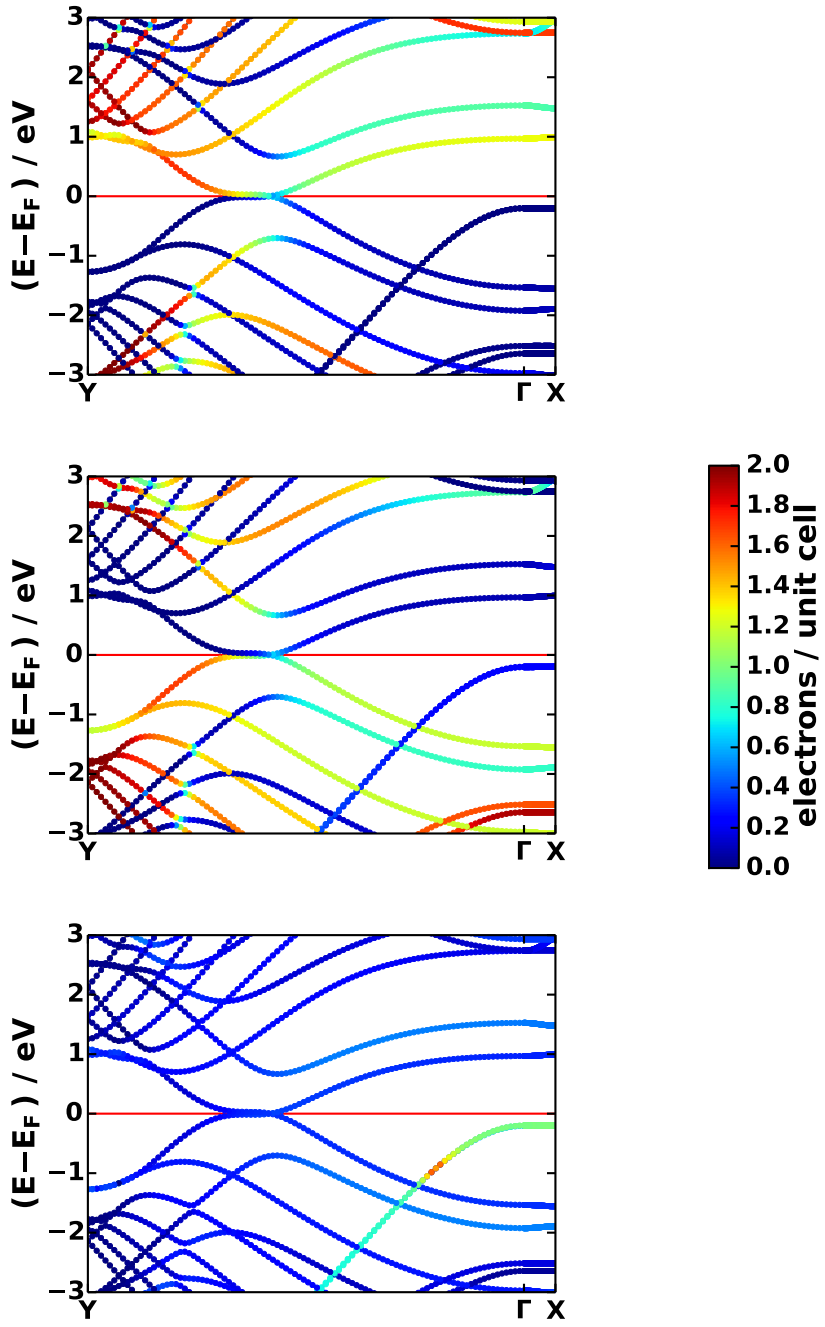

Figure 4.17.: Kohn-Sham band structure of a BN-14C-NB-14C system (geometry individually optimized with GADGET). The k-point resolved band-projected LDOS (see chapter 3.8) is calculated for each point in the band structure and then integrated over three different areas: between the BN and NB pairs (top), between the NB and BN pairs (middle) and at the BN pairs (bottom). The value of the integral is color-coded in the plot.

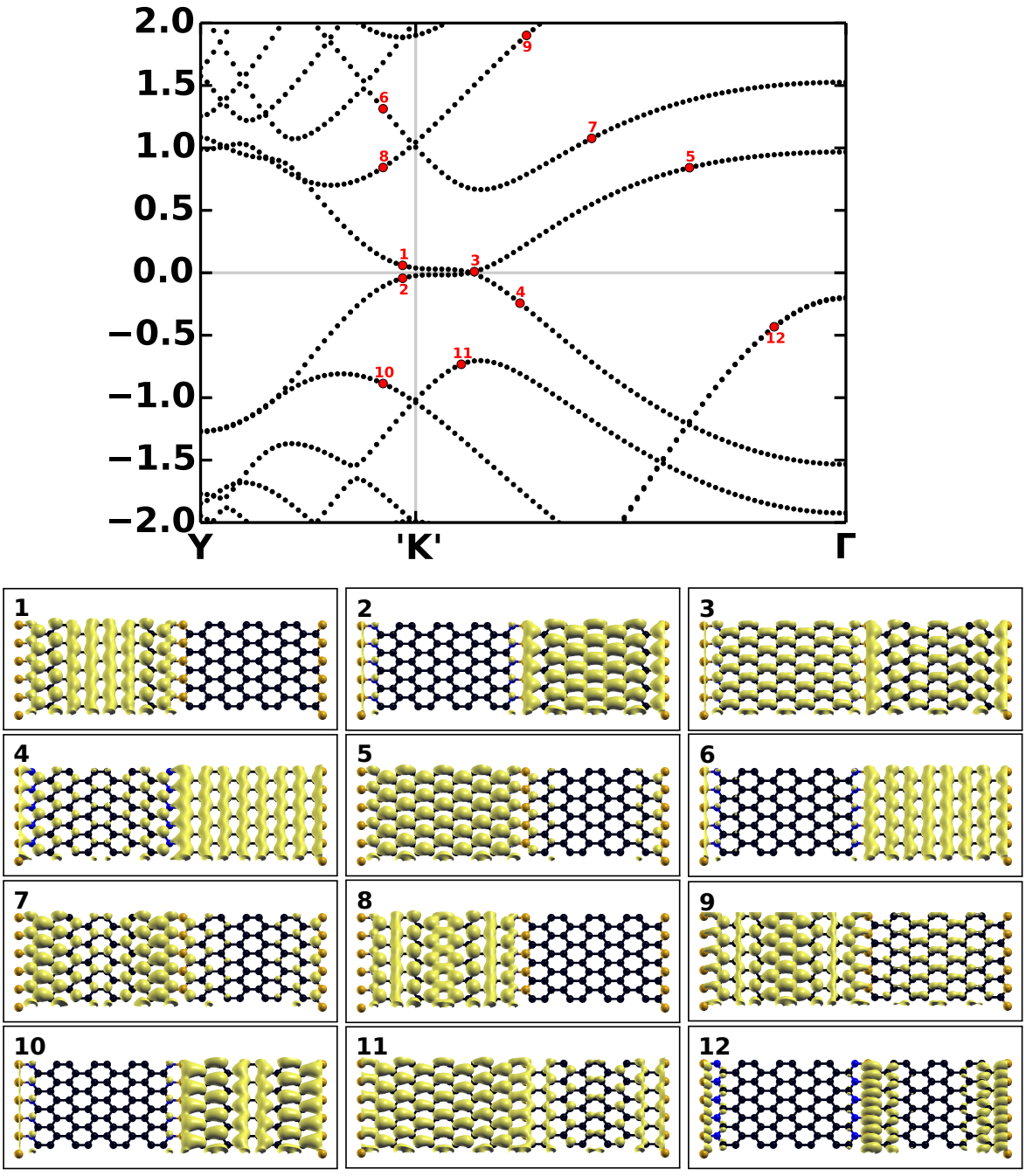

Figure 4.18.: Isosurface of the band-projected k-resolved LDOS at different points in the band structure (see plot at top) of a BN-14C-NB-14C system. The isovalue is 0.01 el./unit cell.

4.5. Other Geometries

In this section, different ways of substituting two neighboring C atoms to create BN pairs are investigated. Apart from the systems with parallelly oriented dipoles discussed so far, there are two general options. These are armchair-like (AC) and zigzag-like (ZZ), see figure 4.19. For the present tests unoptimized structures with all the bond lengths equal to 1.42 Å were used.

4.5.1. Zigzag

In the ZZ case, the dipole density is lowered to 50 % compared to the systems investigated so far: the number of dipoles per unit cell is the same, but they point at a 60° angle from the x-axis. The y-components of the dipoles compensate each other, so only the x-component remains, which is the total dipole moment multiplied by $\cos 60° = 0.5$. Of course, the depolarization behavior is expected to be different, so these 50 % are just a rough approximation.

The width dependence of the energy shift of the PDOS averaged over the C atoms between the BN and NB pairs in ZZ BN-nC-NB-bC systems, with $b = 196 - n$, is investigated in figure 4.20. For rather narrow strip widths, the shift of the averaged PDOS does not follow the same pattern as in the geometry with the BN pairs parallel to each other, because the big differences in the chemical environment of the C atoms closest to the N atoms play a dominating role there. For wider strips, the shift of the ZZ system turns out to be 67 % of the shift of the parallel-BN system. This is substantially more than the 50 % expected from the naive dipole density picture, but due to the very different chemical environment of the B and N atoms (bound to only one C atom as opposed to two) and presumably a different depolarization behavior, this seeming mismatch can be explained.

From the PDOSes in figure 4.21, one can, once more, see that there is chemically a big difference between the B and N atoms in these two systems. The C atoms between the BN and NB lines are shifted to lower energies again, but less, as already discussed above. Due to the large strip width between the NB and BN lines, there is hardly any deviation from the pure graphene DOS there.

As the E_{pot} shift is lower than for the geometries with parallel dipoles, no further investigation of the ZZ structures have been performed.

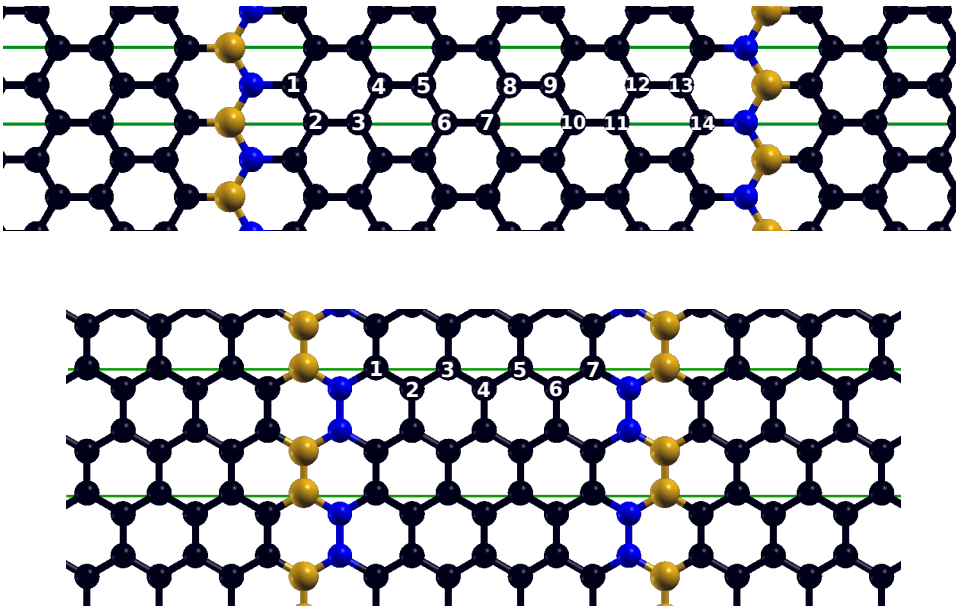

Figure 4.19.: Geometry of a ZZ BN-14C-NB-bC strip (top) and an AC BN-7C-NB-bC strip (bottom). Different numbers of C atoms between the modifiers are possible. The horizontal green lines indicate the boundaries of the unit cell in the y-direction. Graphics produced with XCrysDen [94].

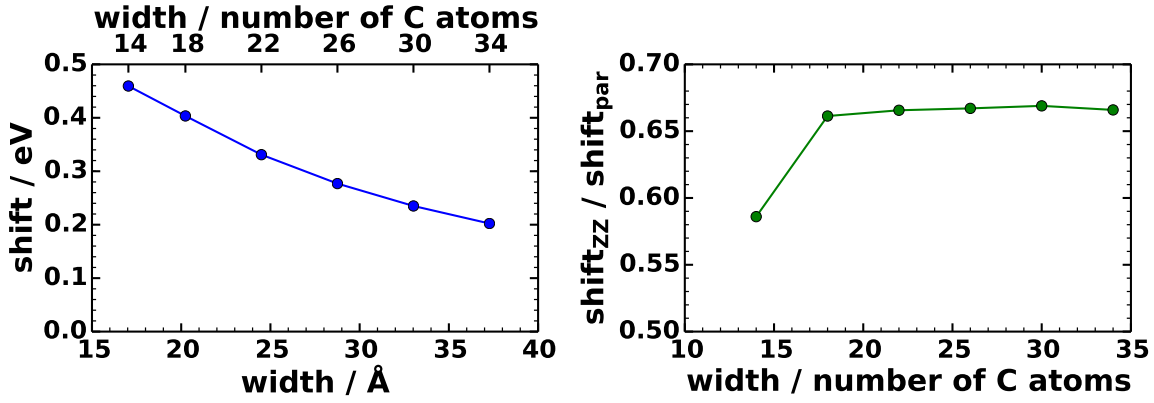

Figure 4.20.: Left: Width dependence of the energy shift of the averaged PDOS over the atoms between the lines of zigzag BN and NB pairs in a ZZ BN-nC-NB-$(196-n)$C system in analogy to figure 4.6. The strip width is given as the number n of C atoms. Only the absolute value of the shift, calculated as explained in section 3.7, is plotted, here it means a shift towards lower energies. Right: Value of the PDOS shift for the zigzag systems investigated here (values from the plot on the left) divided by the values for the BN-nC-NB-182C geometry (data values from figure 4.6, i. e. the system with parallel BN pairs).

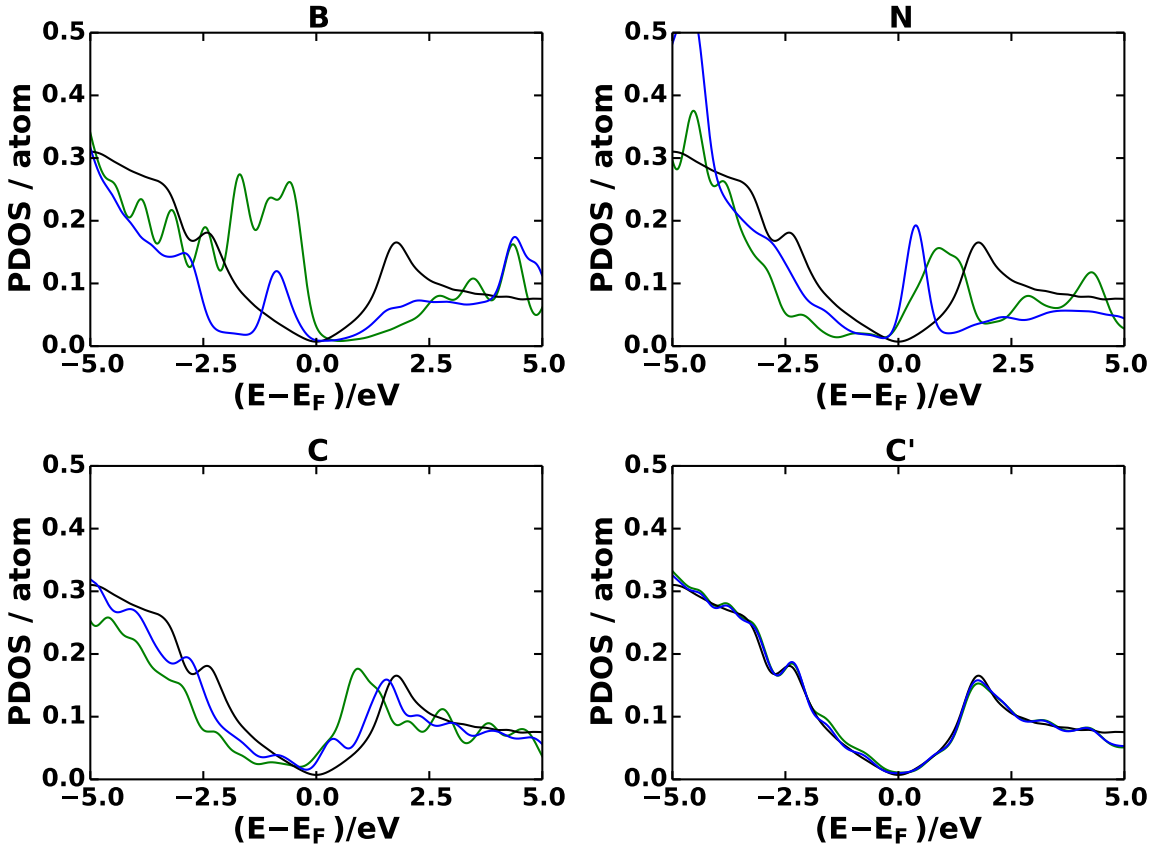

Figure 4.21.: Averaged PDOS per atom for a ZZ BN-14C-NB-182C system for the different atom types (blue line). The carbon atoms in the strip between the BN and NB lines are marked with C, the carbon atoms between the NB and BN lines as C'. To compare, the DOS per atom of pure graphene (black line) and the corresponding curves for a BN-14C-NB-182C system with parallel BN pairs (green) is plotted as well. This plot is to be understood in analogy to figure 4.5.

4.5.2. Armchair

In the AC case, there are 2 dipoles per unit cell, but the unit cell is bigger in y-direction by a factor of $\sqrt{3}$ compared to the systems with parallel BN pairs. This gives a dipole density that is increased by $2/\sqrt{3}$, but the dipoles point in a 30° angle, which reduces the dipole moment in x-direction by $\cos 30° = \sqrt{3}/2$, i. e. the dipole density is 100 %.

As before, there is an energy shift of the states of the C atoms due to the dipole lines, which leads to a PDOS shifted with respect to pure graphene. However, the width dependence of the PDOS shift (figure 4.22) is far more difficult to interpret in this case. As figure 4.23 shows, AC BN-nC-NB-bC strips can behave differently depending on their width: for a number of C atoms $n = 3k$ and $n = 3k + 2$ (figure 4.23a and c), the behavior is similar. However, for $n = 3k + 1$ (figure 4.23b), the shape of the averaged PDOS of the C atoms between the BN and NB pairs around E_F is very different from the other cases. This is also the reason why the energy shift of the PDOS (figure 4.22) seems to have a jump at these strip widths. The observation of three distinct behaviors of the width dependence of a quantity is also seen in armchair graphene nanoribbons (see 2.4.3) [38, 39].

In the band structure of AC strips (figure 4.24), one can see that, depending on the width, they are semiconducting or semimetallic (at least in the DFT calculations used). The gap in the $n = 3k + 1$ case is very small (on the order of magnitude of 0.05 eV), that's why it cannot be seen in the smeared PDOS plots ($SIGMA = 0.3$ eV). However, this band gap is too small to be of relevance for the scope of this work.

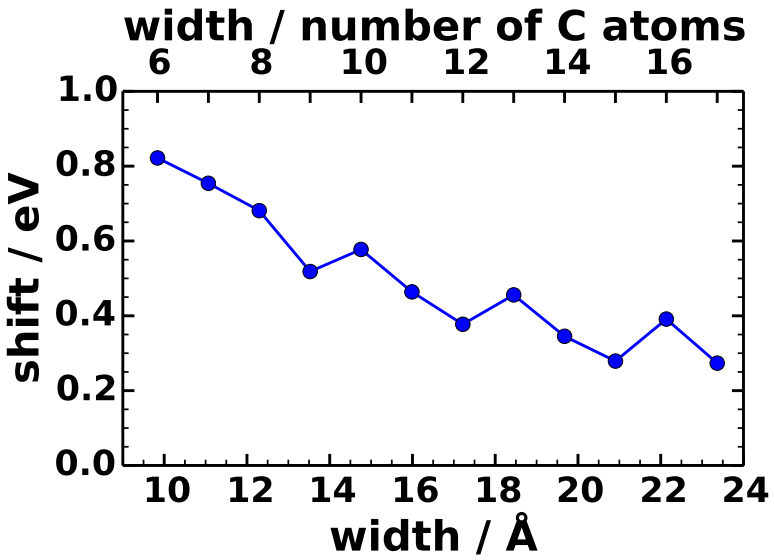

Figure 4.22.: Width dependence of the energy shift of the averaged PDOS over the atoms between the lines of armchair BN and NB pairs in an AC BN-nC-NB-$(96-n)$C system in analogy to figure 4.6. The strip width is given as the number n of C atoms as counted in figure 4.19. Only the absolute value of the shift, calculated as explained in section 3.7, is plotted, here it means a shift towards lower energies.

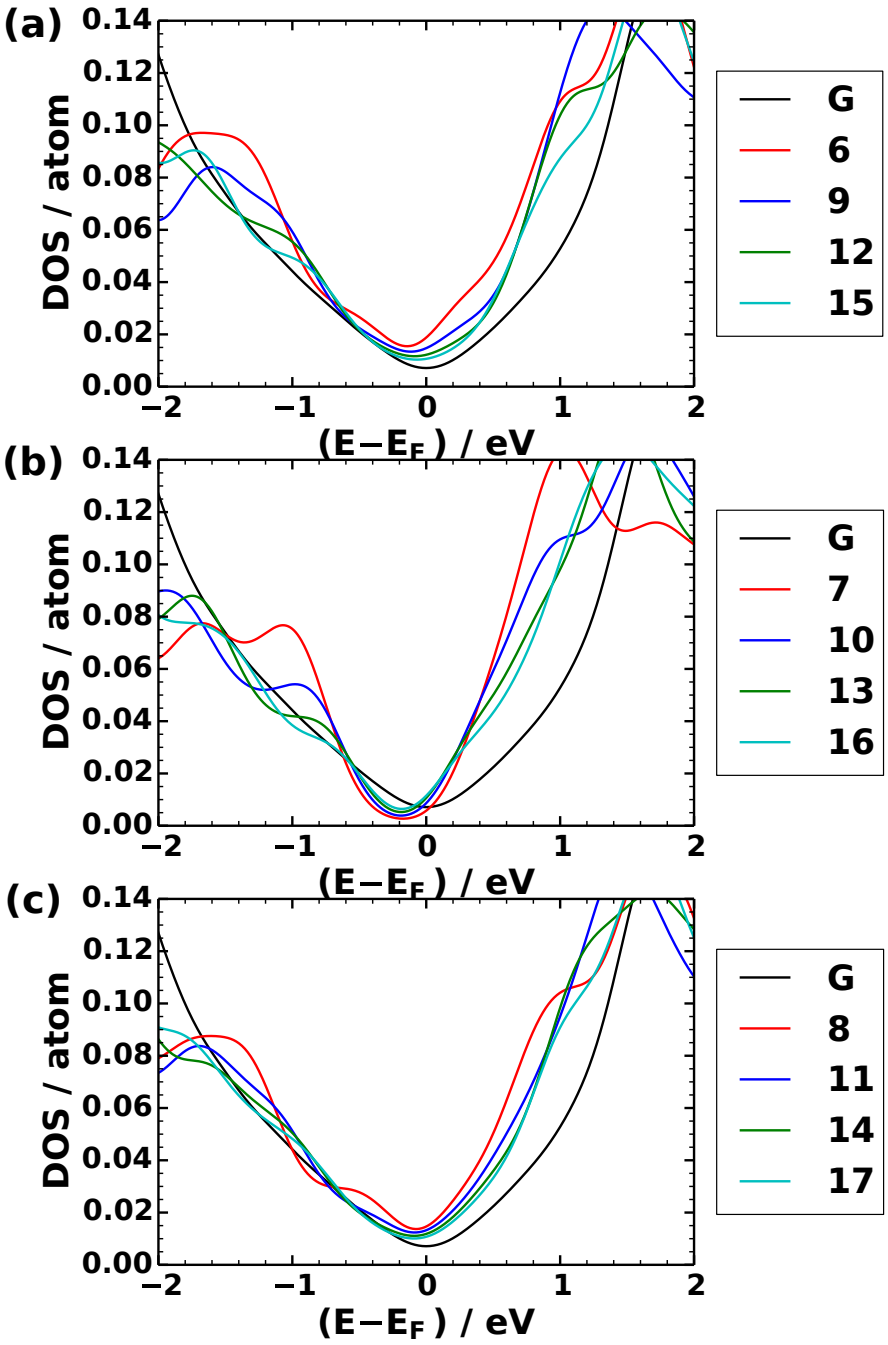

Figure 4.23.: PDOS of the C atoms between the BN and NB pairs of AC BN-nC-NB-$(96-n)$C systems with different values of n. The strip width is given as the number n of C atoms (see legend) as counted in figure 4.19. For comparison, the DOS per atom of pure graphene (G) is plotted as well. The shape of the PDOS depends on the strip width, where widths (a) $n = 3k$, (b) $3k+1$ and (c) $3k+2$ behave differently.

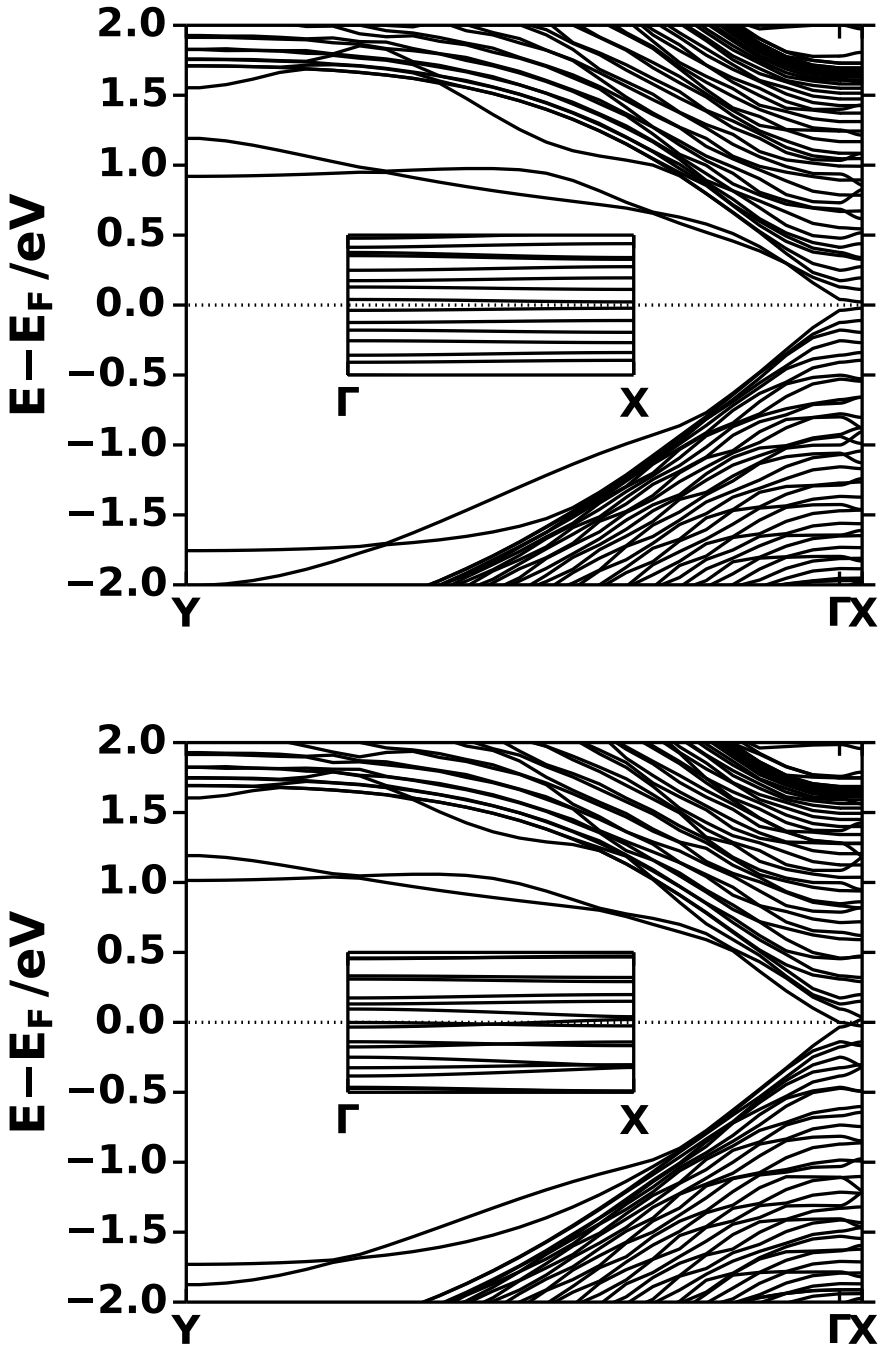

Figure 4.24.: Kohn-Sham band structure of an AC BN-7C-NB-89C, i. e. $n = 3k + 1$, system (top) and of an AC BN-9C-NB-87C, i. e. $n = 3k$, system (bottom). In the insets, the band structure from Γ to X is plotted on a bigger scale (with the same energy scale). Note that, as the AC unit cell is rotated by 90° with respect to the other rectangular unit cells examined so far, the K point from the hexagonal Brillouin zone is now found in the X-direction.

5. Graphene with Adsorbed Molecules

While the graphene systems with in-plane dipoles by substitutional BN pairs show the concept of collective electrostatic effects in two-dimensional materials quite nicely, it is probably hard to build them in experiments. A far more realistic scenario is using organic molecules with dipolar end groups to form dipole lines. The ordered arrangement of the molecules can in principle be achieved using self-assembly with appropriate linker groups. [95] As a proof of principle, here the consequences of letting molecules adsorbe in ordered manner on graphene are investigated. However, the linker groups and the assembly process are not simulated.

5.1. Investigated Systems

The common building block of all the molecules investigated here is diphenylacetylene (see figure 5.1a), which is also the basis for the so-called "Tour wire" (TW) molecules [96] which play a big role in molecular electronics. That is why in this work all the molecules derived from it are abbreviated with TW.

The chemical structures of the molecules that will be investigated in this chapter are displayed in figure 5.1. They are called the TW-CN, TW-Pyr N_{out} and TW-Pyr N_{in} molecules[1]. These molecules were put onto a graphene layer and the adsorption geometry was relaxed (as described in chapter 3.2). The adsorption height (averaged over all carbon atoms in the backbone) of these three molecules can be found in table 5.1.

[1] A very short comparison of these molecules with other molecules is found in chapter 6.4.

Table 5.1.: Adsorption height of the individual molecules regularly adsorbed on a sheet of graphene: maximum (h_{max}), minimum (h_{min}) and average ($\bar{h}$).

Molecule	h_{max}/Å	h_{min}/Å	$\bar{h}$/Å
TW-CN	3.358	3.338	3.344
TW-Pyr N_{out}	3.403	3.352	3.374
TW-Pyr N_{in}	3.421	3.299	3.371

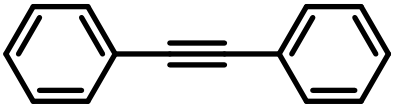

(a) Diphenylacetylene (or TW alone).

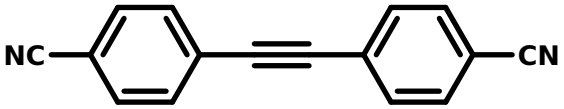

(b) Dicyano-substituted diphenylacetylene (or TW-CN).

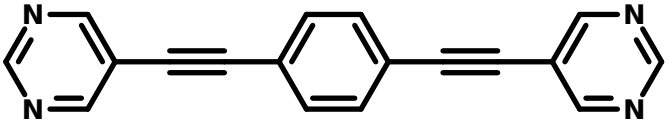

(c) Pyrimidine-substituted Tour wire based molecule in meta-position (or TW-Pyr N_{out}). [97]

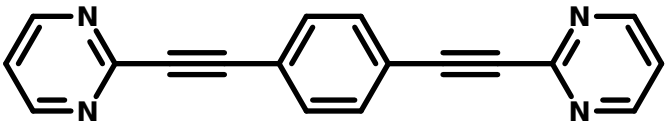

(d) Pyrimidine-substituted Tour wire based molecule in ortho-position (or TW-Pyr N_{in}). [97]

Figure 5.1.: Chemical structure of the molecules mentioned in this chapter.

The outcome of the geometry optimizations is very sensitive to the starting geometries (concerning the lateral position, but not the adsorption height). That's because the molecule does not move sufficiently far from its initial position. This also means that all the locations of the molecules on graphene are very similar in energy. It is thus very important to mention the starting geometries for which the ionic relaxations of the molecules have been performed. A mere translation of the molecule on the substrate only hardly affects the electronic structure (see figure 5.2), but rotating it leads to some changes. For the fundamental investigations performed in this thesis, we limit ourselves to just one of these geometries.

The optimized geometries, as resulting from a calculation with the nearest high symmetry position as starting position (which has the center of the molecule on top of a horizontal C-C bond of graphene) for the TW-CN, TW-Pyr N_{in} and TW-Pyr N_{out} molecules are presented in figure 5.3.

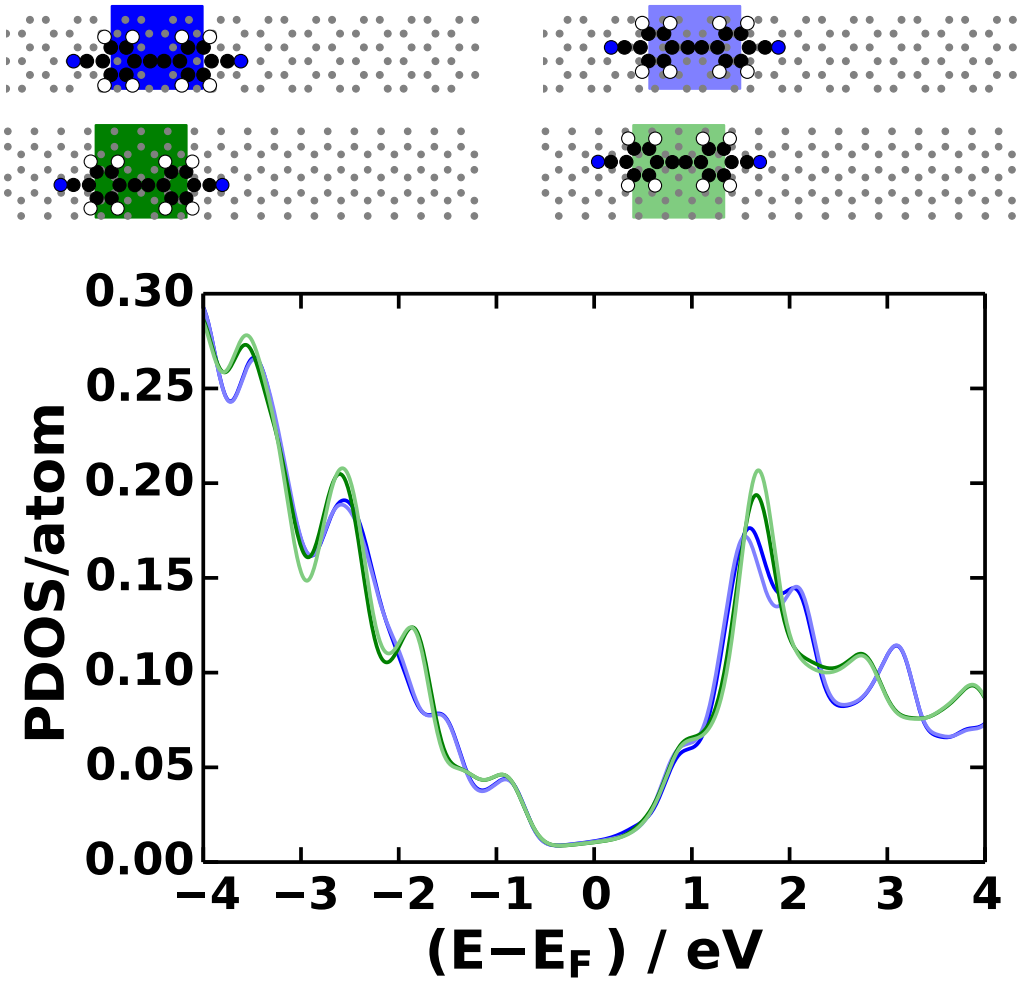

Figure 5.2.: PDOS averaged over the colored region for four different adsorption geometries (see the plots of the unit cells at the top) of TW-CN on graphene. The geometry optimization for each of the four systems was started from a different high symmetry position. The direction of the molecule is rotated by 90° when going from the upper row to the lower row and the molecule is shifted when going from left to right. The colors of the curves in the PDOS plot match the colors of the rectangles in the geometries.

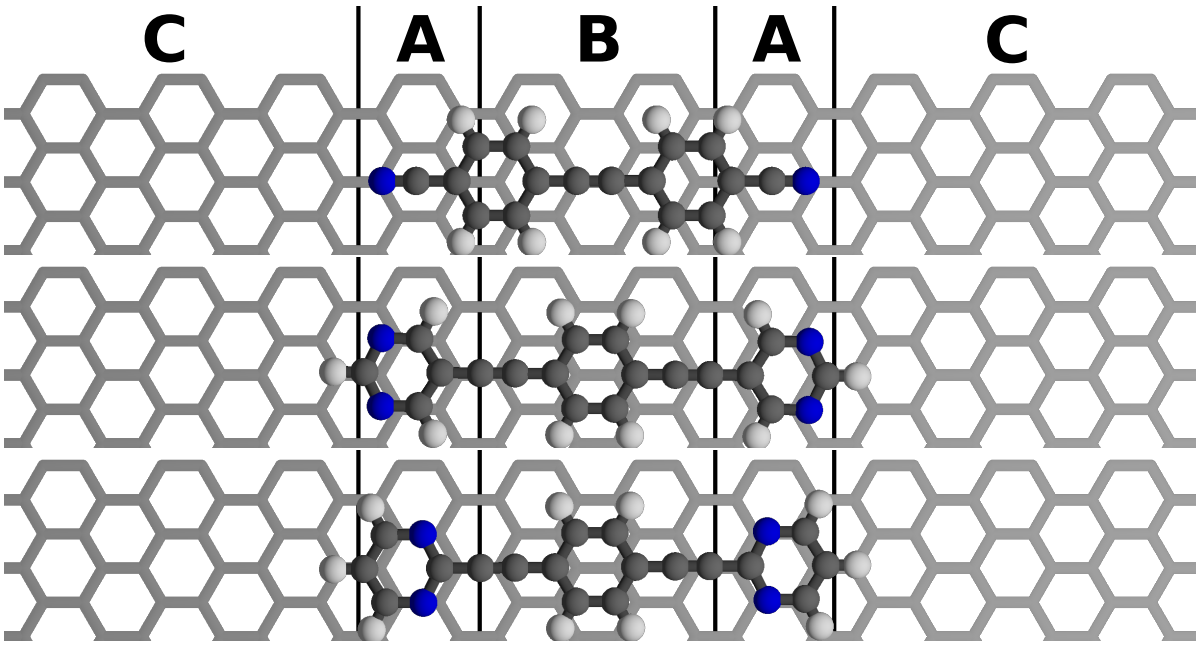

Figure 5.3.: Optimized geometries of the TW-CN (top), TW-Pyr N_{out} (middle) and TW-Pyr N_{in} (bottom) molecule adsorbed on graphene (one unit cell is shown). The adsorption height is given in table 5.1. In each of the unit cells, three regions are marked: one region below the dipolar end groups (region A), one region in-between the dipolar end groups below the molecule (region B) and one region where the graphene sheet is not covered by the molecule (region C).

5.2. Electrostatic Potential

There is a dipole potential, much like for the BN pairs, that originates from the end groups of the molecules. While the end groups act as dipoles, the fact that there is a mirror symmetry through the center of the molecule means that the molecule has no net dipole moment. However, the quadrupole moment tensor has entries different from zero. Figure 5.4 shows the electrostatic potential in the molecule plane for three of the investigated molecules[2]. The dipole of the endgroups of the TW-CN molecule points towards the x-direction, while the dipole of the TW-Pyr N_{out} molecule has the dipoles at an angle to the x-axis.

In the direction perpendicular to the molecule plane, the dipole potential drops like $1/r^3$ (where r is the distance from the plane). Thus, in the graphene plane, which is at a distance of 3 to 3.5 Å in z-direction, the effect of the dipolar endgroups of the molecules has already dropped quite significantly (see figure 5.5). The direction of the dipoles of the TW-Pyr N_{in} molecule is reversed compared to the other two molecules. Furthermore, it can be seen than the dipoles due to Pyrimidine rings in the TW-Pyr N_{out} case are weaker that in the TW-Pyr N_{in} and the TW-CN cases.

While the dipole moment of the end groups is not easily accessible, the total quadrupole moment of the molecules can be calculated with Gaussian (see table 5.2). Then, the different strengths of the dipolar end groups are also observed in the quadrupole tensor: When comparing Q_{xx} (because this is the direction perpendicular to the dipole lines that will eventually be formed by the molecules), the value is comparable for TW-CN and TW-Pyr N_{in} (but oppositely oriented), but the absolute value for the TW-Pyr N_{out} molecule is less than half the value of the other two molecules. Note that the quadrupole moments are only an apt means of comparing the dipole moments of end groups when the distance of the two dipoles is equal for all the molecules (i. e. they have the same size), but this is approximatively the case as can be seen from figure 5.4.

[2] These calculations were performed using hard pseudopotentials: `PAW_PBE C_h 06Feb2004`, `PAW_PBE H_h 06Feb2004` and `PAW_PBE N_h 06Feb2004` with a plane wave energy cutoff of 700 eV.

Table 5.2.: Traceless quadrupole moment of three molecules as calculated by Gaussian using PBEPBE/6-311G(d,p). The rows are the components of the quadrupole moment Q in eÅ^2 while the columns represent the different molecules.

Q/eÅ^2	**TW-CN**	**TW-Pyr N_{out}**	**TW-Pyr N_{in}**
XX	-11.92	-4.56	10.59
YY	7.83	3.43	-3.45
ZZ	4.08	1.14	-7.15
XY	-0.26	0.02	0.06
XZ	0.01	-0.46	-1.44
YZ	-0.18	-0.38	-1.10

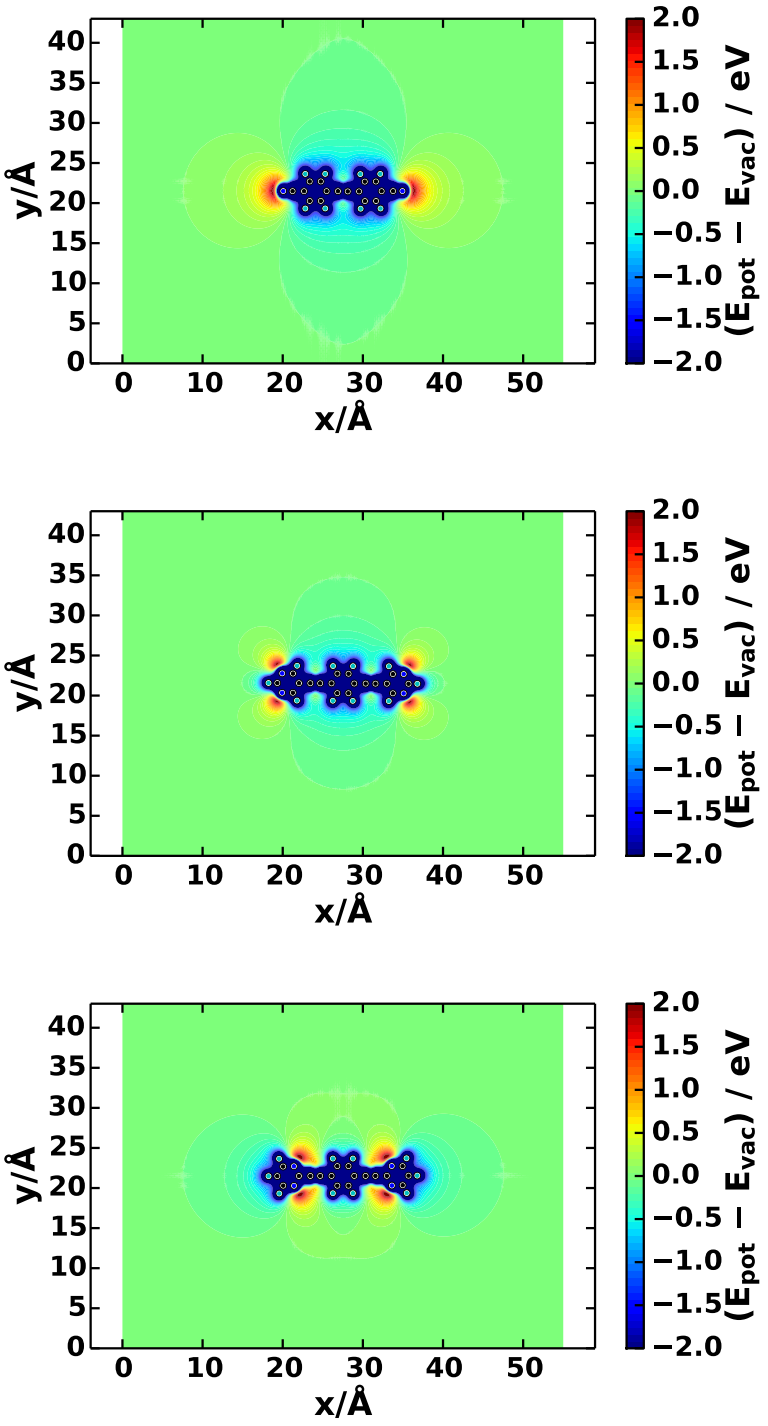

Figure 5.4.: Electron potential energy E_{pot} relative to the vacuum electron potential energy E_{vac} (given by E_{pot} at the point furthest away from the molecule in the unit cell). The calculation is done with one single molecule in a $55 \times 43 \times 40$ Å unit cell and a two-dimensional cut through the three-dimensional E_{pot} is taken in the molecule plane. The color range does not cover the full energy range of E_{pot}. Top: TW-CN, Middle: TW-Pyr N_{out}, Bottom: TW-Pyr N_{in}. For this calculation, hard pseudopotentials and a higher energy cutoff were used (see footnote 2 on page 81).

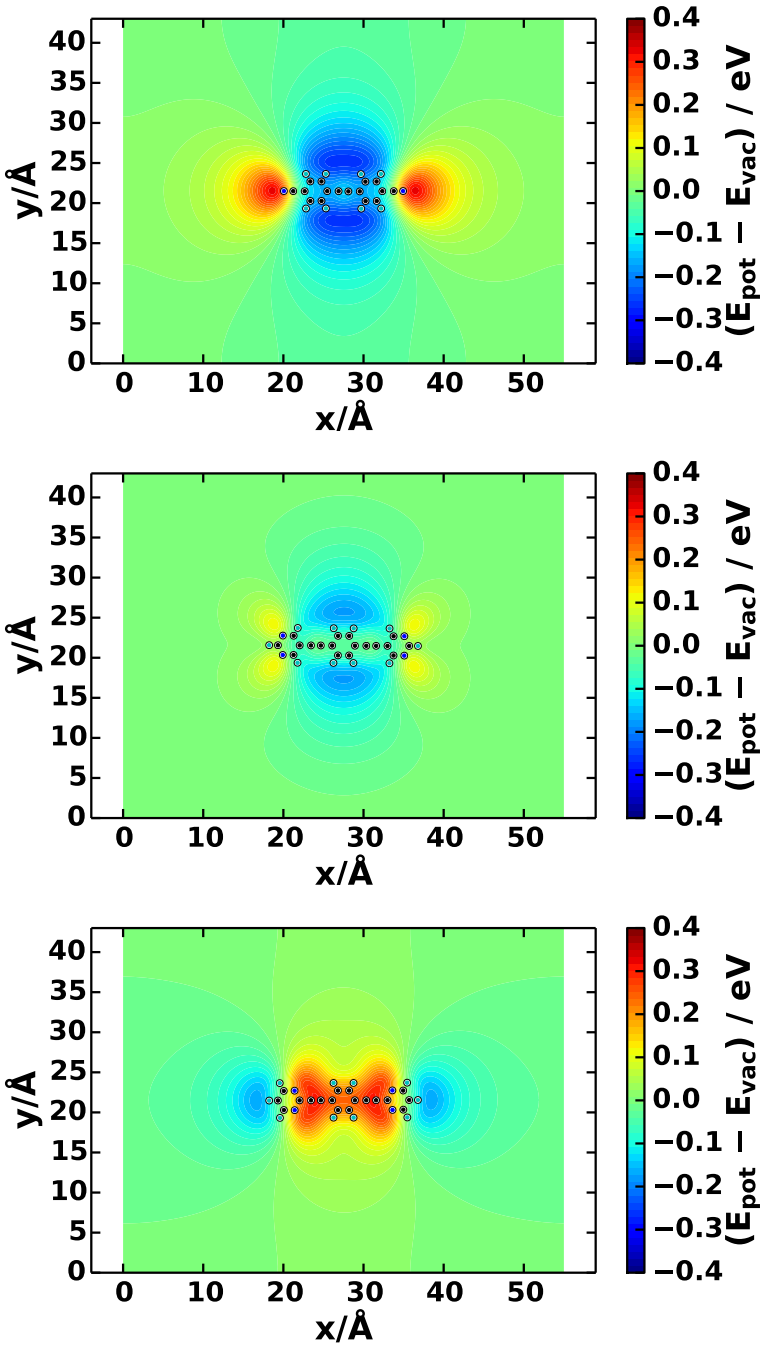

Figure 5.5.: Electron potential energy E_{pot} relative to the vacuum electron potential energy E_{vac} (given by E_{pot} at the point furthest away from the molecule in the unit cell). The calculation is done with one single molecule in a $55 \times 43 \times 40$ Å unit cell and a two-dimensional cut through the three-dimensional E_{pot} is taken in the would-be graphene plane, i. e. 3.33 Å below the molecule. Note that the color range is different than in figure 5.4, but here it covers the full energy range of E_{pot}. Top: TW-CN, Middle: TW-Pyr N_{out}, Bottom: TW-Pyr N_{in}. For this calculation, hard pseudopotentials and a higher energy cutoff were used (see footnote 2 on page 81).

Next, the electron potential energy change in the graphene plane that is caused by an adsorbed molecule will be investigated. This change can be calculated by substracting E_{pot} of a graphene sheet without any adsorbed molecule from E_{pot} of the total system (graphene and adsorbed molecule), both in the graphene plane. The result of this kind of analysis can be found in figure 5.6. The presence of the graphene plane changes the potential in two distinct ways.

First, the height of the potential difference below and outside the molecule is reduced by a factor of about 4.89. This is to be interpreted as a relative permittivity $\varepsilon = 4.89$ in graphene responsible for a linear screening of the potential. This value of ε is in the range found by experiment. [98] It is not necessary to allow for an additional exponential screening term (as inspired by Thomas-Fermi theory) here, presumably because the distance of the out-of-plane dipoles is too large and the charges to be screened are not embedded in the material anymore.

Secondly, there is a constant shift of about 0.004 eV. This is not really physically relevant, because it depends on which vacuum level one chooses. There is a difference of the vacuum levels due to the formation of a bond dipole due to the pushback effect. [89] The dipole created by this pushback splits space in two halves, as expected (see chapter 2.2.3) for a two-dimensional array of dipoles (due to the periodic boundary conditions used). In each of these halves, there is a different vacuum energy (see figure 5.7). However, the formation of the dipole only happens when both the graphene layer and the molecule are present. Depending on which vacuum level is chosen for comparing the different systems, there is a different constant shift between the two curves. More on the bond dipole can be found in chapter 5.4.

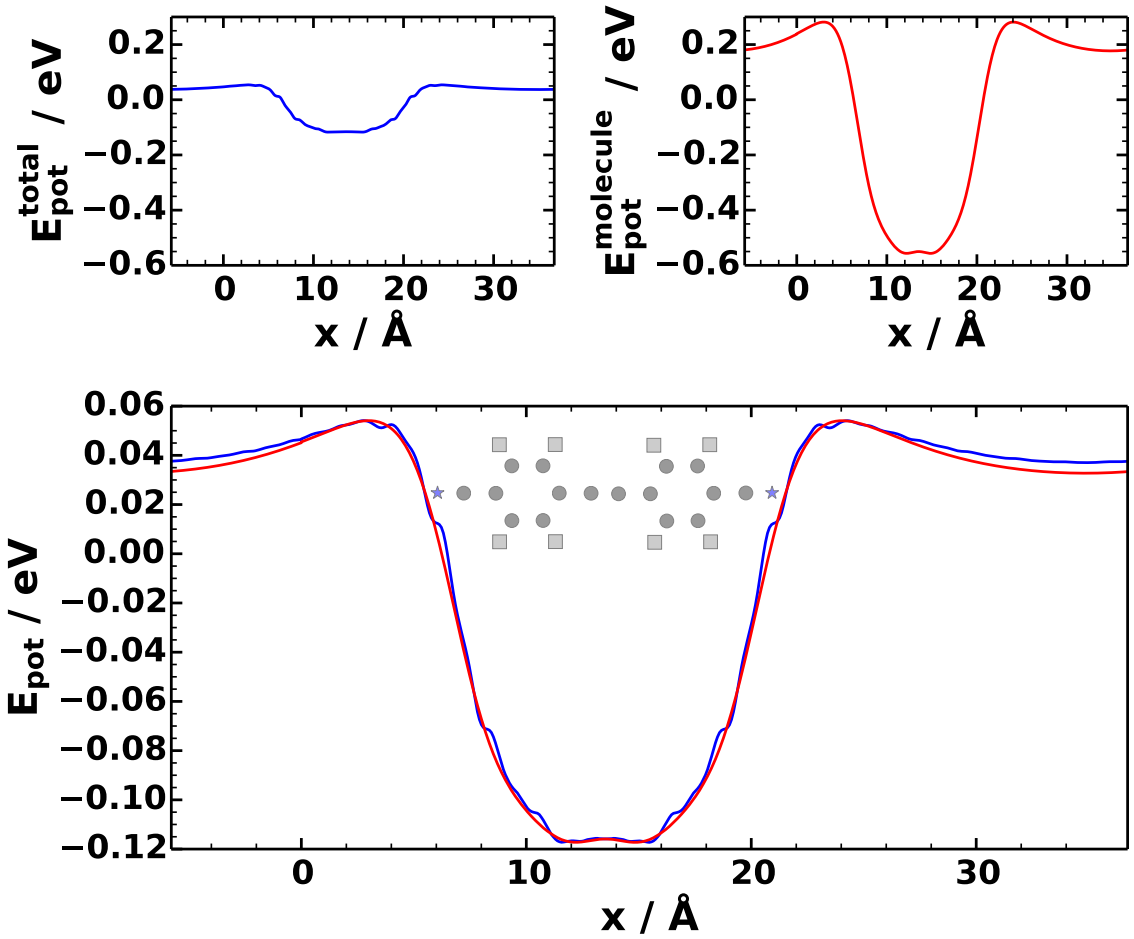

Figure 5.6.: Electron potential energy change E_{pot} (with the vacuum energy as zero) caused by the TW-CN molecule in the graphene plane (averaged in the y-direction). Top left: in presence of the graphene sheet. Top right: without graphene sheet, but in the plane where the graphene sheet would be. Bottom: The same data, but the red curve without graphene sheet transformed according to the linear function $E'_{pot} = (1/4.89)E_{pot} - 0.004$ (in eV). The symbols mark the x-positions of the atoms in the molecule.

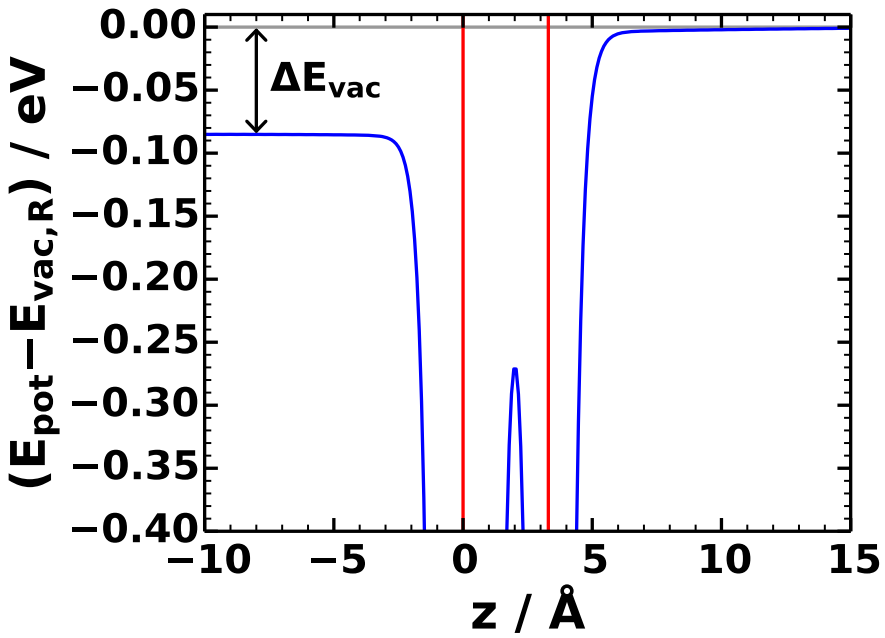

Figure 5.7.: Electron potential energy, xy-plane averaged, for a graphene sheet (at $z = 0$ Å) with an adsorbed TW-CN molecule (at a mean adsorption height of $z = 3.344$ Å, see table 5.1). Here, the size of the unit cell in z-direction is 40 Å and the dipole correction was used (see chapter 3.1). The two red vertical lines show the position of the graphene sheet and the molecule. The right vacuum level is set to zero. There is a vacuum level difference ΔE_{vac} of 0.08 eV between the left and right region due to the two-dimensional array of bond dipoles.

5.3. Energetic Shift of the DOS

As in the systems with substitutional BN pairs, the change of E_{pot} is expected to lead to a shift of the energy of the individual states and thus an energy shift of the PDOS of C atoms with altered E_{pot}.

Figures 5.8, 5.9 and 5.10 show the averaged PDOS in three regions of the graphene sheet for a system with adsorbed TW-CN, TW-Pyr N_{out} and TW-Pyr N_{in} molecules. For TW-CN and TW-Pyr N_{out}, the PDOS of the atoms below the molecule in-between the dipoles is shifted towards lower energies. For TW-Pyr N_{in}, however, the energy shift is in the opposite direction, as expected for a molecule with the dipoles pointing in the other direction. The total effect, measured as the energy shift between the atoms in between the dipoles and outside, is very small. The explanation is that the potential energy shift is not very high because of the adsorption distance and screening effects (as discussed in chapter 5.2).

We find the largest energy shift (of the three cases investigated) for the TW-CN molecule. For the TW-Pyr N_{in} molecule, the value of the energy shift is only slightly smaller, but going in the opposite direction. The smallest energy shift is found for the TW-Pyr N_{out} molecule.

Furthermore, for all three molecules (figures 5.8, 5.9 and 5.10), especially around the Fermi level the characteristic shape of the DOS of graphene is lost. It is more flattened out than for pure graphene. In this aspect, this is similar to what was observed for graphene with substitutional BN pairs. Still, the graphene sheet in the systems with adsorbed molecules has a very low PDOS around the Fermi level. The PDOSes of all the three molecules are even zero at the Fermi level. They have a band gap and are, thus, semiconducting.

When starting at the Fermi level and going to higher energies, the first substantial peak in the DOS comes from the adsorbed molecules (in all three cases). Therefore, when bringing extra electrons into the system, they would mainly go to the lowest unoccupied molecular orbital (LUMO) of the molecule. For the BN pair substituted graphene sheets, the occupied states nearest to E_F were sitting on the modifiers (the BN pairs). Here, in contrast, the *unoccupied* states nearest to E_F sit on the modifiers (the molecules).

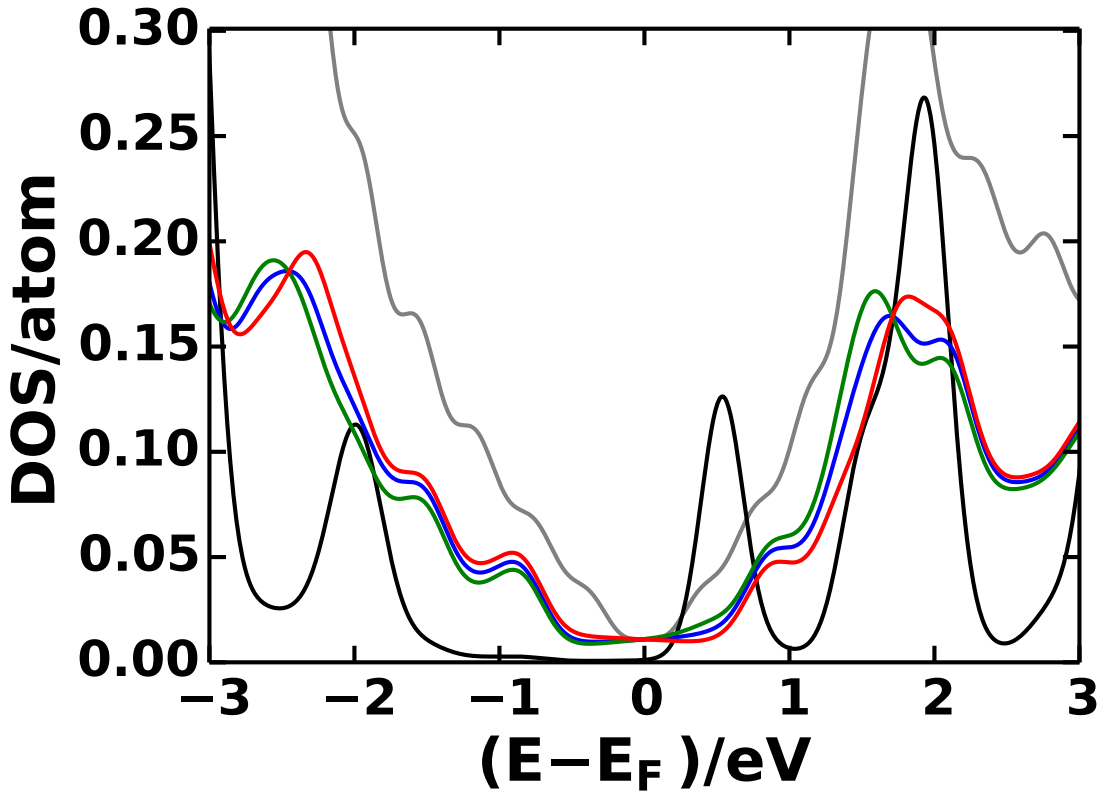

Figure 5.8.: Density of states projected onto the C atoms in a graphene sheet where a TW-CN molecule is adsorbed. The PDOSes are averaged over all the atoms in the different regions shown in figure 5.3: region A in blue, B in green, C in red. The PDOS averaged over all the atoms belonging to the molecule is plotted in black. For comparison, the DOS/atom of pure graphene is plotted as well (gray curve). Here, the PDOSes were "resmeared" with *SIGMA* = 0.2 eV.

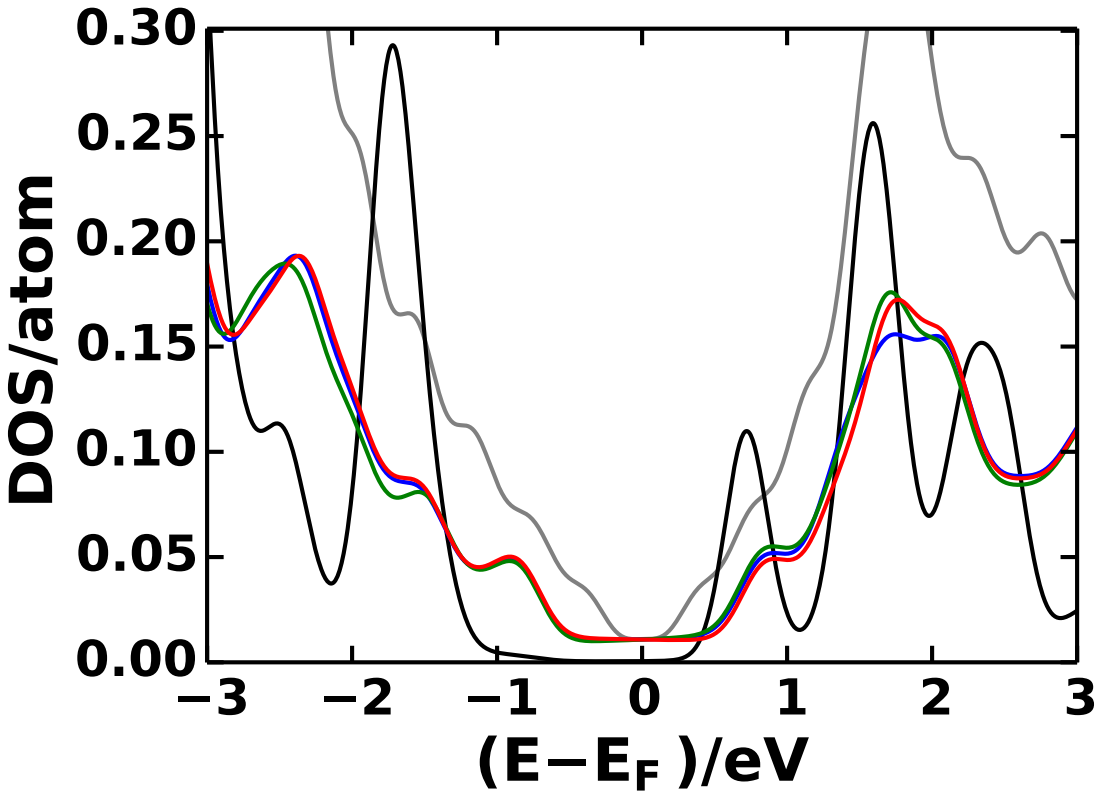

Figure 5.9.: Density of states projected onto the C atoms in a graphene sheet where a TW-Pyr N_{out} molecule is adsorbed. The PDOSes are averaged over all the atoms in the different regions shown in figure 5.3: region A in blue, B in green, C in red. The PDOS averaged over all the atoms belonging to the molecule is plotted in black. For comparison, the DOS/atom of pure graphene is plotted as well (gray curve). Here, the PDOSes were "resmeared" with *SIGMA* = 0.2 eV.

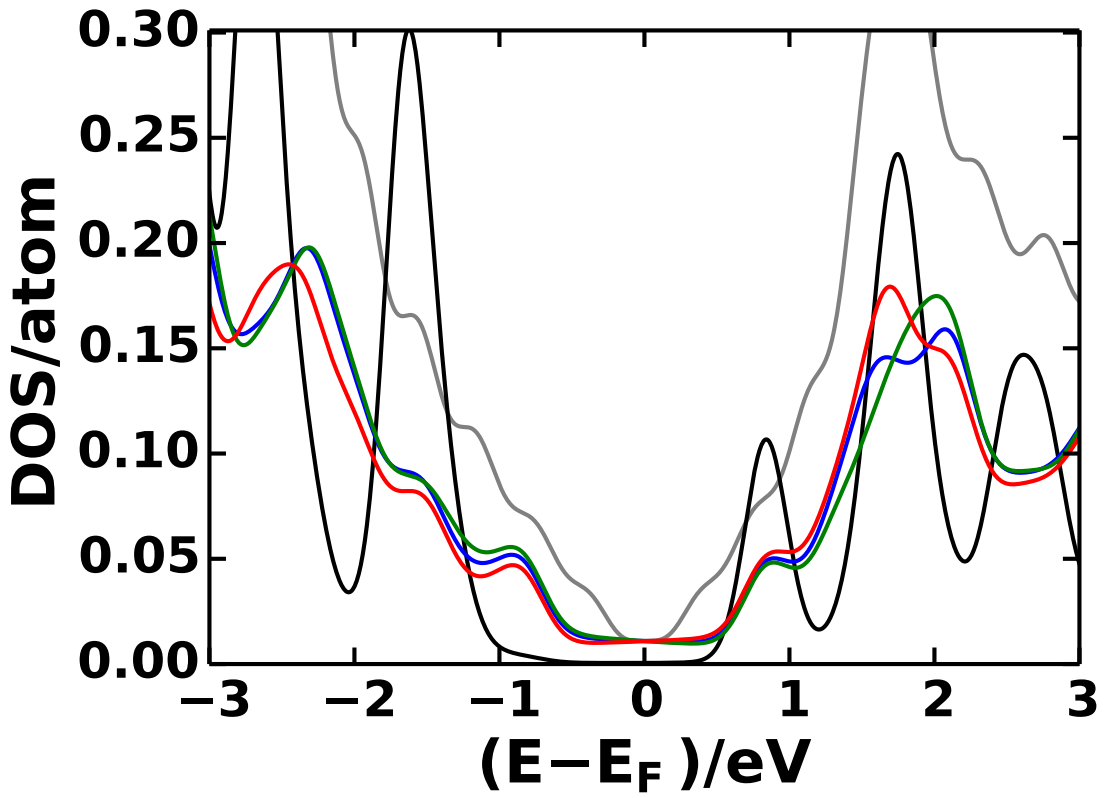

Figure 5.10.: Density of states projected onto the C atoms in a graphene sheet where a TW-Pyr N_{in} molecule is adsorbed. The PDOSes are averaged over all the atoms in the different regions shown in figure 5.3: region A in blue, B in green, C in red. The PDOS averaged over all the atoms belonging to the molecule is plotted in black. For comparison, the DOS/atom of pure graphene is plotted as well (gray curve). Here, the PDOSes were "resmeared" with *SIGMA* = 0.2 eV.

5.4. Charge Rearrangements

Due to the adsorption of the molecule, the electron density both in the molecule and in the graphene sheet changes. For preserving the mainly electrostatic nature of the effect, these charge rearrangements should not be too big.

Chapter 3.9 describes how charge rearrangements are calculated. The results from this calculation for the TW-CN molecule on graphene are shown in figure 5.11.

The total amount of transferred charges $Q(z)$, figure 5.11a (ii), is negative for nearly the whole unit cell. Hence, all in all, electrons are transferred from the graphene layer to the molecule (see also 5.11b and 5.11c). However, compared to other typical systems of monolayers adsorbed on various substrates, these charge rearrangements are fairly small. [5, 89, 99] But as the electrostatic effects investigated in this work are also rather small, it cannot be ruled out that these charge redistributions also influence the electronic behavior of the examined systems.

The redistribution of charge gives rise to a bond dipole, which is pointing from the molecule to the substrate. It leads to a potential energy shift of 0.08 eV (see figure 5.11a (iii)), which corresponds to a bond dipole moment of 0.14 eÅ per unit cell. The bond dipole curve can be calculated in two ways: by integrating $Q(z)$ or by calculating the change of the electron potential energy upon adsorption (see chapter 3.9). There is a very slight mismatch between these two curves in figure 5.11a (iii) because the automatic dipole correction overcompensates the dipole layer a little bit. However, the agreement is sufficiently good.

The charge redistribution is shown three-dimensionally in figures 5.11b and 5.11c. The isosurfaces around the molecule are mainly colored in blue, which means that the charge is transferred from the graphene sheet to the molecule (as already concluded from figure 5.11a (ii)). A lot of this transferred charge can be found at the nitrogen atoms in the cyano groups.

In the graphene plane, further charge rearrangements can be seen. The region below the nitrogen atoms in the dipolar endgroups loses electrons (see the large red areas in figures 5.11b and 5.11c). In contrast, the carbon rings between two molecules in y-direction show a large electron accumulation (see the large blue area in figure 5.11b). This could be due to the dipole lines, as the electrons move to regions with lower potential energy. This rearrangement of electrons counteracts the dipole potential, which leads to the screening discussed in context of figure 5.6. The electron density of the carbon rings right below the molecular backbone changes only slightly. Somehow the molecular backbone seems to prevent electrons from accumulating there, and, therefore, the electron accumulation only appears between the molecules and not below. The reason for this behavior is not clear.

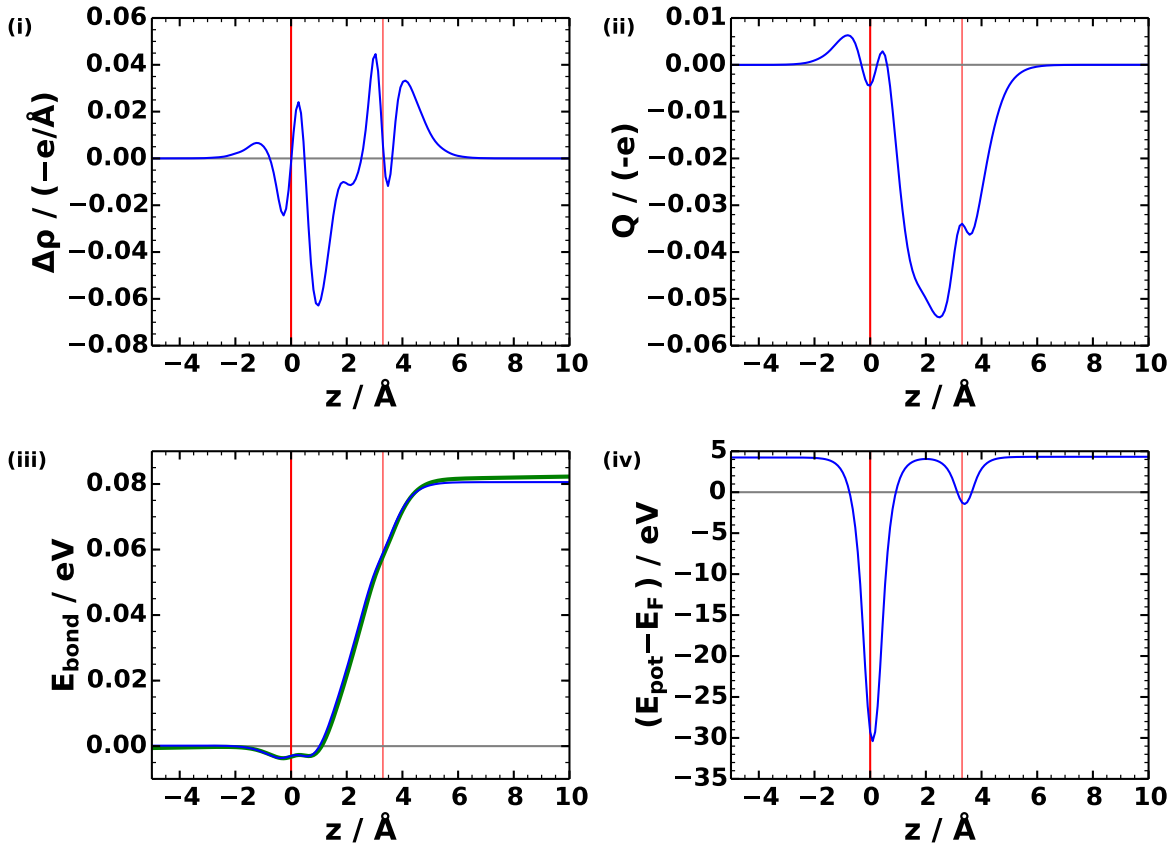

(a) (i) Charge rearrangements $\Delta\rho(z)$. (ii) Total amount of flown charge $Q(z)$. (iii) Resulting bond dipole $E_{\text{bond}}(z)$ calculated by integration of $Q(z)$ (blue line) and directly from the VASP potential energies (green line). (iv) Electrostatic potential of the total system, showing the position of the graphene sheet and the molecule. The two vertical red lines mark the position of the graphene sheet (left) and the molecule (right). Here, 40 Å of vacuum and the dipole correction were used.

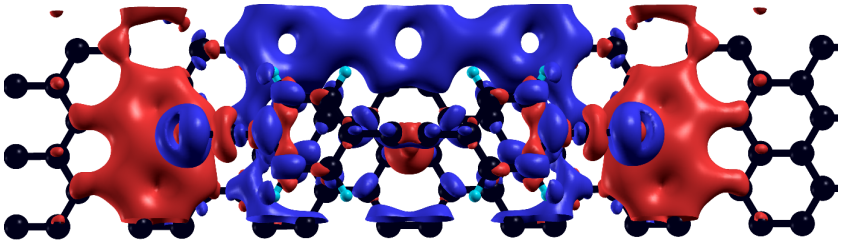

(b) Isosurface of $\Delta\rho$ at $\pm 10^{-3}$ (−e/Å^3), top view. Blue means electron accumulation, red means reduction of the electron density.

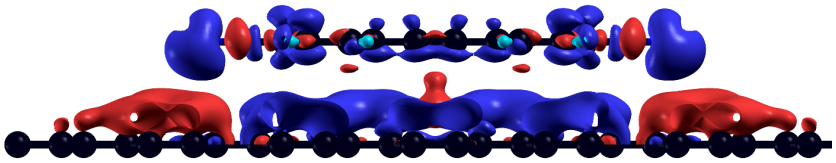

(c) Isosurface of $\Delta\rho$ at $\pm 10^{-3}$ (−e/Å^3), side view.

Figure 5.11.: Charge rearrangements due to the adsorption of the TW-CN molecule on graphene. Isosurface plots produced with XCrysDen [94].

6. Hexagonal Boron Nitride with Adsorbed Molecules

Due to the large dielectric constant of graphene, the potential caused by the dipolar end groups of adsorbed molecules is substantially reduced (see chapter 5.2). The isolating material *hexagonal boron nitride* (hBN) is expected to have a lower ε than graphene. [100] Therefore, the potential will not be screened as efficiently and the PDOS energy shift is expected to be higher. Furthermore, splitting electrons and holes and localizing them in different spatial regions could be feasible in semiconductors and isolators (see chapter 4.3.5).

6.1. Hexagonal Boron Nitride

A monolayer of hexagonal boron nitride (hBN) has the same structure as graphene, but with a broken sublattice symmetry: one of the sublattices is occupied by boron atoms, the other by nitrogen atoms. As with graphene, only single layers will be considered[1]. The bond distance is comparable to that of graphene, in the range of 1.4 Å. [101, 102] Lattice and ionic relaxations using GADGET lead to a value of 1.42 Å. The breaking of the sublattice symmetry causes the opening of a band gap (see chapter 2.4.5). In the flavor of DFT used throughout this thesis, the band gap comes out as 4.6 eV (see DOS in figure 6.1). As typical for Kohn-Sham theory, this value underestimates the real gap. [103] Values for the excitonic band gap obtained by optical experiments [104] and for the fundamental gap from GW calculations [105] are at around 6 eV.

The DOS plot in figure 6.1 also shows that the unoccupied levels are mainly provided by the boron atoms while the occupied levels are sitting mostly on the nitrogen atoms. Again, the DOS above the vacuum level (the right vertical line in figure 6.1) is wrong because without special precautions VASP does not describe unbound states correctly.

[1] While in principle the relationship of hexagonal boron nitride to a monolayer of the material is similar to the relationship of graphite to single-layer graphene, when we refer to hBN only one single planar sheet of the material is meant in this thesis.

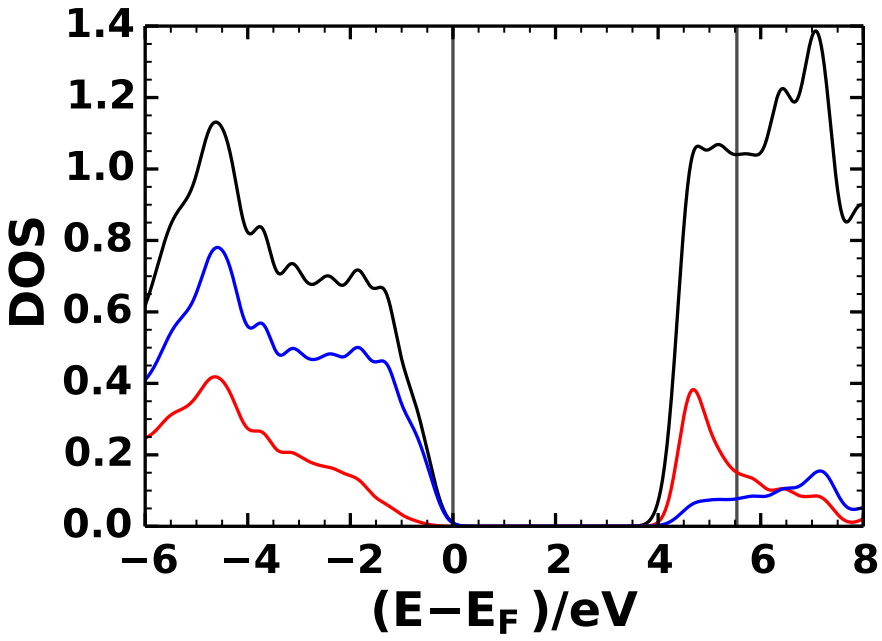

Figure 6.1.: Density of states of a monolayer of hexagonal boron nitride (hBN). Black line: total DOS, red line: PDOS of the B atom, blue line: PDOS of the N atom. The band gap can nicely be seen (due to the smearing it looks smaller than the values extracted from the raw data). The Fermi and vacuum levels are marked by gray vertical lines (the position of the Fermi level inside the gap is arbitrary: VASP puts it at the valence band edge). The fact that the individual PDOSes do not always sum up to the total DOS is an artifact of the projection scheme used by VASP (see the chapter on RWIGS in the VASP manual [82]).

6.2. Preliminary Discussion: Be and O in hBN

In the spirit of embedding boron and nitrogen atoms in graphene sheets, similary beryllium and oxygen atoms can be used as a dipolar pair of atoms in hBN. This system is very far from realistic and just acts as a logical extension of the graphene with BN pairs systems to sheets of hBN. Due to the loss of sublattice symmetry when going from graphene to hBN, the choices for incorporating Be and O atoms into the planar material are very limited if one requires the total unit cell to have no net dipole moment. The inclusion of Be and O distorts the lattice quite considerably (see figure 6.2).

The resulting modification of the electron potential energy is shown in figure 6.3: The B and the N atoms are equally affected by the dipoles, as expected from the simple electrostatic picture. All in all, the resulting curves look very similar to the graphene with BN pairs case (see figure 4.3). This similarity is very pronounced in the region with lowered potential, however in the region with higher potential the characteristic drop of the electron potential energy with increasing distance to the dipole lines is not present.

For a strip width of about 20 Å, the resulting shift of E_{pot} is approximately 1.5 eV. This is large compared to the graphene sheets with BN pairs.

These observations can be attributed to effects beyond the different reaction of hBN and graphene to dipolar fields: Firstly, the placement of the heteroatoms is very different in the two systems. Secondly, the massive lattice distortions change the electronic properties of the hBN system. Thirdly, there is a net dipole moment in the y-direction (due to the lattice distortion), which creates additional unwanted effects. Finally, there is no reason why the dipole moment of a pair of Be and O in hBN is similar or even compareable to the dipole moment of a pair of B and N in graphene. Due to this vast number of possible sources for the differences in behavior, which cannot be separated, it is not sensible to continue to examine the inequality of graphene and hBN by comparing BN pair substituted graphene with this system.

A more promising way to compare graphene and hBN is by looking at the adsorption of molecules.

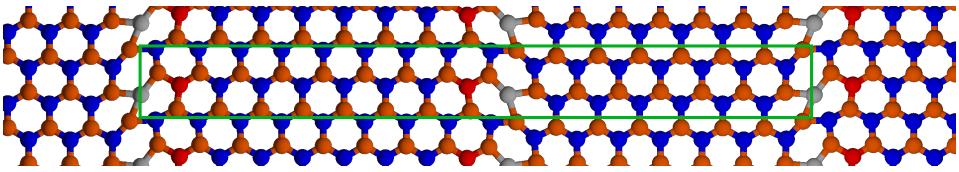

Figure 6.2.: GADGET-optimized two-dimensional structure of a sheet of hBN (orange: B atoms, blue: N atoms) with pairs of Be (gray) and O (red) atoms. The unit cell is shown in green.

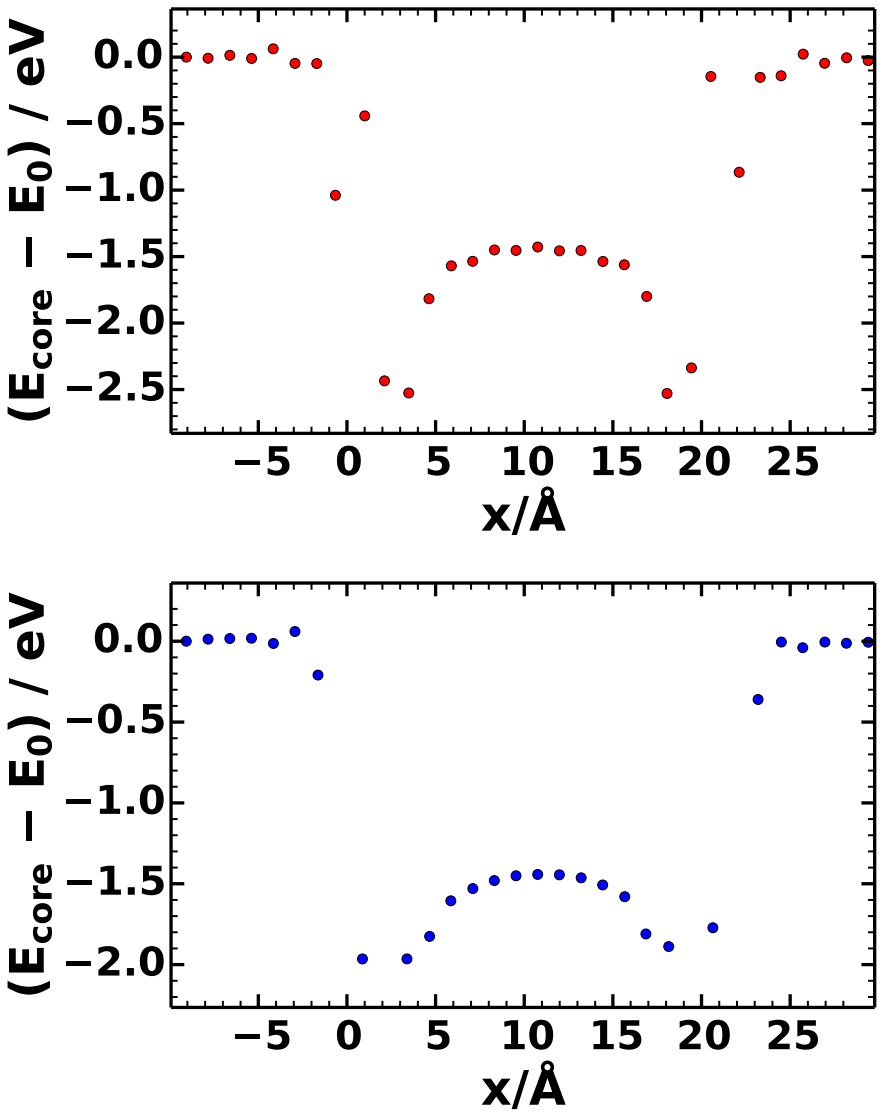

Figure 6.3.: Electron potential energy at the core relative to the leftmost plotted atom for the B atoms (top) and the N atoms (bottom) in hBN with substitutional Be and O atoms (see figure 6.2).

6.3. Adsorption Geometries

In contrast to the difficulties concerning comparability between graphene and hBN with in-plane dipoles, comparing the two different planar materials with adsorbed molecules is straightforward.

In analogy to the geometries used for the adsorbed molecules on graphene (see figure 5.3), the same three molecules (TW-CN, TW-Pyr N_{out} and TW-Pyr N_{in}) are investigated on hBN (see figure 6.4). Again, starting from high symmetry positions[2], the atoms belonging to the molecule were allowed to move during a geometry relaxation with GADGET, while the B and N atoms in the hBN sheet were kept at their fixed positions (for more methodological details see chapter 3.2). The adsorption heights (table 6.1) are very similar to the adsorption heights on graphene (table 5.1).

[2] Although the symmetry is lowered compared to graphene because of the breaking of the sublattice symmetry.

Table 6.1.: Adsorption height of the individual molecules regularly adsorbed on a sheet of hBN: maximum (h_{max}), minimum (h_{min}) and average ($\bar{h}$).

Molecule	h_{max}/Å	h_{min}/Å	$\bar{h}$/Å
TW-CN	3.390	3.300	3.348
TW-Pyr N_{out}	3.403	3.324	3.355
TW-Pyr N_{in}	3.413	3.254	3.349

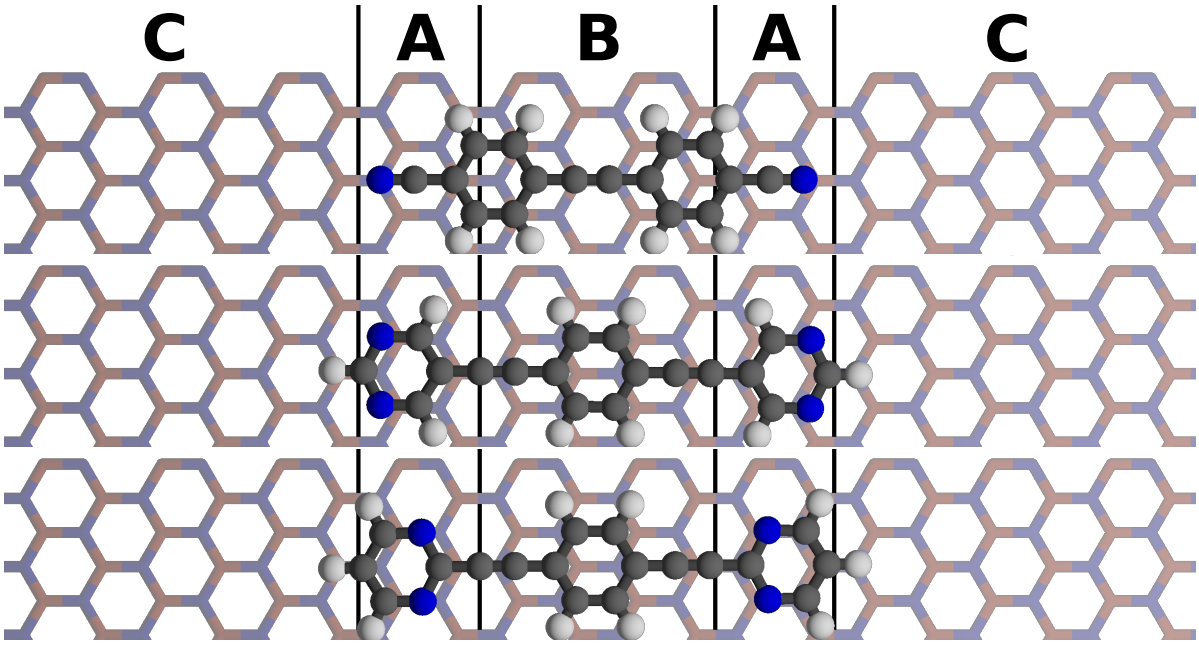

Figure 6.4.: Optimized geometries of the TW-CN (top), TW-Pyr N_{out} (middle) and TW-Pyr N_{in} (bottom) molecule adsorbed on hBN (one unit cell is shown). In the substrate, bonds around boron atoms are colored in orange, nitrogen in blue. The adsorption height is given in table 6.1. In each of the unit cells, three regions are marked: one region below the dipolar end groups (region A), one region in-between the dipolar end groups below the molecule (region B) and one region where the hBN sheet is not covered by the molecule (region C).

6.4. Electrostatic Potential

As for graphene, the electron potential energy change upon adsorption of a TW-CN molecule on hBN will be investigated (see figure 5.6 for the graphene counterpart). The presence of the hBN sheet linearly screens the potential of the dipolar end groups of the molecule (see figure 6.5). There is a reduction of E_{pot} by a factor of 1.74, which can again be attributed to a relative dielectric constant ε. The ratio of the this linear screening for hBN and graphene is about 2.8. Outside the part of the hBN layer that is covered by the molecule, the potential drops far less quickly than without the presence of the hBN. There is presumably a polarization of the hBN sheet that counteracts this drop. This is a huge contrast to the behavior of in-plane dipoles in graphene, where Thomas-Fermi like nonlinear screening causes E_{pot} to fall more quickly. The reason for this discrepancy remains unclear.

The constant shift, here in the range of −0.065 eV, again depends on the choice of the vacuum potential. Its value is physically irrelevant.

To find out more about the differences between the screening behavior of graphene and hBN, the electron potential energy in the plane of the two-dimensional material is compared for these two materials (see figure 6.7). Here, in addition to the TW-CN, TW-Pyr N_{out} and TW-Pyr N_{in} molecules discussed so far, three other molecules are shown for comparison (see figure 6.6). While they also look promising, they have not been further investigated because this would have surpassed the scope of this thesis. It should be noted that the adsorption geometry of these molecules was not optimized. This means that the adsorption height was arbitrarily chosen (as 3 Å, a value that is about 10% too low at least for TW-CN, TW-Pyr N_{out} and TW-Pyr N_{in}) and also the x and y adsorption position was arbitrary[3]. To get a feeling for the error that is caused by using this geometry, a comparison of the TW-CN molecule here and in an optimized adsorption geometry (as discussed above) can be made: While the shift on graphene is −0.20 eV here, in the relaxed geometry it is only −0.16 eV, which is most likely mainly due to the larger adsorption distance. On hBN, the shift is −0.56 eV here and −0.50 eV in the relaxed geometry.

In general, the shift in E_{pot} caused by the molecules is larger in hBN than in graphene. For TW-CN, TW-NO_2 and TW-NC, the factor is about 2.8. For TW-Pyr N_{out} and TW-Pyr N_{out} CN, the factor is higher, for TW-Pyr N_{in} it is lower. This discrepancy probably stems from the different size and number of rings of these molecules.

In general, the other molecules, i. e. TW-Pyr N_{out} CN, TW-NO_2 and TW-NC, also look promising as the effect in the potential caused by them is comparable to or surpassing the TW-CN molecule. The molecules with pyrimidine rings as the only dipolar groups are less suited. However, TW-Pyr N_{in} is the only molecule with reversed dipoles included here.

[3] The center of the molecules were at $x = 3.18$ Å for the TW-CN molecule, at $x = 0.74$ Å for the TW-Pyr N_{out} molecule, at $x = 0.74$ Å for the TW-Pyr N_{in} molecule, at $x = 2.60$ Å for the TW-NO_2 molecule, at $x = 3.13$ Å for the TW-NC molecule, and at $x = 0.71$ Å for the TW-Pyr N_{out} CN molecule. These positions are measured from the x position of a boron atom in the hBN sheet. All the centers of the molecules were put at the same y-positions as a boron atom in the hBN sheet.

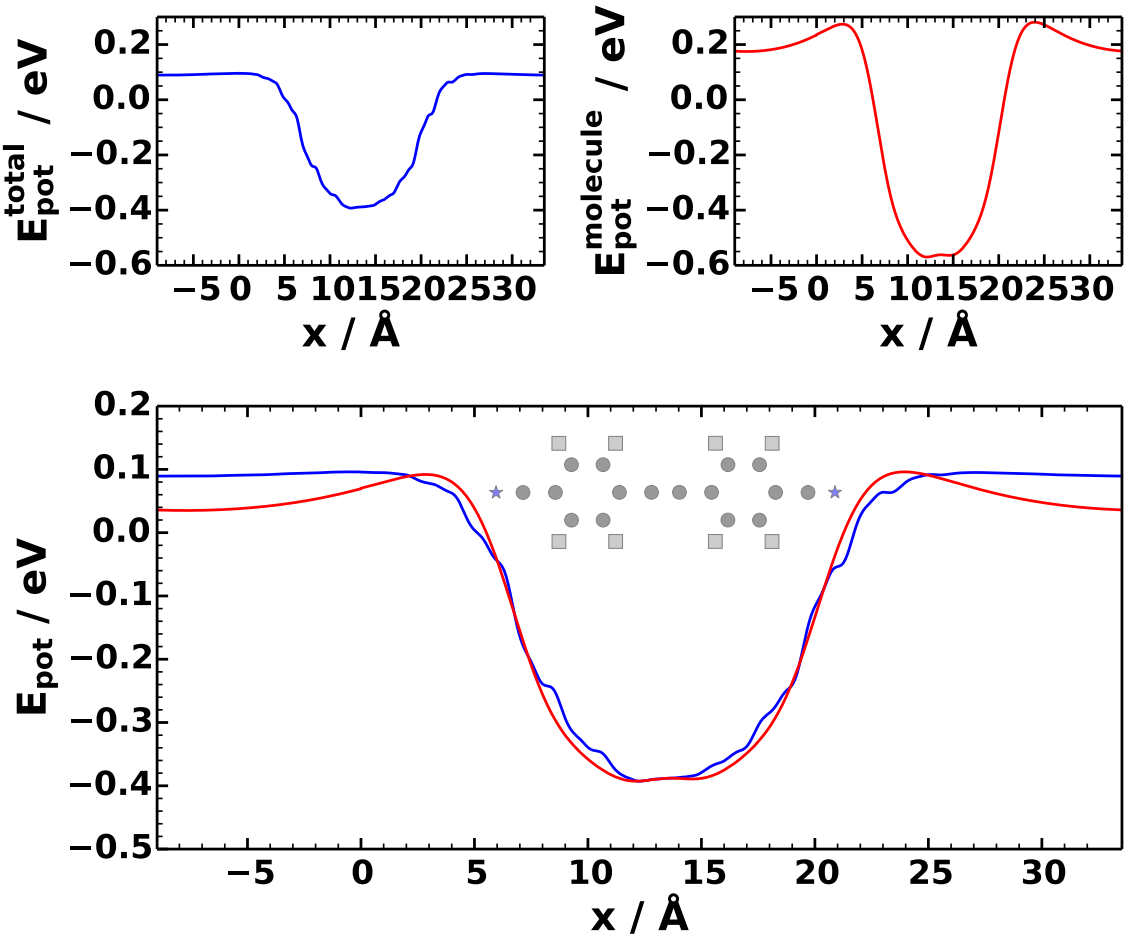

Figure 6.5.: Electron potential energy change E_{pot} (with the vacuum energy as zero) caused by the TW-CN molecule in the hBN plane (averaged in the y-direction). Top left: in presence of the hBN sheet. Top right: without hBN sheet, but in the plane where the hBN sheet would be. Bottom: The same data, but the red curve without hBN sheet transformed according to the linear function $E'_{pot} = (1/1.74)E_{pot} - 0.065$ (in eV). The symbols mark the x-positions of the atoms in the molecule.

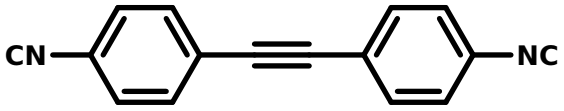

(a) Di-isocyano-substituted diphenylacetylene (or TW-NC).

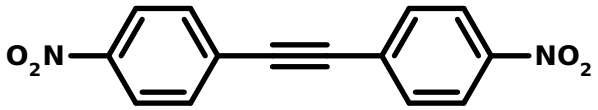

(b) Dinitro-substituted diphenylacetylene (or TW-NO_2).

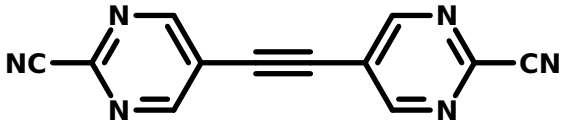

(c) (Ortho)-dicyano-substituted dipyrimidine acetylene (or TW-Pyr N_{out} CN).

Figure 6.6.: Chemical structure of the three molecules discussed here in addition to the figures presented in figure 5.1.

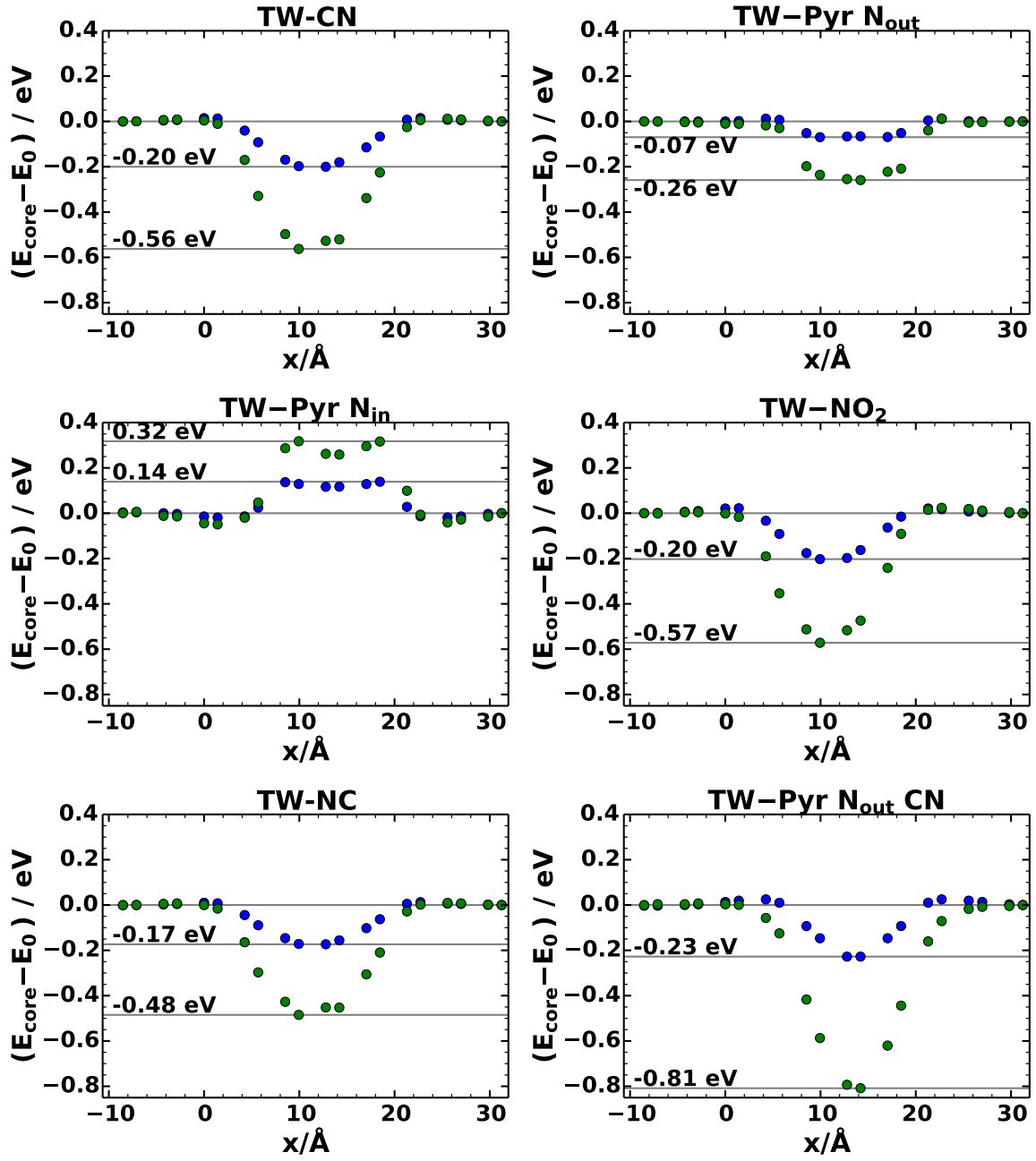

Figure 6.7.: Electron potential energy at the core of the atoms in the two-dimensional material at $y = 0$ (i. e. at the lower boundary of the unit cell) with different molecules adsorbed. The data points for graphene are plotted in blue, hBN in green. The rightmost plotted datapoint is aligned to zero potential. Here, no additional geometry optimization of the molecules has been performed, but the Gaussian geometries are used in an adsorption distance of $h = 3\,\text{Å}$.

6.5. Energetic Shift of the DOS

The characteristic energy shift of the site-projected density of states, averaged over different regions, is again a nice way to assess the impact of the collective dipole potential on the energy of the individual states. Figures 6.8, 6.9 and 6.10 show this quantity for the TW-CN, TW-Pyr N_{out} and TW-Pyr N_{in} molecule. The shift of the PDOSes relative to each other is clearly visible. It is considerably larger than for graphene sheets, as expected from the electrostatic considerations. In the gap, there are states that are localized on the molecules. These are the first states above the Fermi level, so excited or excess electrons would occupy these states. This observation is similar to the one made for molecules adsorbed on graphene, where extra electrons would also be found on the molecule.

The different directions of the shift between TW-Pyr N_{out} and TW-Pyr N_{in} is again present. For the unoccupied states, there seems to be a problem when one compares pure hBN to the site-projected PDOS: this happens for the same reason discussed in the caption of figure 6.1, i. e. it is an artefact of the projection method.

In total, semiconducting or isolating ultra-thin materials like hBN seem to be better suited for the electrostatic modification of their electronic structure, because a separation of electron and hole states in different regions could be feasible with carefully chosen modifiers.

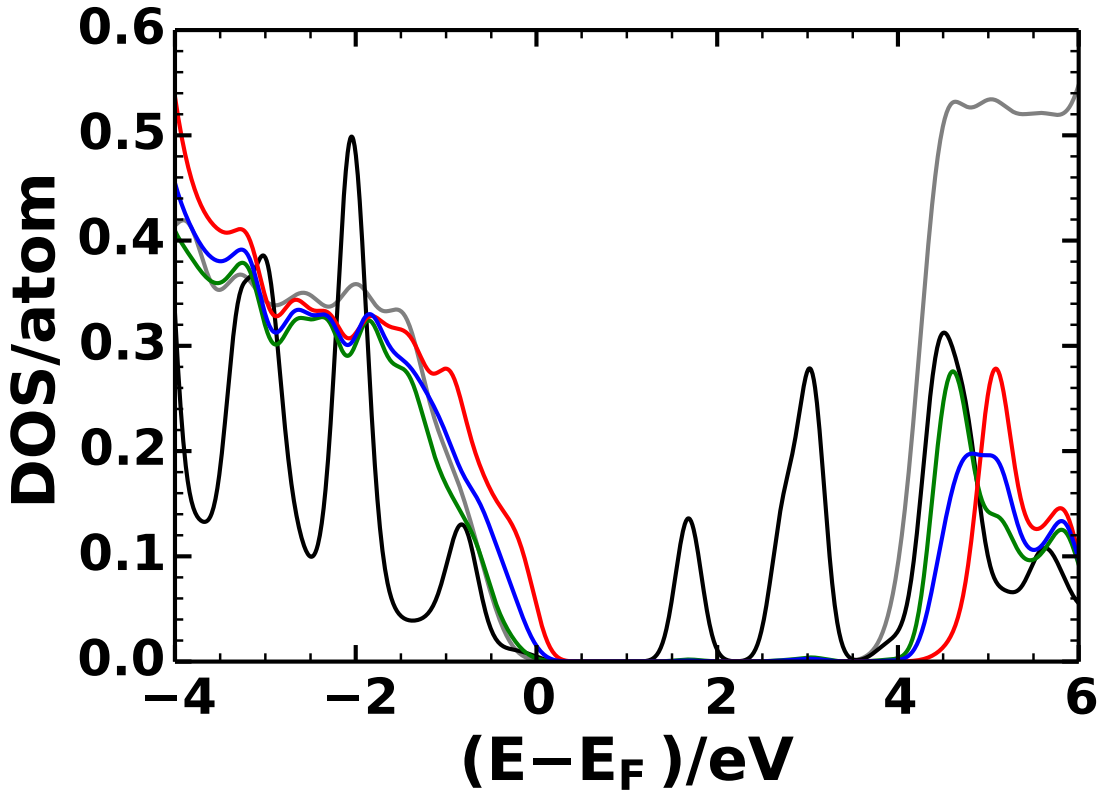

Figure 6.8.: Density of states projected onto the C atoms in a hBN sheet where a TW-CN molecule is adsorbed. The PDOSes are averaged over all the atoms in the different regions shown in figure 6.4: region A in blue, B in green, C in red. The PDOS averaged over all the atoms belonging to the molecule is plotted in black, the DOS per atom of pure hBN is plotted in gray.

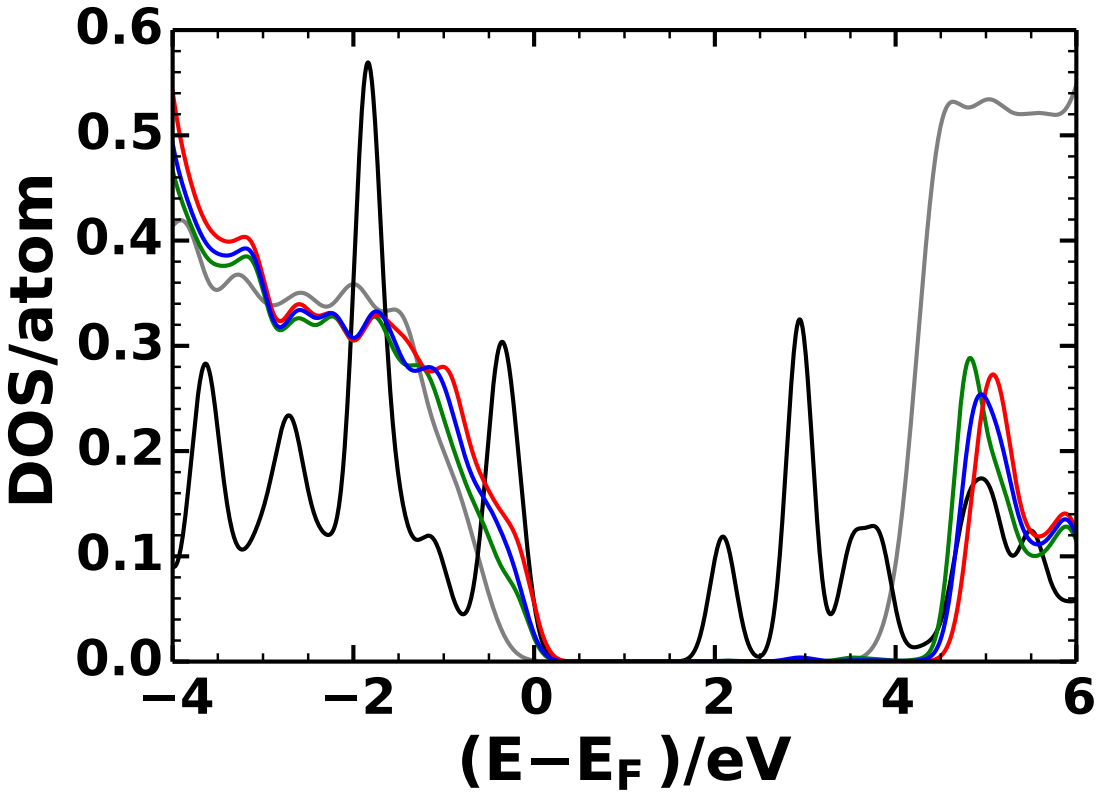

Figure 6.9.: Density of states projected onto the C atoms in a hBN sheet where a TW-Pyr N_{out} molecule is adsorbed. The PDOSes are averaged over all the atoms in the different regions shown in figure 6.4: region A in blue, B in green, C in red. The PDOS averaged over all the atoms belonging to the molecule is plotted in black, the DOS per atom of pure hBN is plotted in gray.

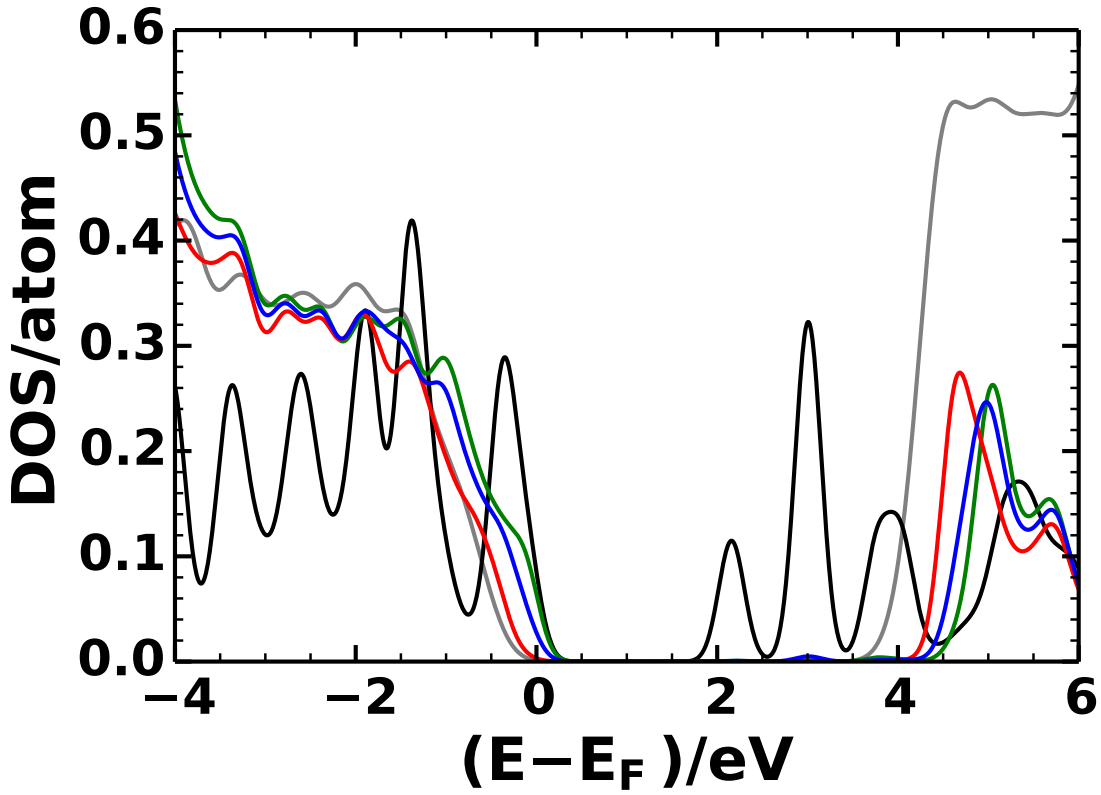

Figure 6.10.: Density of states projected onto the C atoms in a hBN sheet where a TW-Pyr N_{in} molecule is adsorbed. The PDOSes are averaged over all the atoms in the different regions shown in figure 6.4: region A in blue, B in green, C in red. The PDOS averaged over all the atoms belonging to the molecule is plotted in black, the DOS per atom of pure hBN is plotted in gray.

6.6. Charge Rearrangements

As for graphene, the charge rearrangements upon adsorption of a molecule are investigated. The methodological description of the calculation of this quantity is given in chapter 3.9. The resulting curves are found in figure 6.11.

In general, the redistribution of the electron density due to the adsorption is smaller than for the graphene sheet. The overall shape of the curves is very similar in the two cases, which means that again electrons are transferred from the hBN layer to the molecule. While charge transfer is expected for metallic (or semi-metallic) substrates, it is surprising to find it for an isolating substrate like hBN. The region of strongest electron accumulation is around the dipolar C-N bond in the molecule. Inside the plane of the substrate, there is a relocation of charges probably due to the potential stemming from the dipolar endgroups. As for TW-CN on graphene, the region below the molecule has only small charge redistributions.

All in all, the charge rearrangements lead to a bond dipole, which is weaker than for graphene.

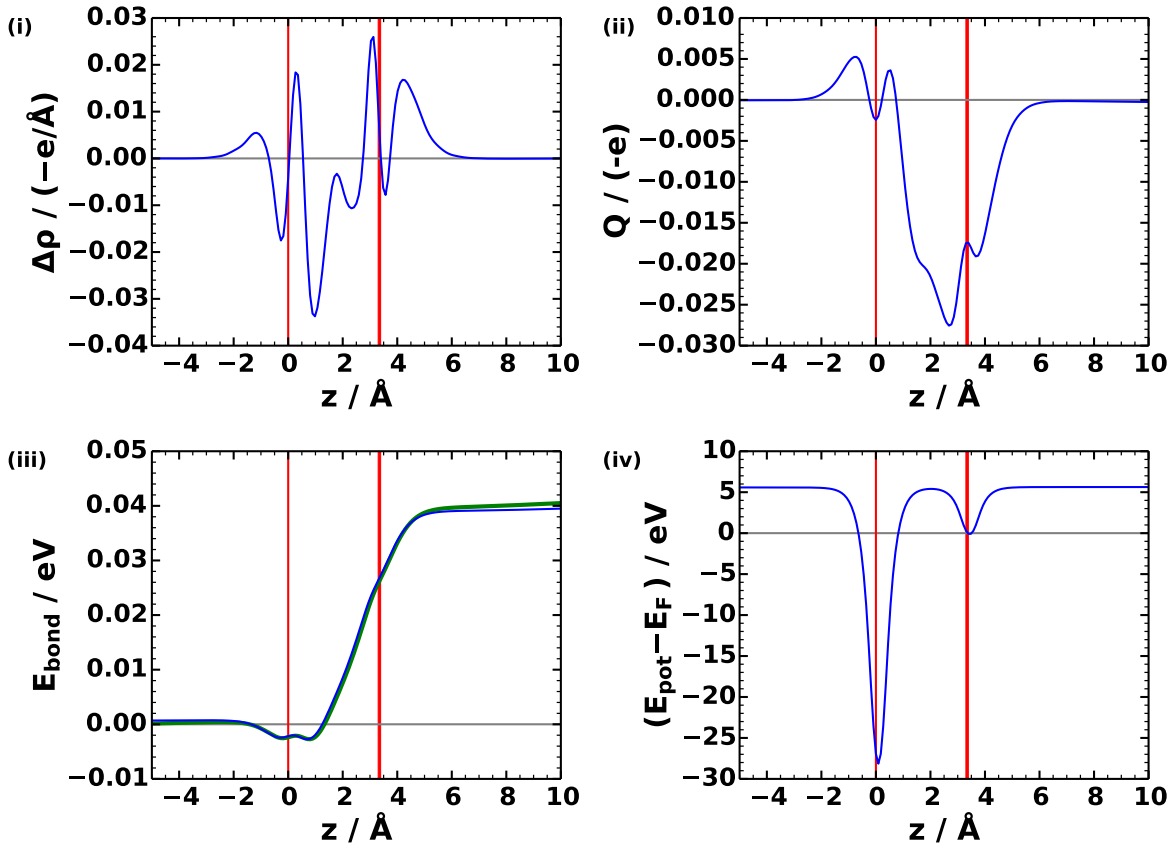

(a) (i) Charge rearrangements $\Delta\rho(z)$. (ii) Total amount of flown charge $Q(z)$. (iii) Resulting bond dipole $E_{\text{bond}}(z)$ calculated by integration of $Q(z)$ (blue line) and directly from the VASP potential energies (green line). (iv) Electrostatic potential of the total system, showing the position of the hBN sheet and the molecule. The two vertical red lines mark the position of the hBN sheet (left) and the molecule (right). Here, 40 Å of vacuum and the dipole correction were used.

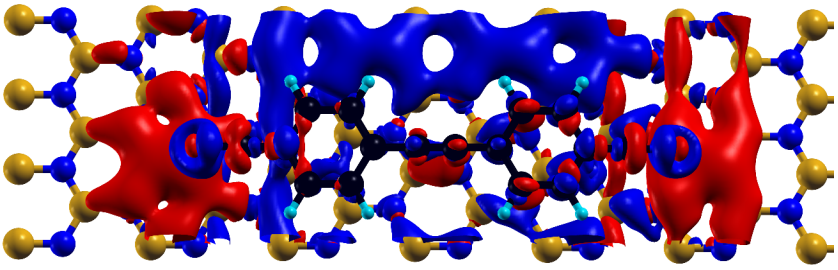

(b) Isosurface of $\Delta\rho$ at $\pm 10^{-3}$ ($-$e/Å^3), top view. Blue means electron accumulation, red means reduction of the electron density.

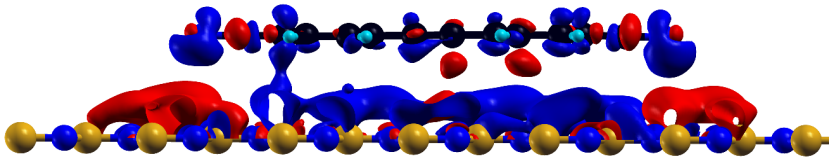

(c) Isosurface of $\Delta\rho$ at $\pm 10^{-3}$ ($-$e/Å^3), side view.

Figure 6.11.: Charge rearrangements due to the adsorption of the TW-CN molecule on hBN. Isosurface plots produced with XCrysDen [94].

7. Conclusions and Outlook

The use of lines of dipoles turns out to be an interesting means of locally changing the electronic structure of graphene. The modification of the electrostatic potential shifts the energy of the carbon states, which in turn can be observed in the density of states of carbon atoms. While a separation and localization of occupied and unoccupied states happens to a certain extent, the formation of separated transport channels for electrons and holes is not confirmed. Nevertheless, transport calculations with these systems would be the logical next step for a further exploration of their properties.

The lateral extent of the observed effects is rather short-ranged, which limits possible test cases to narrow strips of graphene between the dipolar lines. While the experimental feasibility of linearly arranged dipolar substituents in graphene is doubtful to say the least, using self-assembled monolayers could be the route to go for implementing these systems in practise. There, the strength of the effect is, however, much weaker than for directly embedded dipoles. Thus, finding molecules with strongly dipolar end groups and a low adsorption distance would be beneficial for the overall effect. Of course, also the strip width has to be kept low while maintaining a high dipole density along the line.

Apart from graphene, which is by far the most popular two-dimensional material, using single layers of semiconducting or isolating materials is also an interesting option. In hexagonal boron nitride, the example of such an isolator chosen for this work, the resulting energy shift of the density of states is bigger than in graphene in all tested cases. This is attributed to a significant lowering of the attenuation of the potential created by the dipolar elements in hBN compared to graphene. However, the origin of this different behavior has not been thouroughly investigated here, so that the apparent dependence on molecule size was not fully explained. An in-depth investigation of these effects in conjuction with the study of other, similar materials certainly appears to be rewarding when looking at the outcome of the calculations performed in this thesis. Furthermore, these results suggest that in these semiconductors a spatial separation of electron and hole states might be achieved. Therefore a more detailed examination of these systems is certainly worthwile.

Appendix

A. Typical Input Files

A single point VASP calculation needs four input files: `INCAR` contains the necessary parameters for the numerical algorithms and the general behavior of the program, `POSCAR` defines the geometry of the system, `POTCAR` has the PAW potentials for the individual atomic species and `KPOINTS` gives the *k*-point grid.

The `POSCAR`-file is very system specific and the `POTCAR` file is just built from the repository of `POTCAR` files.

For geometry optimizations using GADGET, the additional `INPDAT` input file has to be given.

Preoptimized molecule gas phase geometries were obtained using Gaussian, the corresponding input file is `geoopt.com`.

A.1. INCAR

```
SYSTEM = ...
ENCUT = 279.692
NWRITE = 2
PREC = Normal
ISPIN = 1#no spin=1
ICHARG=1
ISTART=1

EDIFF = 1.E-04 (or 1.E-06)
EDIFFG = -1E-02
NELMIN = 1
NSW = 1
IBRION = -1
ISYM = 0

LORBIT = 11
EMIN = -20.
EMAX = 15.
NEDOS = 5001
```

```
ISMEAR = 0
SIGMA = 0.01
LREAL = Auto
AMIN=0.01
VOSKOWN = 1
ALGO = Normal
LDIAG = .TRUE.
LPLANE = .TRUE.
NSIM = 4
NPAR = 4

LWAVE = .FALSE.
LCHARG = .TRUE.
LELF = .FALSE.
LVHAR = .TRUE.

IDIPOL = 0
LDIPOL = .FALSE.
```

The meaning of the individual tags can be found in the VASP manual [82]. In some `INCAR` files, the following tags were used: for non-self-consistent calculations (for the band structure or partial charge densities) *ICHARG*=11, to calculate energy- or band- and *k*-resolved charge densities *LPARD*, *EINT*, *LSEPB*, *IBAND*, and *LSEPK*, to calculate the energy of the core states of the atoms *ICORELEVEL*, for the dipole correction *IDIPOL* and *LDIPOL*, if the dipole correction did not converge faster than the SCF cycle *NELMIN*, for calculations with more or less electrons than in the electrically neutral unit cell *NELECT*, if the number of calculated bands was not sufficient *NBANDS*.

A.2. KPOINTS

For self-consistent calculations, a `KPOINTS` file according to the following template was used:

```
Automatic Mesh
0
Gamma
  6 21 1
  0 0 0
```

The number of *k*-points per direction was changed according to the unit cell or Brillouin zone size.

For non-self-consistent calculations (*ICHARG*=11) of the band structure, a `KPOINTS` file like the following was used:

```
Automatic Mesh
50
Line-mode
Reciprocal

0.5 0.0 0.0
0.0 0.0 0.0

0.0 0.0 0.0
0.0 0.5 0.0
```

The number of *k*-points (50 in this example) and the paths through *k*-space (here from X to Γ and from Γ to Y in a rectangular unit cell) were adjusted to the needs of the individual calculations.

A.3. INPDAT

```
Input file, check inputer.py for all available tags!!!

HESSIAN=3
HUPDATE=1
CART=0
GCRITER=0.000194469

SCRITER=5.02
ECRITER=1e1
ASCALE=1.3
RELAX=0
OPTENGINE=0
NFREE=5
NSW = 1000

#BSCALE= 1.6
#FRAGCOORD= 2
#POTIM=100
```

Most importantly, the energy convergence criterion was found to be typically not necessary and was thus set to 10 eV for some of the calculations for a speedup in convergence. For some geometry optimizations, additional constraints were set with the `ICONST` file as

explained by Tomáš Bučko in the `README.txt` file of GADGET.

A.4. Gaussian Geometry Optimization

A template input file for a gas phase geometry optimization of a molecule (the initial geometry can be created using programs like molden or MarvinSketch) in Gaussian looks like this `geoopt.com` file:

```
%chk=geoopt.chk
%nproc=2
%mem=2gb
# PBEPBE/6-311G(d,p) pop=regular opt=(maxcycles=200) nosymm

System-Name

0 1
 C     0.000000     0.000000     0.000000
 ...
```

The individual initial atomic positions have to be given in analogy to the carbon atom at the origin in this file. The input file has to end with a blank line. For a detailed description of the input file, refer to the Gaussian manual.

B. Program to Calculate the Dipole Line Potential

The potential of a line of dipoles located at the y-axis with the dipole moments pointing in the x-direction can be calculated according to (2.9). The following file is a FORTRAN 90 program for doing this summation:

```
subroutine chaindippot(x,expo,b,y,z,pot,dpot)
implicit none
double precision, intent(in) :: x, expo, b, y, z
double precision, intent(out) :: pot, dpot
double precision :: potold, r
integer :: N, i

N=5000

pot = 0.0
do i=-N,N
    potold=pot
    r=sqrt(x**2+(y+i*b)**2+z**2)
    r=x/r**3*exp(-expo*r)*(1+expo*r)
    if(isnan(r)) cycle
    pot=pot+r
end do
dpot=pot-potold
end subroutine chaindippot
```

The input parameters of this subroutine are the point of observation `x`, `y`, `z`, the Thomas-Fermi screening constant `expo` and the lattice constant of the line `b`. For a calculation without Thomas-Fermi screening, `expo` has to be set to zero. The output parameters are the potential per dipole moment `pot` and an estimate of the error, `dpot`.

The number of summed terms is $2N$, and for realistic values of `b`, `N=5000` has turned out to be sufficient. If, however, the estimated error `dpot` is too large, this value can be increased. Should the current term `r` fall below the lowest possible floating point number, its value is `nan` and it is not added to the potential.

The resulting value `pot` has to be multiplied by the dipole moment of the individual dipoles forming the line. If all lengths are given in $\mathring{A}$ and the dipole moment is given in eÅ, the electron potential energy in eV is $E_{\text{pot}} = 14.399640 \cdot p \cdot \texttt{pot}$.

While this subroutine can be compiled with a FORTRAN compiler and then used in a FORTRAN program, it is also possible to use f2py[1] to be able to call this subroutine as a function from Python programs. The corresponding command is
`f2py -c --fcompiler=gfortran -m chaindippot chaindippot.f90`.

[1] For a description see `http://docs.scipy.org/doc/numpy-dev/f2py/`.

C. Shifted PDOS Model

The following listing shows the main part[1] of the python script[2] used for the calculation of the shifted PDOS model that was introduced in chapter 4.3.5.

```
import numpy as np
from scipy.integrate import quad
from scipy.integrate import cumtrapz
from scipy.optimize import fsolve

# The following function decorators can make functions
# handle vectors as well
def make_vector_handleable(func):
    def func_univ(ks,*args,**kwargs):
        if hasattr(ks, '__iter__'):
            res=[]
            for k in ks:
                res.append(func(k,*args,**kwargs))
            return np.array(res)
        else:
            return func(ks,*args,**kwargs)
    return func_univ

# We define a function that represents the PDOS of
# each of the atoms.
@make_vector_handleable
def pdos_atom(E):
    return 0.5*np.abs(E)

# We define a shift function that shifts the
# PDOS for an atom.
# For that we need the number of atoms N.
# The atoms are at positions 0,...,N-1.
# The maximum shift of the PDOS is max_shift.
N=20
```

[1] In particular, the plotting commands have been left out.

[2] Tested with Python 2.7.3 (default, Feb 27 2014, 19:58:35) and Python 3.2.3 (default, Feb 27 2014, 21:31:18) with numpy 1.6.1 and scipy 0.9.0.

```
max_shift=2

@make_vector_handleable
def shift_pdos(k):
    if k<N/4:
        return max_shift*(-1+4*k/float(N))
    elif k<3*N/4:
        return 0
    else:
        return max_shift*(1-4*(N-k-1)/float(N))

# coordinates of the atoms: 0, ..., N-1
atoms=range(N)

# Construct the total DOS from the PDOSes:
@make_vector_handleable
def total_dos(E):
    dos=0
    for at in atoms:
        dos+=pdos_atom(E-shift_pdos(at))
    return dos

#energies=np.linspace(-5-max_shift,5+max_shift,101)
#dos=total_dos(energies)

# We will now fill the system with extra electrons,
# i.e. use a higher number of electrons and shift the
# Fermi energy (from zero) to higher energies.

# We look at the integated DOS:
@make_vector_handleable
def total_dos_int(dE):
    return quad(total_dos,0.0,dE)[0]

# Now we can find out how the Fermi energy E_F changes
# when we put in a certain number of extra electrons
# into the system:

dne = 1 # number of additional electrons
dEF = fsolve(lambda E: total_dos_int(E)-dne,0.5)

# We now choose a certain number of extra electrons
# N_extra, calculate the Fermi energy shift for this
# number and then fill the PDOSes up to that energy.
```

```
@make_vector_handleable
def extra_electrondensity(N_extra,atoms):
    startval=0.5*np.sign(N_extra)
    dE_F = fsolve(lambda E: total_dos_int(E)-N_extra,
                  startval)
    nelec_perat=[]
    for at in atoms:
        nelec=quad(lambda E: pdos_atom(E-shift_pdos(at)),
                                       0.0,dE_F)[0]
        nelec_perat.append(nelec)
    return np.array(nelec_perat)

print(extra_electrondensity([-1,0,1],atoms))
```

For the semiconductor model, the only difference is

```
@make_vector_handleable
def pdos_atom(E):
    if E<-2.5 or E>2.5:
        return 1
    else:
        return 0
```

Bibliography

1. A. K. Geim and K. S. Novoselov. “The rise of graphene”. *Nature Materials* **6,** 183 (2007).
2. K. Oura, V. Lifshits, A. Saranin, and A. Zotov. *Surface Science: An Introduction* (Springer Berlin Heidelberg, 2003).
3. A. Natan, L. Kronik, H. Haick, and R. T. Tung. “Electrostatic Properties of Ideal and Non-ideal Polar Organic Monolayers: Implications for Electronic Devices”. *Advanced Materials* **19,** 4103 (2007).
4. M. L. Blumenfeld, M. P. Steele, and O. L. Monti. “Near- and Far-Field Effects on Molecular Energy Level Alignment at an Organic/Electrode Interface”. *The Journal of Physical Chemistry Letters* **1,** 145 (2010).
5. G. Heimel, F. Rissner, and E. Zojer. “Modeling the Electronic Properties of π-Conjugated Self-Assembled Monolayers”. *Advanced Materials* **22,** 2494 (2010).
6. V. H. Nguyen, F. Mazzamuto, A. Bournel, and P. Dollfus. “Resonant tunnelling diodes based on graphene/h-BN heterostructure”. *Journal of Physics D: Applied Physics* **45,** 325104 (2012).
7. R. Martin. *Electronic Structure: Basic Theory and Practical Methods* (Cambridge University Press, 2004).
8. D. Sholl and J. Steckel. *Density Functional Theory: A Practical Introduction* (Wiley, 2011).
9. P. Hohenberg and W. Kohn. “Inhomogeneous Electron Gas”. *Physical Review* **136,** B864 (1964).
10. W. Kohn and L. J. Sham. “Self-Consistent Equations Including Exchange and Correlation Effects”. *Physical Review* **140,** A1133 (1965).
11. J. P. Perdew, K. Burke, and M. Ernzerhof. “Generalized Gradient Approximation Made Simple”. *Physical Review Letters* **77,** 3865 (1996).
12. R. Parr and R. Yang. *Density-Functional Theory of Atoms and Molecules* (Oxford University Press, USA, 1989).
13. E. Gross, R. Dreizler, and N. A. T. O. S. A. Division. *Density Functional Theory* (Springer, 1995).
14. W. Kohn. “Nobel Lecture: Electronic structure of matter-wave functions and density functionals”. *Reviews of Modern Physics* **71,** 1253 (1999).

15. C. Fiolhais, F. Nogueira, and M. Marques. *A Primer in Density Functional Theory* (Springer, 2003).
16. W. Nolting. *Grundkurs Theoretische Physik 3: Elektrodynamik* (Springer, 2011).
17. J. Lekner. "Coulomb Forces and Potentials in Systems with an Orthorhombic Unit Cell". *Molecular Simulation* **20,** 357 (1998).
18. D. M. Taylor and G. F. Bayes. "Calculating the surface potential of unionized monolayers". *Physical Review E* **49,** 1439 (1994).
19. A. Natan, Y. Zidon, Y. Shapira, and L. Kronik. "Cooperative effects and dipole formation at semiconductor and self-assembled-monolayer interfaces". *Physical Review B* **73,** 193310 (2006).
20. N. Ashcroft and N. Mermin. *Solid State Physics* (Holt, Rinehart and Winston, 1976).
21. R. Gross and A. Marx. *Festkörperphysik* (De Gruyter, 2012).
22. J. M. Ugalde and C. Sarasola. "Bound electronic states in a statically screened electric-dipole potential". *Physical Review A* **54,** 2868 (1996).
23. J. Warner. *Graphene: fundamentals and emergent applications* (Elsevier, Oxford, 2013).
24. P. Wallace. "The Band Theory of Graphite". *Physical Review* **71,** 622 (1947).
25. K. S. Novoselov, A. K. Geim, S. V. Morozov, D. Jiang, Y. Zhang, S. V. Dubonos, I. V. Grigorieva, and A. A. Firsov. "Electric Field Effect in Atomically Thin Carbon Films". *Science* **306,** 666 (2004).
26. A. H. Castro Neto, N. M. R. Peres, K. S. Novoselov, and A. K. Geim. "The electronic properties of graphene". *Reviews of Modern Physics* **81,** 109 (2009).
27. C. Lee, X. Wei, J. W. Kysar, and J. Hone. "Measurement of the Elastic Properties and Intrinsic Strength of Monolayer Graphene". *Science* **321,** 385 (2008).
28. R. E. Peierls. "Quelques propriétés typiques des corps solides". *Annales de l'Institut Henri Poincaré* **5,** 177 (1935).
29. L. D. Landau. "Zur Theorie der Phasenumwandlungen II". *Physikalische Zeitschrift der Sowjetunion* **11,** 26 (1937).
30. A. Fasolino, J. H. Los, and M. I. Katsnelson. "Intrinsic ripples in graphene". *Nature Materials* **6,** 858 (2007).
31. J. C. Meyer, A. K. Geim, M. I. Katsnelson, K. S. Novoselov, T. J. Booth, and S. Roth. "The structure of suspended graphene sheets". *Nature* **446,** 60 (2007).
32. L. Landau and E. Lifshitz. *Statistical Physics* **v. 5.** (Elsevier Science, 1996).
33. Y. Ando. "Topological Insulator Materials". *Journal of the Physical Society of Japan* **82,** 102001 (2013).
34. T. Plehn. *Lectures on LHC Physics* (Springer, 2012).

35. M. I. Katsnelson, K. S. Novoselov, and A. K. Geim. “Chiral tunnelling and the Klein paradox in graphene”. *Nature Physics* **2,** 620 (2006).

36. J. C. Martinez, M. B. A. Jalil, and S. G. Tan. “Klein tunneling and zitterbewegung and the formation of a polarized p-n junction in graphene”. *Applied Physics Letters* **97,** 062111 (2010).

37. V. Ariel and A. Natan. “Electron Effective Mass in Graphene”. *arXiv preprint arXiv:1206.6100.* (2012).

38. V. Barone, O. Hod, and G. E. Scuseria. “Electronic Structure and Stability of Semiconducting Graphene Nanoribbons”. *Nano Letters* **6,** 2748 (2006).

39. Y.-W. Son, M. L. Cohen, and S. G. Louie. “Energy Gaps in Graphene Nanoribbons”. *Physical Review Letters* **97,** 216803 (2006).

40. L. Yang, C.-H. Park, Y.-W. Son, M. Cohen, and S. Louie. “Quasiparticle Energies and Band Gaps in Graphene Nanoribbons”. *Physical Review Letters* **99,** 186801 (2007).

41. Z. Chen, Y.-M. Lin, M. J. Rooks, and P. Avouris. “Graphene nano-ribbon electronics”. *Physica E: Low-dimensional Systems and Nanostructures* **40,** 228 (2007).

42. M. Han, B. Özyilmaz, Y. Zhang, and P. Kim. “Energy Band-Gap Engineering of Graphene Nanoribbons”. *Physical Review Letters* **98,** 206805 (2007).

43. D. Malterre, B. Kierren, Y. Fagot-Revurat, C. Didiot, F. J. García de Abajo, F. Schiller, J. Cordón, and J. E. Ortega. “Symmetry breaking and gap opening in two-dimensional hexagonal lattices”. *New Journal of Physics* **13,** 013026 (2011).

44. *International Tables for Crystallography: Space-group symmetry* 1st ed. (eds T. Hahn, H. Fuess, T. Hahn, H. Wondratschek, U. Müller, U. Shmueli, E. Prince, A. Authier, V. Kopský, D. B. Litvin, M. G. Rossmann, E. Arnold, S. Hall, and B. McMahon) (International Union of Crystallography, Chester, England, 2006).

45. D. Vanderbilt. *PythTB* URL: `http://www.physics.rutgers.edu/pythtb/index.html`.

46. K. S. Novoselov, V. I. Fal’ko, L. Colombo, P. R. Gellert, M. G. Schwab, and K. Kim. “A roadmap for graphene”. *Nature* **490,** 192 (2012).

47. M. Fujita, K. Wakabayashi, K. Nakada, and K. Kusakabe. “Peculiar Localized State at Zigzag Graphite Edge”. *Journal of the Physics Society Japan* **65,** 1920 (1996).

48. K. Nakada, M. Fujita, G. Dresselhaus, and M. S. Dresselhaus. “Edge state in graphene ribbons: Nanometer size effect and edge shape dependence”. *Physical Review B* **54,** 17954 (1996).

49. R. Ribeiro, N. Peres, J. Coutinho, and P. Briddon. “Inducing energy gaps in monolayer and bilayer graphene: Local density approximation calculations”. *Physical Review B* **78,** 075442 (2008).

50. O. Hod, V. Barone, J. E. Peralta, and G. E. Scuseria. “Enhanced half-metallicity in edge-oxidized zigzag graphene nanoribbons”. *Nano Letters* **7,** 2295 (2007).

51. F. Cervantes-Sodi, G. Csanyi, S. Piscanec, and A. C. Ferrari. “Edge-functionalized and substitutionally doped graphene nanoribbons: Electronic and spin properties”. *Physical Review B* **77,** 165427 (2008).
52. P. Wagner, C. P. Ewels, J.-J. Adjizian, L. Magaud, P. Pochet, S. Roche, A. Lopez-Bezanilla, V. V. Ivanovskaya, A. Yaya, M. Rayson, P. Briddon, and B. Humbert. “Band Gap Engineering via Edge-Functionalization of Graphene Nanoribbons”. *The Journal of Physical Chemistry C* **117,** 26790 (2013).
53. S. Dutta, A. Manna, and S. Pati. “Intrinsic Half-Metallicity in Modified Graphene Nanoribbons”. *Physical Review Letters* **102,** 096601 (2009).
54. Z. H. Ni, T. Yu, Y. H. Lu, Y. Y. Wang, Y. P. Feng, and Z. X. Shen. “Uniaxial Strain on Graphene: Raman Spectroscopy Study and Band-Gap Opening”. *ACS Nano* **2,** 2301 (2008).
55. V. Pereira, A. Castro Neto, and N. Peres. “Tight-binding approach to uniaxial strain in graphene”. *Physical Review B* **80,** 045401 (2009).
56. P. A. Denis. “Band gap opening of monolayer and bilayer graphene doped with aluminium, silicon, phosphorus, and sulfur”. *Chemical Physics Letters* **492,** 251 (2010).
57. I. Zanella, S. Guerini, S. Fagan, J. Mendes Filho, and A. Souza Filho. “Chemical doping-induced gap opening and spin polarization in graphene”. *Physical Review B* **77,** 073404 (2008).
58. H. Pinto, R. Jones, J. P. Goss, and P. R. Briddon. “p-type doping of graphene with F4-TCNQ”. *Journal of Physics: Condensed Matter* **21,** 402001 (2009).
59. I. Gierz, C. Riedl, U. Starke, C. R. Ast, and K. Kern. “Atomic Hole Doping of Graphene”. *Nano Letters* **8,** 4603 (2008).
60. H. Sevinçli, M. Topsakal, E. Durgun, and S. Ciraci. “Electronic and magnetic properties of 3d transition-metal atom adsorbed graphene and graphene nanoribbons”. *Physical Review B* **77,** 195434 (2008).
61. E. Bekyarova, M. E. Itkis, P. Ramesh, C. Berger, M. Sprinkle, W. A. de Heer, and R. C. Haddon. “Chemical Modification of Epitaxial Graphene: Spontaneous Grafting of Aryl Groups”. *Journal of the American Chemical Society* **131,** 1336 (2009).
62. X. Peng and R. Ahuja. “Symmetry Breaking Induced Bandgap in Epitaxial Graphene Layers on SiC”. *Nano Letters* **8,** 4464 (2008).
63. J. Song, A. Shytov, and L. Levitov. “Electron Interactions and Gap Opening in Graphene Superlattices”. *Physical Review Letters* **111,** 266801 (2013).
64. L. Ci, L. Song, C. Jin, D. Jariwala, D. Wu, Y. Li, A. Srivastava, Z. F. Wang, K. Storr, L. Balicas, F. Liu, and P. M. Ajayan. “Atomic layers of hybridized boron nitride and graphene domains”. *Nature Materials* **9,** 430 (2010).
65. Z. Huang, V. Crespi, and J. Chelikowsky. “Electronic properties of mixed-phase graphene/h-BN sheets using real-space pseudopotentials”. *Physical Review B* **88,** 235425 (2013).

66. A. K. Geim and I. V. Grigorieva. “Van der Waals heterostructures”. *Nature* **499,** 419 (2013).

67. C. Bjelkevig, Z. Mi, J. Xiao, P. A. Dowben, L. Wang, W.-N. Mei, and J. A. Kelber. “Electronic structure of a graphene/hexagonal-BN heterostructure grown on Ru(0001) by chemical vapor deposition and atomic layer deposition: extrinsically doped graphene”. *Journal of Physics: Condensed Matter* **22,** 302002 (2010).

68. A. Avetisyan, B. Partoens, and F. Peeters. “Electric field tuning of the band gap in graphene multilayers”. *Physical Review B* **79,** 035421 (2009).

69. K. Mak, C. Lui, J. Shan, and T. Heinz. “Observation of an Electric-Field-Induced Band Gap in Bilayer Graphene by Infrared Spectroscopy”. *Physical Review Letters* **102,** 256405 (2009).

70. C. H. Ahn, M. Di Ventra, J. N. Eckstein, C. D. Frisbie, M. E. Gershenson, A. M. Goldman, I. H. Inoue, J. Mannhart, A. J. Millis, A. F. Morpurgo, D. Natelson, and J.-M. Triscone. “Electrostatic modification of novel materials”. *Reviews of Modern Physics* **78,** 1185 (2006).

71. E. Jones, T. Oliphant, P. Peterson, *et al. SciPy: Open source scientific tools for Python* http://www.scipy.org/ [Online; accessed 2014-10-21] (2001).

72. S. van der Walt, S. C. Colbert, and G. Varoquaux. “The NumPy Array: A Structure for Efficient Numerical Computation”. *Computing in Science & Engineering* **13,** 22 (2011).

73. J. D. Hunter. “Matplotlib: A 2D graphics environment”. *Computing In Science & Engineering* **9,** 90 (2007).

74. G. Kresse and J. Hafner. “Ab initio molecular dynamics for liquid metals”. *Physical Review B* **47,** 558 (1993).

75. G. Kresse and J. Hafner. “Ab initio molecular-dynamics simulation of the liquid-metal–amorphous-semiconductor transition in germanium”. *Physical Review B* **49,** 14251 (1994).

76. G. Kresse and J. Furthmüller. “Efficiency of ab-initio total energy calculations for metals and semiconductors using a plane-wave basis set”. *Computational Materials Science* **6,** 15 (1996).

77. G. Kresse. “Efficient iterative schemes for ab initio total-energy calculations using a plane-wave basis set”. *Physical Review B* **54,** 11169 (1996).

78. J. P. Perdew, K. Burke, and M. Ernzerhof. “Generalized Gradient Approximation Made Simple [Phys. Rev. Lett. 77, 3865 (1996)]”. *Physical Review Letters* **78,** 1396 (1997).

79. P. E. Blöchl. “Projector augmented-wave method”. *Physical Review B* **50,** 17953 (1994).

80. G. Kresse and D. Joubert. “From ultrasoft pseudopotentials to the projector augmented-wave method”. *Physical Review B* **59,** 1758 (1999).

81. H. J. Monkhorst and J. D. Pack. “Special points for Brillouin-zone integrations”. *Physical Review B* **13,** 5188 (1976).

82. G. Kresse, J. Furthmuller, and M. Marsman. *VASP the GUIDE* 2012.

83. T. Bučko, J. Hafner, and J. G. Ángyán. “Geometry optimization of periodic systems using internal coordinates”. *The Journal of Chemical Physics* **122,** 124508 (2005).

84. A. Tkatchenko and M. Scheffler. “Accurate Molecular Van Der Waals Interactions from Ground-State Electron Density and Free-Atom Reference Data”. *Physical Review Letters* **102,** 073005 (2009).

85. T. Bučko, S. Lebègue, J. Hafner, and J. Ángyán. “Tkatchenko-Scheffler van der Waals correction method with and without self-consistent screening applied to solids”. *Physical Review B* **87,** 064110 (2013).

86. M. J. Frisch, G. W. Trucks, H. B. Schlegel, G. E. Scuseria, M. A. Robb, J. R. Cheeseman, G. Scalmani, V. Barone, B. Mennucci, G. A. Petersson, H. Nakatsuji, M. Caricato, X. Li, H. P. Hratchian, A. F. Izmaylov, J. Bloino, G. Zheng, J. L. Sonnenberg, M. Hada, M. Ehara, K. Toyota, R. Fukuda, J. Hasegawa, M. Ishida, T. Nakajima, Y. Honda, O. Kitao, H. Nakai, T. Vreven, J. A. Montgomery Jr., J. E. Peralta, F. Ogliaro, M. Bearpark, J. J. Heyd, E. Brothers, K. N. Kudin, V. N. Staroverov, T. Keith, R. Kobayashi, J. Normand, K. Raghavachari, A. Rendell, J. C. Burant, S. S. Iyengar, J. Tomasi, M. Cossi, N. Rega, J. M. Millam, M. Klene, J. E. Knox, J. B. Cross, V. Bakken, C. Adamo, J. Jaramillo, R. Gomperts, R. E. Stratmann, O. Yazyev, A. J. Austin, R. Cammi, C. Pomelli, J. W. Ochterski, R. L. Martin, K. Morokuma, V. G. Zakrzewski, G. A. Voth, P. Salvador, J. J. Dannenberg, S. Dapprich, A. D. Daniels, Ö. Farkas, J. B. Foresman, J. V. Ortiz, J. Cioslowski, and D. J. Fox. *Gaussian 09 Revision C.01* Gaussian Inc. Wallingford CT 2010.

87. L. Köhler and G. Kresse. “Density functional study of CO on Rh(111)”. *Physical Review B* **70,** 165405 (2004).

88. A. Görling. “Density-functional theory for excited states”. *Physical Review A* **54,** 3912 (1996).

89. L. Romaner, D. Nabok, P. Puschnig, E. Zojer, and C. Ambrosch-Draxl. “Theoretical study of PTCDA adsorbed on the coinage metal surfaces, Ag(111), Au(111) and Cu(111)”. *New Journal of Physics* **11,** 053010 (2009).

90. P. Lambin, H. Amara, F. Ducastelle, and L. Henrard. “Long-range interactions between substitutional nitrogen dopants in graphene: Electronic properties calculations”. *Physical Review B* **86,** 045448 (2012).

91. J. A. Lawlor, P. D. Gorman, S. R. Power, C. G. Bezerra, and M. S. Ferreira. “Sublattice imbalance of substitutionally doped nitrogen in graphene”. *arXiv preprint arXiv:1405.5030.* (2014).

92. P. A. Khomyakov, G. Giovannetti, P. C. Rusu, G. Brocks, J. van den Brink, and P. J. Kelly. “First-principles study of the interaction and charge transfer between graphene and metals”. *Physical Review B* **79,** 195425 (2009).

93. T. Ohta. “Controlling the Electronic Structure of Bilayer Graphene”. *Science* **313,** 951 (2006).

94. A. Kokalj. “Computer graphics and graphical user interfaces as tools in simulations of matter at the atomic scale”. *Computational Materials Science* **28,** 155 (2003). Code available from http://www.xcrysden.org/.

95. L. Grill, M. Dyer, L. Lafferentz, M. Persson, M. V. Peters, and S. Hecht. “Nano-architectures by covalent assembly of molecular building blocks”. *Nature Nanotechnology* **2,** 687 (2007).

96. J. M. Tour, M. Kozaki, and J. M. Seminario. “Molecular scale electronics: a synthetic/computational approach to digital computing”. *Journal of the American Chemical Society* **120,** 8486 (1998).

97. D. A. Egger, F. Rissner, E. Zojer, and G. Heimel. “Polarity Switching of Charge Transport and Thermoelectricity in Self-Assembled Monolayer Devices”. *Advanced Materials* **24,** 4403 (2012).

98. E. J. G. Santos and E. Kaxiras. “Electric-Field Dependence of the Effective Dielectric Constant in Graphene”. *Nano Letters* **13,** 898 (2013).

99. G. Heimel, L. Romaner, E. Zojer, and J.-L. Brédas. “Toward Control of the Metal-Organic Interfacial Electronic Structure in Molecular Electronics: A First-Principles Study on Self-Assembled Monolayers of π-Conjugated Molecules on Noble Metals”. *Nano Letters* **7,** 932 (2007).

100. K. K. Kim, A. Hsu, X. Jia, S. M. Kim, Y. Shi, M. Dresselhaus, T. Palacios, and J. Kong. “Synthesis and Characterization of Hexagonal Boron Nitride Film as a Dielectric Layer for Graphene Devices”. *ACS Nano* **6,** 8583 (2012).

101. B. G. Demczyk, J. Cumings, A. Zettl, and R. O. Ritchie. “Structure of boron nitride nanotubules”. *Applied Physics Letters* **78,** 2772 (2001).

102. N. Alem, R. Erni, C. Kisielowski, M. Rossell, W. Gannett, and A. Zettl. “Atomically thin hexagonal boron nitride probed by ultrahigh-resolution transmission electron microscopy”. *Physical Review B* **80,** 155425 (2009).

103. J. P. Perdew and M. Levy. “Physical content of the exact Kohn-Sham orbital energies: band gaps and derivative discontinuities”. *Physical Review Letters* **51,** 1884 (1983).

104. Y. Gao, W. Ren, T. Ma, Z. Liu, Y. Zhang, W.-B. Liu, L.-P. Ma, X. Ma, and H.-M. Cheng. “Repeated and Controlled Growth of Monolayer, Bilayer and Few-Layer Hexagonal Boron Nitride on Pt Foils”. *ACS Nano* **7,** 5199 (2013).

105. X. Blase, A. Rubio, S. G. Louie, and M. L. Cohen. “Quasiparticle band structure of bulk hexagonal boron nitride and related systems”. *Physical Review B* **51,** 6868 (1995).